Site U1319[1]

Expedition 308 Scientists[2]

Chapter contents

[1]Expedition 308 Scientists, 2006. Site U1319. *In* Flemings, P.B., Behrmann, J.H., John, C.M., and the Expedition 308 Scientists, *Proc. IODP,* 308: College Station TX (Integrated Ocean Drilling Program Management International, Inc.). doi:10.2204/iodp.proc.308.103.2006
[2]**Expedition 308 Scientists' addresses.**

Background and objectives

Geological setting of Brazos-Trinity Basin IV

Brazos-Trinity Basin IV is the southernmost of a chain of five north-south-oriented basins on the continental slope of the Gulf of Mexico (Figs. **F1, F2**) (Satterfield and Behrens, 1990; Winker, 1996). It is located ~250 km south-southeast of Houston, Texas (USA). It forms part of the Brazos-Trinity Fan, a large latest Pleistocene sediment gravity flow depositional system. These basins are a classic area for study of modern deepwater turbidite systems (Morton and Suter, 1996; Winker, 1996; Beaubouef and Friedmann, 2000; Fraticelli, 2003; Anderson and Fillon, 2004). Early work in these basins established the "fill and spill" model whereby deposition in downslope basins would not occur before all upslope basins were filled (Satterfield and Behrens, 1990; Winker, 1996). Subsequent work elaborated on this conceptual model (e.g., Beaubouef and Pirmez, 1999; Friedmann and Beaubouef, 1999). Badalini et al. (2000) and Fraticelli (2003) proposed a contrasting model wherein deposition was contemporaneous in each of these basins.

More recently, Beaubouef et al. (2003) used high-resolution three-dimensional (3-D) seismic data over Brazos-Trinity Basin IV and further refined the work of Beaubouef and Friedmann (2000). Most recently, Mallarino et al. (in press) used piston coring at the margins of Brazos-Trinity Basin IV to characterize its paleogeographic evolution. They described six sedimentary units (Fig. **F3**) and used biostatratigraphic analysis to constrain the age of these sediments; Brazos-Trinity Basin IV formed during the stepwise sea level fall between 115 and 15 ka, ending just prior to the meltwater pulse to the Gulf of Mexico at 14 ka.

Seismic surfaces

Prior to drilling, we mapped six reflectors in Brazos-Trinity Basin IV from closely spaced, high-resolution, two-dimensional (2-D) seismic reflection data: the seafloor reflector (SF) and Reflectors R10, R20, R30, R40, R50, and R60 (Figs. **F4, F5, F6, F7, F8;** Table **T1**). Time-depth conversions were estimated prior to drilling with the following velocity model.

doi:10.2204/iodp.proc.308.103.2006

$$z_{bsf} = 0.7798735\ t_{bsf} + 1.66055 \times 10^{-4}\ t^2_{bsf}, \quad (1)$$

where

z_{bsf} = depth below sea level in meters and
t_{bsf} = two-way traveltime in milliseconds from the seafloor to the horizon of interest.

Equation 1 results from a compilation of regional check shot (velocity) data (C. Winker, Shell International Exploration and Production Company, pers. comm., 2005).

The seismic reflection character of the basin sediments (between Reflector R40 and the seafloor) can be divided into an alternating succession of transparent units and more reflective layered units. We mapped three reflectors (Figs. **F5, F6, F7**):

- R30 caps the first layered package.
- R20 lies within the second layered package.
- R10 caps a thin layered interval in the final reflective package.

Reflector SF caps a high-amplitude but somewhat chaotic package that becomes more layered in the downdip (southern) direction. The reflective layered seismic facies are interpreted as fan deposits, whereas the chaotic and/or transparent deposits are interpreted as debris flows and/or mass transport complexes (Badalini et al, 2000; Winker and Booth, 2000; Beaubouef et al., 2003). Figure **F3** illustrates how our mapped surfaces tie to the sediment packages defined in previous work.

Location of Site U1319

Site U1319 is located in ~1430 m of water on the southern flank of Brazos-Trinity Basin IV (Figs. **F4, F5**). Two-dimensional seismic data illustrate that Site U1319 holes penetrate the flank of the basin. At this location, basin sediments (seafloor to Reflector R40) are projected to be only 35 m thick (Table **T1**). Beneath the basin sediments (beneath Reflector R40), parallel reflectors from hemipelagic sediments are present.

Site U1319 drilling objectives

The primary drilling objectives at this site were the following:

- Establish a reference section to determine the change in rock and fluid properties at this normally pressured location.
- Determine the age of the stratigraphic section and thus contribute to the derivation of an integrated age model for Brazos-Trinity Basin IV.
- Determine the lithology and stratigraphic evolution of the margin of this basin to allow lateral correlation with the sections at Sites U1320 and U1321.
- Sample the subsurface biosphere in this reference location.
- Conduct a logging-while-drilling (LWD)/measurement-while-drilling (MWD) program in a dedicated LWD/MWD hole.

To achieve these objectives, Hole U1319A was continuously cored to terminal depth (TD) at 157.5 meters below seafloor (mbsf). Advanced piston coring (APC) was used to 114.6 mbsf, followed by extended core barrel (XCB) coring. One advanced piston corer temperature (APCT) tool measurement was taken at the bottom of Core 308-U1319A-5H at ~42.5 mbsf. Special tool deployments in Hole U1319A included one deployment of the temperature/dual pressure (T2P) probe just above the seafloor and one deployment at 80.5 mbsf. A dedicated second hole (Hole U1319B) was drilled to conduct the LWD/MWD operations to a TD of 180 mbsf. This was done to generate a complete set of logging parameters for correlation with core and wireline logging data from Hole U1319A.

Operations

Site U1319

The summary of operations at Site U1319 can be found in Tables **T2** and **T3.** The vessel arrived at Site U1319 in the early afternoon of 6 June 2005 and deployed a beacon at 1350 h. The APC/XCB bottom-hole assembly (BHA) was made of a 9⅞ inch polycrystalline diamond (PDC) bit, bit sub, seal bore drill collar, landing sub, top sub, head sub, nonmagnetic drill collar, four controlled-length drill collars, a tapered drill collar, two stands of 5½ inch drill pipe, and a crossover sub (total length = 127.1 m). The usual routine of measuring and rabbiting the tubulars was carried out, and the bit was suspended at a depth of 1393 meters below rig floor (mbrf) by 1945 h. Preparations were then made for a test deployment of the T2P via the coring line colleted delivery system (CDS). Pressure and temperature were measured continuously as the tool was deployed from the surface to the bit, which was suspended ~40 m above the mudline. The core winch operator made planned 2 min stops at 500 and 1000 mbrf for pressure calibration. The probe remained in the bit for 5 min.

After the T2P was recovered, the bit was lowered and tagged the seafloor at 1439.0 mbrf, as observed using the underwater vibration-isolated television (VIT) camera that was deployed to ensure that there were no obstructions, pipeline, or cables on the seafloor prior to spudding. The drill picked up 5 m from seafloor tagging depth in preparation for spudding the

hole. At this point, electrical control problems associated with the mud pumps delayed operations for 45 min while the problem was resolved.

Hole U1319A

Hole U1319A was spudded at 0130 h on 7 June 2005. Recovery in the first core established the seafloor depth at 1440.0 mbrf or 6.4 m shallower than the corrected precision depth recorder (PDR) depth. Piston coring advanced to 80.5 mbsf, when coring was halted for a second deployment of the T2P probe. The T2P was deployed in the hole for the first time at a depth of 80.5 mbsf for 30 min. Because the formation was stiffer than anticipated, the tip of the probe bent and the data quality was questionable.

After the probe was recovered, piston coring resumed to a depth of 114.6 mbsf (Core 13H). After the last four cores partially stroked and were advanced by recovery, coring continued with the XCB. The APC cored 114.6 m with a biogenic gas–augmented average recovery of 104.3%. The cores were oriented starting with Core 4H, and one APCT measurement was attempted at 42.5 mbsf (Core 5H). Fluorescent microspheres were deployed in the core catchers of Cores 1H–10H and 12H. All piston coring was conducted with nonmagnetic APC hardware.

The hole was then deepened to 157.5 mbsf with the XCB, where coring terminated short of the original depth objective of 230 mbsf because all scientific objectives for the site were fulfilled. The XCB system cored 42.9 m with an average recovery of 83.5%. The total cored interval was 157.5 m with a recovery of 155.29 m (average recovery = 98.6%). The bit was pulled clear of the hole at 2120 h on 7 June and raised to 240 m above the seafloor.

Hole U1319B

Hole U1319B was positioned 20 m north of Hole U1319A. A beacon was dropped on site at 0005 h on 12 June 2005, and the hole was spudded at 0915 h on 12 June as the driller observed the bit contacting the seafloor at a depth of 1447.0 mbrf. MWD drilling advanced without incident to the depth objective of 180.0 mbsf at an average rate of penetration of 30.0 m/h by 2100 h on 13 June. After the bit cleared the seafloor at 2200 h, preparations were made to begin the short offset to an approved alternate site.

Lithostratigraphy

The 156 m thick sedimentary section at Site U1319 was divided into six lithostratigraphic units (Table **T4;** Fig. **F9**) based on visual observation, analysis of smear slides, and spectrophotometric data. The high recovery at this site provided a good record of the sedimentary history of this basin margin location. The section is amenable to fine division in the upper part of the hole but is relatively uniform below 31 mbsf. Subdivisions of this condensed basin margin sequence were made to facilitate the expected correlations to the thicker basin fill section at Site U1320.

When splitting sedimentary units between cores we chose the depth of the unit boundary as depth of the top of the next core, as this is closest to the true drilling depth below seafloor (see **"Introduction to Expedition 308 shipboard methods"** in the "Methods" chapter). This resulted in some inconsistencies, typically <0.5 m, between core depth recorded in the visual core descriptions (VCDs) and unit boundary depths.

Description of lithostratigraphic units

Unit I

Interval: Sections 308-U1319C-1H-1, 0 cm, through 1H-3, 33 cm
Depth: 0–3.33 mbsf
Age: Holocene–(?) late Pleistocene
Lithology: foraminifer-bearing clay

Lithostratigraphic Unit I consists of foraminifer-bearing greenish gray clay. As estimated from smear slides, the foraminifer concentrations are low (probably <5%), but they are visible to the naked eye on the split core. This unit is characterized by relatively high spectrophotometric lightness values (Fig. **F10**).

Unit II

Interval: Sections 308-U1319C-1H-3, 33 cm, through 3H-3, 25 cm
Depth: 3.33–17.25 mbsf
Age: late Pleistocene
Lithology: clay with fine sand laminae

Lithostratigraphic Unit II is composed of clay with fine sand laminae and organic-rich black clay. We divided the unit into four subunits.

Subunit IIA (3.33–6.2 mbsf)

Lithostratigraphic Subunit IIA is characterized by clay with silt laminae <1 cm thick. In the interval of Subunit IIA, the sediment undergoes a color change from gray-green to black. Smear slides suggest that silt laminae are dominated by quartz with minor amounts of carbonate and organic matter. Some silt beds are black and may include significant amounts of organic matter and associated pyrite.

Subunit IIB (6.2–12.0 mbsf)

The top of lithostratigraphic Subunit IIB is defined just below a silt lamina at 6.2 mbsf. Subunit IIB is

mostly composed of homogeneous black, organic-rich clay (Fig. F11) and records some of the lowest spectrophotometric lightness values (Fig. F10). The black clay rapidly oxidized after opening; it had turned green 24 h after splitting when the close-up core photographs were taken. Only the first millimeters at the surface were oxidized; the original color was preserved within the sediment.

Subunit IIC (12.0–14.0 mbsf)

Lithostratigraphic Subunit IIC is a thin, 2 m thick interval consisting of green clay with silt and fine sand laminae as thick as 1 cm (Fig. F12). Laminae are locally graded. Subunit IIC includes rare shell fragments and mud clasts.

Subunit IID (14.0–17.25 mbsf)

Lithostratigraphic Subunit IID is greenish gray clay, intensely bioturbated, and lacking sand and silt laminae. Foraminifers were not macroscopically visible in this subunit. Subunit IID is interpreted as a transitional unit between the turbidite unit above and the foraminifer-bearing Unit III below.

Unit III

Interval: Sections 308-U1319C-3H-3, 25 cm, through 3H-8, 22 cm
Depth: 17.25–23.5 mbsf
Age: late Pleistocene
Lithology: foraminifer-bearing clay

Lithostratigraphic Unit III consists of intensely bioturbated dark gray to greenish gray clay with foraminifers macroscopically visible on the split core face. The overall percentage of foraminifers is estimated at <5%. However, analysis of smear slides commonly indicates the presence of broken carbonate grains in the sediment. A distinct 2 cm thick ash layer occurs at 22.73 mbsf (Fig. F13). Analysis of smear slides indicated the ash is principally composed of undevitrified volcanic glass (Fig. F14). Overall, Unit III shows relatively high values of spectrophotometric lightness. A sharp drop in lightness values defines the base of the unit, even though this lightness extends deeper than the limit of obvious presence of foraminifers in the cores.

Unit IV

Interval: Sections 308-U1319C-4H-1, 0 cm, through 4H-4, 150 cm
Depth: 23.5–29.5 mbsf
Age: late Pleistocene
Lithology: clay with very fine sand laminae

Lithostratigraphic Unit IV is composed dominantly of green clay with a central section of very fine sand and silt laminae and beds with local grading. Unit IV shows a lower degree of lightness than the flanking foraminifer-bearing clays.

Unit V

Interval: Sections 308-U1319C-4H-5, 0 cm, through 4H-6, 150 cm
Depth: 29.5–31.0 mbsf
Age: late Pleistocene
Lithology: foraminifer-bearing clay

Lithostratigraphic Unit V consists of foraminifer-bearing clay and a thin (3 cm thick) foraminifer sand bed. Although thin, Unit V shows a distinctive narrow peak in spectrophotometric lightness (Fig. F10). Smear slides show a clear dispersed carbonate component in the clay.

Unit VI

Interval: Sections 308-U1319C-4H-7, 0 cm, through 18X-7, 29 cm
Depth: 31.0–155.8 mbsf
Age: late Pleistocene
Lithology: clay

Lithostratigraphic Unit VI comprises greenish gray to reddish brown clay (Fig. F15). The major lithology of the unit is punctuated by dark gray to black, locally pyritic layers, ranging from millimeters to centimeters in thickness. The greenish gray and reddish brown clays are locally distinct and range from ~1 to several decimeters thick. More commonly these layers are disrupted by burrowing, imparting an overall mottled appearance to the unit.

Smear slide analysis

Smear slides are a valuable tool to identify mineralogical and biological constituents in core. Because the process of making the smear slides may not preserve relative percentages of components and any estimates of percentages are qualitative, the data have to be used with care. Nevertheless, the compiled results (Fig. F16) clearly show diagnostic features of particular units. For example, the ash layer of lithostratigraphic Unit III is dominantly volcanic glass, foraminifers are evident in smear slides from Units I and III, and a consistent organic component is present in the lower portion of Unit III.

Interpretation of lithostratigraphy

Interpretation by unit

Lithostratigraphic Unit I is enriched in planktonic foraminifers and lacks any turbidite beds or laminae; it is thus interpreted as Holocene drape. With a thickness of 3.33 m, Unit I is only slightly thinner

than the thickness of a similar lithology observed in piston cores from this area by Mallarino et al. (in press).

The subunits of lithostratigraphic Unit II provide a link to at least three major events in the history of this basin. The thin, locally graded sand and silt laminae of Subunit IIA indicate turbidite influx during deposition. As such, it correlates with the major phase of turbidite accumulation represented by the wedge-shaped fan structure that has prograded from the northeast (Beaubouef et al., 2003). The black organic-rich clays of Subunit IIB suggest a period of abundant organic matter input. The homogeneous nature of Subunit IIB, the complete absence of laminae and other sedimentary structures, and the presence of wood fragments suggests that it was emplaced rapidly, perhaps as a single event bed. We tentatively interpret this unit to be the result of a mass transport deposit (MTD), although additional shore-based analyses are needed to confirm this interpretation. Turbidite influx into the basin occurred during accumulation of lithostratigraphic Subunit IIC. Although only 2 m thick, Subunit IIC correlates with an acoustically reflective unit in the basin center, which is interpreted to be the result of turbidity current deposition (see **"Lithostratigraphy"** in the "Site U1320" chapter) (Mallarino et al., in press; Beaubouef et al., 2003). Subunit IID lacks evidence of turbidite deposition and is transitional to Unit III.

Lithostratigraphic Unit III, characterized by microfossil-bearing clay and lacking turbidite features, suggests a period of hemipelagic sedimentation. Unit III correlates with a hemipelagic unit of Mallarino et al. (in press) that drapes over preexisting units in high-resolution seismic profiles. Unit III (6.25 m thick) is marginally thinner than the 8–10 m thickness observed by Mallarino et al. (in press) in piston cores. Unit III contains a distinctive 2.5 cm thick ash bed. This same ash bed has been observed in a nearby piston core and was interpreted as ash Layer Y8, representing the fallout from the Los Chocoyos (Guatemala) eruption at 84 ka (Mallarino et al., in press; Drexler et al., 1980).

Lithostratigraphic Unit IV, characterized by clay with very fine sand laminae, records another pulse of turbidite input to the basin.

Lithostratigraphic Unit V, a thin foraminifer- and nannofossil-bearing clay, records a period of minimum siliciclastic input to the basin and hemipelagic-dominated sedimentation. Given the occurrence of the ash Layer Y8 above, we tentatively assign this interval to the last interglacial (marine isotope Stage [MIS] 5e).

Finally, lithostratigraphic Unit VI is a thick and monotonous interval dominated by bioturbated clay with rare foraminifers and lacking obvious evidence of sandy turbiditic input. The faint color banding (greenish gray and black) of the organic-rich clays is interpreted to represent fluctuations in organic matter and siliciclastic input. The general lack of coarse (silt and sand) grains suggests deposition from muddy plumes or from a nepheloid layer.

Summary interpretation

Because Site U1319 is at the edge of Brazos-Trinity Basin IV, its sedimentary section is extremely condensed and minimally influenced by turbidite influx to the basin. Nevertheless, subtle but interpretable sedimentary signals are present. Overall, the sediments at Site U1319 show an alternation of turbiditic and hemipelagic deposition in a basin-margin setting. Accumulation of the first and fifth hemipelagic units (lithostratigraphic Units I and V) is related to the major sea level highstands at the present and at ~125 ka. These units bracket another interval of hemipelagic input (lithostratigraphic Unit III), which represents a significant pause in turbidity current influx to this basin margin site.

Biostratigraphy

Calcareous nannofossils and planktonic foraminifers are generally common to abundant and well preserved in samples from Cores 308-U1319A-1H to 4H and become rare further downhole. Benthic foraminifers are few to common with good preservation in Hole U1319A and are overall far less abundant than planktonic foraminifers in the upper 30 m of Hole U1319A.

Sediments recovered from Site U1319 range in age from Holocene to late Pleistocene, spanning approximately the last 150 k.y. No obvious hiatuses were detected. Nannofossil QAZ1 *Emiliania huxleyi* Acme Zone and QAZ2 Transitional Zone, as well as planktonic foraminifer Zones W, X, Y, and Z were identified (Fig. **F17**). The rarity of nannofossils and planktonic foraminifers below ~30 mbsf hampered biostratigraphic resolution in this part of the hole.

Benthic foraminifers identified in Hole U1319A are dominated by species mainly living in low-oxygen, nutrient-rich environments. This is consistent with the muddy lithology described as fine-grained turbidites (see **"Lithostratigraphy"**). The distinction of a *"Laticarinina"* assemblage in the 20–30 mbsf interval indicates a normal lower bathyal setting.

Sedimentation rates were relatively low in the uppermost Pleistocene (0.97 m/k.y.) to Holocene (0.15 m/k.y.). Pending further stratigraphic precision, sedimentation rates below 24 mbsf (equivalent to the

last ~150–90 k.y.) appear to have been much higher (>2.31 m/k.y.).

Calcareous nannofossils

We examined all core catcher samples and one additional sample from interval 308-U1319A-4H-5, 9–13 cm, for calcareous nannofossils. Quantitative nannofossil data and their general distributions are presented in Figures F18 and F19. All samples yielded rare to very abundant nannofossil assemblages. A general reduction in abundance is seen toward the bottom of the hole. The interval from the seafloor to Sample 308-U1319A-4H-5, 84–88 cm, has a very abundant nannofossil assemblage. Downhole from Sample 308-U1319A-4H-CC, the assemblages vary from abundant to rare. Preservation is good to moderately good throughout the section. Samples with poor preservation are typically coarser grained with low overall abundance. Nannofossil assemblages contain in situ and reworked species. The most dominant in situ species are *E. huxleyi, Gephyrocapsa aperta,* and *Gephyrocapsa ericsonii*. *Gephyrocapsa oceanica* is always more abundant than *Gephyrocapsa caribbeanica* and contributes <5% of the total abundance. The great majority of reworked species are Cretaceous in age (>99%), and they occur throughout the cored section.

We divided the cored interval into two main zones, the QAZ1 *E. huxleyi* Acme and QAZ2 Transitional Zones based on the nannofossil stratigraphic subdivision of Hine and Weaver (1998).

QAZ1 *E. huxleyi* Acme Zone

We identified this zone in Samples 308-U1319A-1H-CC and 2H-CC based on the dominant abundance of *E. huxleyi* (approximately >70% of total abundance) (Fig. F18). According to Berggren et al. (1995), the first occurrence datum of *E. huxleyi* acme is at 90 ka. During this time, *Syracosphaera* spp. became more abundant in comparison with the lower interval of the hole, where they varied from abundant to common. Reworked Cretaceous assemblages are abundant in this part of the section.

QAZ2 Transitional Zone

This zone was distinguished in Samples 308-U1319A-3H-CC to 18H-CC (Fig. F18). It is characterized by the dominance of *G. aperta-G. ericsonii*. Together, these two species form >90% of the overall abundance. Based on the distribution of different groups of nannofossils we distinguished Subzones A, B, and C within the QAZ1 Transitional Zone.

QAZ1 Subzone A

Subzone A is defined based on the presence of *G. aperta-G. ericsonii* and the absence of *E. huxleyi* (Fig. F18). The overall abundance of *G. aperta-G. ericsonii* may be up to 100,000 specimens per 100 fields of view. The *G. oceanica-G. caribbeanica* complex is common to abundant and forms the second dominant group of the assemblage. *Scapholithus fossilis* and *Umbilicosphaera* spp. are more abundant in this unit. Subzone A is defined in Samples 308-U1319A-3H-CC and 4H-5, 9–13 cm. It is the uppermost subzone of the QAZ2 Transitional Zone.

QAZ2 Subzone B

This subzone is distinguished by the common overall abundance of *G. aperta-G. ericsonii,* and reworked Cretaceous specimens form <50% of the total abundance. Samples 308-U1319A-4H-CC through 9H-CC were assigned to Subzone B.

QAZ2 Subzone C

Subzone C is defined by the dominance of reworked Cretaceous assemblages that form >50% of the total abundance. It is defined in Samples 308-U1319A-10H-CC to 18H-CC. The other common group of the assemblage is *G. aperta-G. ericsonii*. This subzone has the lowest abundance of in situ species throughout the entire section.

Planktonic foraminifers

The preservation of foraminifers in Hole U1319A is excellent overall. Semiquantitative planktonic foraminifer data are presented in Table T5. Samples from above Section 308-U1319A-4H-5 contain common to abundant planktonic foraminifers, although they are rarer in Sample 2H-CC, 22–24 cm. Samples from Section 308-U1319A-4H-CC and below contain rare planktonic foraminifers.

The planktonic foraminifer assemblage is dominated by *Globigerinoides ruber* (both the pink and white forms) with lesser amounts of *Globigerinoides sacculifer*, *Globigerinoides conglobatus*, *Neogloboquadrina dutertrei, Globorotalia truncatulinoides, Globorotalia menardii, Globorotalia tumida, Globorotalia flexuosa* (older than 68 ka), *Globorotalia inflata* (older than 10 ka), *Globorotalia crassaformis, Globigerinella siphonifera, Orbulina universa, Globigerina bulloides, Globigerina falconensis,* and *Pulleniatina obliquiloculata*. There are traces of many other taxa, such as *Globigerinita glutinata, Hastigerina pelagica,* and *Globigerinella calida*.

The Pleistocene zonation of Ericson and Wollin (1968), based upon the presence or absence of the

warm-water species *G. menardii* and allied species for the Gulf of Mexico, and as modified by Kennett and Huddlestun (1972), was applied to the fossil succession in Hole U1319A. Consequently, planktonic foraminifer assemblage Zones W, X, Y, and Z were identified, suggesting that the sediment recovered from Hole U1319A was deposited during the last 180 k.y. (Fig. F20). These results are similar to the findings of Kohl (1985) from Pigmy Basin and of Mallarino et al. (in press) from the western margin of Brazos-Trinity Basin IV.

Zone Z

This zone is represented only by Sample 308-U1319A-1H-CC, 15–20 cm (Fig. F20). The planktonic foraminifer assemblage is characterized by abundant *G. menardii* and *G. ruber* and other warm-water species. It can be distinguished from Zone X by the absence of both *G. flexuosa* and *G. inflata*. According to Berggren et al. (1995), the last occurrence datum of *G. flexuosa* was at 68 ka.

Zone Y

A distinct cool-water assemblage underlies the Zone X sample and can be assigned to Zone Y (Sample 308-U1319A-2H-CC, 22–27 cm) (Fig. F20). This assemblage includes mainly *G. inflata, G. ruber, G. crassaformis,* and *G. siphonifera*. *G. menardii* or its allied species (*G. tumida* and *G. flexuosa*) were not recorded from this zone. According to Kennett and Huddlestun (1972) and Martin et al. (1990), Zone Y can be divided into Subzones Y1–Y8 and represents MIS 2 to upper MIS 5 (10.5–90 ka). Just above the Zone X/Y boundary at 22.73 mbsf the distinct 2 cm thick ash Layer Y8 bears an age of ~84 ka (Drexler et al., 1980).

Zone X

Zone X was recognized in Samples 308-U1319A-3H-CC, 17–22 cm, 4H-5, 9–13 cm, and 4H-5, 84–88 cm (Fig. F20). It contains abundant warm-water planktonic foraminifers typified by *G. menardii, G. tumida, G. flexuosa, G. crassaformis, G. truncatulinoides*. *G. siphonifera, N. dutertrei, P. obliquiloculata, Orbulina universa, G. ruber, G. sacculifer, G. conglobatus,* and *G. falconensis*. The cool-water species *G. inflata* is absent from this zone. According to Kennett and Huddlestun (1972) and Martin et al. (1990), Zone X can be divided into Subzones X1–X5 and represents MIS 5c–5e with an age of 90–129 ka (see **"Biostratigraphy"** in the "Methods" chapter).

Zone W

Zone W is characterized by the presence of *G. inflata* and the absence of *G. menardii* and other warm-water species in a less thriving assemblage (Fig. F20). Sample 308-U1319A-5H-CC, 36–41 cm, and remaining samples downhole were assigned to Zone W. According to Kennett and Huddlestun (1972), Zone W can be divided into Subzones W1 and W2 and represents MIS 6 (129–180 ka). Biostratigraphic subdivision of this interval could not be achieved shipboard because planktonic foraminifers were rare.

Benthic foraminifers

The benthic foraminiferal assemblages studied include mainly calcareous taxa and only few species and specimens of agglutinated taxa. The benthic foraminifers generally represent well-known neritic to "deepwater" taxa that prefer oxygen-poor, nutrient-rich environments (Phleger and Parker, 1951a, 1951b; Poag, 1981; Culver and Buzas, 1983; van Morkhoven et al., 1986). Semiquantitative benthic foraminifer data listed in Table T6 enabled recognition of two assemblages: the *Laticarinina* assemblage, representing a normal bathyal association, and the *Bolivina-Bulimina* assemblage, representing an assemblage preferring low-oxygen, high-nutrient environments. The relative abundances of selected species are presented in Figure F21.

Benthic foraminifers are moderately abundant in core catcher samples from Hole U1319A, although they are rare in comparison with planktonic foraminifers in Cores 308-U1319A-1H to 3H. Benthic foraminifer abundance drops significantly in samples from Core 308-U1319A-2H and below Core 10H, in which small, thin-shelled species are common. Preservation in most samples is good to very good, showing no signs of dissolution.

Laticarinina assemblage (Holocene MIS 1 and late Pleistocene MIS 5)

This is a well-diversified assemblage recognized in Cores 308-U1319A-1H, 3H, and 4H, characterized by the few or common occurrences of *Laticarinina pauperata, Cibicidoides wuellerstorfi, Uvigerina hispidicostata, Stilostomella lepidula, Cibicidoides* spp., *Sigmoilopsis schlumbergeri, Pyrgo* spp., *Sphaeroidina bulloides*, *Lenticulina* spp., and *Pullenia* spp (Fig. F21). Middle to lower bathyal paleodepths are indicated for this assemblage by the presence of *L. pauperata* and *P. wuellerstorfi*, generally found in water depths exceeding 1000 m (van Morkhoven et al., 1986).

Bolivina-Bulimina assemblage (late Pleistocene MIS 2–4 and MIS 6)

In Cores 308-U1319A-2H and 308-U1319A-5H through 18X, small thin-shelled species including *Bolivina spissa, Bolivina* spp., *Bulimina aculeata, Uvige-*

rina spp., *Fursenkoina bradyi*, and *Chilostomella ovoidea* dominate the assemblage (Fig. F21). Other species that may also occur are *Quinqueloculina* spp., *Gyroidina* spp., and *Oridorsalis tenera*. This assemblage indicates upper slope to lower bathyal depths, with the upper limit near 400 m (van Morkhoven et al., 1986). An infaunal habitat preference for most common species from this assemblage indicates low-oxygen, nutrient-rich environments (Poag, 1981). Rapid sediment accumulation causing stress conditions may also nurture similar assemblages.

Fluctuations in the relative abundance of such taxa as *Bolivina* spp., *Bulimina* spp. and *Fursenkoina bradyi*, observed in some of the samples (Fig. F21), may reflect cyclic changes in sediment input and/or circulation.

Age model and sedimentation rates

The age models developed during the expedition are preliminary. Biostratigraphic dating of Pleistocene sediments is difficult, and we had to rely on several assumptions to constrain age models and sedimentation rates. In the case of Site U1319, we took into consideration biostratigraphic, lithostratigraphic (ash layer events), and magnetostratigraphic tie points (Table T7). The magnetostratigraphic tie points were derived by matching the rock magnetic record with a global $\delta^{18}O$ curve (see "Paleomagnetism" in the "Methods" chapter), and they are thus very interpretative. However, at Site U1319 the trend in paleomagnetic tie points matches the trend obtained by linking biostratigraphic with lithostratigraphic datums (Fig. F22). All of the datums are recorded in the uppermost 30 m. The deepest datum at ~30 mbsf is a magnetic tie point with an age of ~122 ka. Fitting one line through all the data points from the uppermost 30 m yields an estimated sedimentation rate for this interval of ~0.2 m/k.y. (Fig. F22). No stratigraphic datums were recorded below 30 mbsf at this site. However, we make the assumption that since no occurrence of *Helicosphaera inversa* was recorded, the oldest sediment recovered is younger than the last occurrence (LO) of *H. inversa* (LO = 150 ka). This assumption implies that sediment below 30 mbsf accumulated at a rate of 5 m/k.y. More extensive postcruise work is needed to confirm this interpretation.

Paleomagnetism

Archive halves from Hole U1319A were measured on the pass-through cryogenic magnetometer using a peak alternating-field (AF) demagnetization field of 30 mT (Table T8). Cores 308-U1319A-1H to 13H were cored with the APC and Cores 3H through 13H were oriented using the Tensor tool. Cores 308-U1319A-14X through 18X were cored using the XCB and were not oriented (see "Operations"). XCB drilling is less suitable for paleomagnetic studies because of drill string overprints and core disturbance. The peak field of 30 mT is assumed to have removed the viscous magnetic overprint induced by the drill string (Flood, Piper, Klaus, et al., 1995; Shipboard Scientific Party, 1996).

Paleomagnetic intervals

Hole U1319A was divided into three paleomagnetic intervals.

Interval 1 (0–37 mbsf)

Natural remanent magnetization after AF demagnetization at 30 mT (NRM_{30mT}) intensities in paleomagnetic Interval 1 range between ~0 and 0.015 mA/m (Fig. F23A). Between 0 and 16 mbsf, NRM_{30mT} values are slightly higher than those between 17 and 37 mbsf. Declination ranges between 30° and 150° throughout Interval 1 except between 5 and 15 mbsf (Core 308-U1319A-2H), where declination values center around 250°. This peak is unreliable because the Tensor tool correction could not be applied for Core 308-U1319A-2H (Fig. F23B). The inclination shows normal polarity within the Brunhes Chron throughout all of Interval 1 with the exception of spurious outlying data points (e.g., at ~15 mbsf), which are interpreted as noise (Fig. F23C).

Interval 2 (37–47 mbsf)

Paleomagnetic Interval 2 has average NRM_{30mT} intensity values ranging between 0.005 and 0.01 mA/m (Fig. F23A). NRM_{30mT} intensity in Interval 2 corresponds (see "Lithostratigraphy") to reddish clay layers (Fig. F24A), suggesting enhanced iron oxide precipitation in this interval. These layers correspond to declination of ~120° (Fig. F23B). The inclination shows normal polarity within the Brunhes Chron throughout Interval 2 (Fig. F23C).

Interval 3 (47 mbsf–TD)

NRM_{30mT} values in paleomagnetic Interval 3 average 0.005 mA/m with a maximum value around 0.01 mA/m (Fig. F23A). Magnetic susceptibility values in Interval 3 (Fig. F25C, F25D) correspond to an interval with increased iron oxide content within reddish clay layers and silt laminae (see "Lithostratigraphy;" Fig. F24B). Declination directions generally range between 30° and 150°, similar to Interval 1 but with considerably more scatter (Fig. F24B). The inclination record of Interval 3 shows random orientations, which might be related to possible postdeposi-

tional iron oxide formation or a generally disturbed signal in this part of the core. These values are therefore not shown in Figure F23C and are not discussed further.

The Lake Mungo and Blake events or the Laschamps Excursion (Freed and Healy, 1974; Stupavsky and Gravenor, 1984; Flood, Piper, Klaus, et al., 1995; Cisowski and Hall, 1997) could not be identified in Hole U1319A.

Magnetostratigraphy

In general, the NRM_{30mT} intensity signal correlates with the magnetic volume susceptibility and magnetic point susceptibility (acquired using the magnetic susceptibility core logger [MSCL] on the multisensor track [MST] and MS2F sensors, respectively) as well as with bulk density (Fig. F25). Magnetostratigraphic tie points (MTPs) are identified using the multiparameter correlation described in "Paleomagnetism" in the "Methods" chapter. We recognized MTP1–MTP8 for Interval 1 and MTP9–MTP12 for Intervals 2 and 3 (Table T9).

Preliminary magnetostratigraphic interpretation for Interval 1 in Hole U1319A was achieved by correlating the magnetostratigraphic tie points to MIS 3.1–5.5 (Bassinot et al., 1994). In addition, ash Layer Y8 at 22.7 mbsf (see "Lithostratigraphy") supports the correlation of MTP4–MTP8. The magnetostratigraphic tie points were included in the preliminary age model (see Fig. F22) and constrain the upper 30 mbsf (lithostratigraphic Units I–V) of the sediment column to an age range of 0 to ~122 ka (MIS 5.5 to recent). As a first approach, individual peaks of NRM_{30mT} intensity, magnetic susceptibility, and bulk density of the lowermost part of Hole U1319A (from ~30 mbsf downhole) were matched with MTP9–MTP12, the latter probably belonging to MIS 6 (Fig. F25). This lowermost depth interval is entirely within lithostratigraphic Unit VI.

Geochemistry and microbiology

Inorganic geochemistry

Interstitial water chemistry

Interstitial water chemistry results are listed in Table T10 and shown in Figures F26, F27, F28, and F29.

Alkalinity was widely variable throughout Hole U1319A, ranging from a minimum value of 2.95 to a maximum of 19.45 mM (Table T10). Alkalinity increases to the peak concentration of 19.45 mM at 13.5 mbsf and then decreases ~4 mM at 40 mbsf. Below this depth alkalinity remains constant at ~4 mM (Fig. F26). Interstitial water pH varies from 7.18 to 7.84. The pH depth profile is similar in downhole variation trends to alkalinity but with different maxima depths. The pH maximum, at 24–36 mbsf, is below the alkalinity concentration maximum depth (15 mbsf). Below 50 mbsf, pH remains approximately constant, but with a slight downhole increase from 7.3 to 7.5 (Fig. F26).

Salinity varies from 3.2 to 3.7 parts per hundred (pph) (Table T10). Salinity decreases significantly downhole from the seafloor to ~20 mbsf. Below this depth, salinity shows more limited but irregular variation between 3.2 and 3.5 pph. A low salinity of 3.2 pph is again reached at ~110 mbsf, corresponding to a high methane content peak in this interval. Interstitial water chlorinity values are mostly ~560 mM, similar to the standard seawater value (559 mM), but several mimima are observed, the lowest value of 516 mM is coincident with the salinity minimum at 110 mbsf (Fig. F26).

The dissolved SO_4^{2-} profile dramatically decreases from 26 mM at the seafloor to ~0.5 mM below 15 mbsf and then increases slightly downhole to 2.1–2.9 mM at the bottom of the core (Fig. F27). The sulfate/methane interface (SMI) is estimated to occur at 15 mbsf. Dissolved NH_4^+ concentration increases from 291 to 4411 µM downhole, although a mimimum occurs at 33 mbsf (Fig. F27). The depth profile for dissolved Si^{2+} is irregular, but slightly higher values occur at shallower depths (Fig. F27). Dissolved PO_4^{3-} concentrations are highest at shallow depths, with a maximum value of 75.2 µM at 13.5 mbsf, which corresponds to the alkalinity maximum (Table T10). Below 40 mbsf, PO_4^{3-} concentrations are generally low (several micromolar concentration) (Table T10).

The depth profile of Na^+ is very irregular with several mimima at 13.5, 40.5, 53.5, and 133 mbsf (Fig. F28). Na^+, K^+, Mg^{2+}, and Ca^{2+} profiles decrease similarly at shallow depths, reaching mimima at ~13.5 mbsf, corresponding to alkalinity and PO_4^{3-} maxima at this depth. Below this depth, K^+ and Mg^{2+} increase slightly and then decrease to TD. In contrast, Ca^{2+} increases to a maximum at 90 mbsf and then decreases slightly to the bottom of the hole. However, the sample from Section 308-U1319A-16X-3 at 133 mbsf shows distinct concentration minima for Na^+, Mg^{2+}, and Ca^{2+} relative to the respective downhole trends (Fig. F28).

Concentration-depth trends of B^{3+} and Ba^{2+} are similar to those of alkalinity and pH, with a peak at ~13.5 mbsf (Fig. F29). The dissolved Li^+ depth profile is similar to those of K^+ and Mg^{2+}, and the Sr^{2+} profile mimics variations in Ca^{2+} (Fig. F29). The depth profile for dissolved Fe^{2+} is irregular, but slightly higher values are present at shallower depths. Mn^{2+} concentrations in interstitial water show a trend similar to

that of SO_4^{2-}; namely, Mn^{2+} concentrations decrease from 147 µM at the seafloor to 5 µM at 12 mbsf, followed by a small peak between 15 and 30 mbsf with values as high as 23.9 µM. Below this depth Mn^{2+} content remains extremely low (<4.0 µM) (Fig. **F29**).

In summary, interstitial water chemical compositions show great variability at shallow depths with maximum or minimum values centered at ~15 mbsf, which is coincident with lithostratigraphic Subunit IIB, homogeneous black clay. The sharp pore water chemistry changes at this very shallow subseafloor depth suggest very rapid anaerobic degradation of organic matter through sequential redox reactions within the uppermost 15 mbsf. Sulfate reduction of organic matter in this shallow interval is likely the cause for the decrease in SO_4^{2-} concentrations and the increases in alkalinity, PO_4^{3-}, and Ba^{2+} concentrations (e.g., Gieskes, 1983). The upper zone of increased alkalinity (centered at ~13.5 mbsf) coincides with decreases in Ca^{2+}, Mg^{2+}, and Sr^{2+} ions, which may suggest precipitation of diagenetic carbonates within this interval (e.g., Baker and Burns, 1985).

Solid-phase chemistry

Initial results for total inorganic carbon (TIC), total organic carbon (TOC), total nitrogen, and total hydrogen analyses on sediment squeeze cakes are listed in Table **T11** and presented in Figure **F30.** TIC concentrations are highly variable throughout the hole, ranging from 0.87 to 4.08 wt%. The lowest concentration of TIC (0.16 wt%) occurs between 25 and 26.5 mbsf, directly below the highest peak in TIC content of 3.56 wt% at 23.5 mbsf. TIC concentrations initially decrease to ~1 wt% within the upper 39 mbsf, approaching an average concentration of 2.49 wt% below 39 mbsf to TD.

TOC content ranges between 0.16 and 1.9 wt% (average = 0.75 wt%). The result of 0 wt% for the sediment interval collected at 36 mbsf is an artifact of the method used to calculate TOC, where

$$TOC = TC - TIC,$$

and is not included in the data analysis. The TOC curve exhibits two concentration maxima at 6–13.5 and 34.5–39 mbsf, with maximum respective values of 1.06 and 1.9 wt%. TOC concentrations below 39 mbsf decrease to 0.67 wt% at TD.

Downhole variation is minimal in total nitrogen and hydrogen contents. Nitrogen contents range from 0.17 to 0.28 wt% (average = 0.23 wt%). Hydrogen concentrations range between 0.49 and 1.06 wt% (average = 0.77 wt%).

The molar ratio of organic carbon to total nitrogen (C/N) ranges from 0.88 to 8.5 (excluding results from 36 mbsf) and averages 3.77. C/N ratios tended to be higher within depth intervals 4.3 to 13.5 mbsf and 33.1 to TD, corresponding to respective lithostratigraphic Units II and VI.

Solid-phase initial interpretations

Comparison of organic and inorganic carbon concentrations with lithology suggests a relationship between carbon content and lithostratigraphic units. The TOC peak between 6 and 13.5 mbsf (Fig. **F30**) coincides with lithostratigraphic Subunit IIB, a homogeneous black clay. Elevated TOC concentrations are also observed between 34.5 and 39 mbsf within the upper portion of lithostratigraphic Unit IV. TIC maxima at 1.5 and 23.5 mbsf agree with sediment lightness in foraminifer-rich Units I and III (Figs. **F9, F10**). Coincidence between peaks in TIC contents and foraminifer-rich lithostratigraphic Units I and III suggests that carbon within these units is predominately inorganic.

The average C/N of 3.77 is indicative of organic matter derived primarily from algal material (Fig. **F30**). Marine organic matter has a C/N range of 4–10 compared to the typically high ratios (>20) associated with terrigenous organic matter (e.g., Bouloubassi et al., 1999). Conversely, C/N ratios <5 may suggest low-productivity conditions or poor preservation (e.g., Bouloubassi et al., 1999). The C/N maximum (5.92) observed at 13.5 mbsf is coincident with the black clay in lithostratigraphic Subunit IIB (Fig. **F9**). A second maximum C/N ratio of 8.53 at 34.5 mbsf suggests an organic-rich component in lithostratigraphic Unit VI (Fig. **F9**). High ratios (>8) may result from input of terrestrial material or preferential degradation of nitrogenous matter during early diagenesis (e.g., Bouloubassi et al., 1999). Bulk carbon and nitrogen isotopic analyses can provide an additional constraint with which to better access the significance of C/N ratios observed in the Gulf of Mexico.

Organic geochemistry

Hydrocarbon gas composition

Methane was the predominant hydrocarbon present in all cores of Hole U1319A. Concentrations of methane and ethane are shown in Table **T12.** Very minor amounts of ethane (~0.7 ppmv) were detected in a few sections, and no higher hydrocarbons were detected. The presence of only methane suggests that the hydrocarbon gas is a result of biogenic production rather than of thermogenic origin. The vertical distribution of headspace methane is shown in Figure **F31.** Methane concentrations fluctuate with depth; the highest concentration of methane (11,310 ppmv) occurs at 29 mbsf. Below this depth, methane concentrations decrease until 105 mbsf.

Slight increases in methane concentrations are again observed between 105 and 153 mbsf. The SMI is estimated to occur at 15 mbsf, as shown in Figure F32.

Microbiology

Biomass enumeration

Samples for prokaryotic cell enumeration were taken from microbiology whole-round core samples (Table T13). Whole rounds were collected every ~4 m between 4.27 and 21.5 mbsf (5 samples), every ~9 m between 21.5 and 117.3 mbsf (10 samples), and every ~20 m between 117.3 and 152.4 mbsf (2 samples). The highest biomass was found near the seafloor (4.4 mbsf), which contained 1.2×10^6 cells/mL, and the number of cells decreased with depth in general (Fig. F33). The biomass depth profile is similar to results from previous Ocean Drilling Program (ODP) legs (Parks et al., 1994; D'Hondt, Jørgensen, Miller, et al., 2003; Newberry et al., 2004). However, there were several features observed in the vertical profile at this site. One was the significantly lower biomass compared to previous reports and the other was the drastic decrease in cell numbers near the seafloor (17 mbsf), $<1.0 \times 10^5$ cells/mL. Considering the geological setting of this site and the low sedimentation rates, energy supply scarcity could be a possible reason for the low biomass and the drastic decrease in cell numbers in near-seafloor sediments. In addition, we observed an anomalously high biomass (1.2×10^5 cells/mL) at 37.5 mbsf, consistent with an increase in TOC concentrations (34.5 and 39 mbsf).

Physical properties

At Site U1319, laboratory measurements were performed to provide a downhole profile of physical properties at a reference site in Brazos-Trinity Basin IV. Fractures and voids that resulted from gas expansion, especially between 60 and 120 mbsf, degraded MST measurements. *P*-wave velocity logger (PWL) measurements were aborted after logging four cores unsuccessfully.

Density and porosity

Gas expansion and elastic recovery of clays were observed on the cores obtained at this site from 30 mbsf and deeper. This phenomenon reduces the bulk density from that in situ and, consequently, porosity is overestimated relative to in situ conditions. This error is assumed to be relatively small, and the data remain useful for interpretation and correlation. The downhole trends in gamma ray attenuation (GRA), measurement while drilling (MWD), and moisture and density (MAD) profiles correspond well (Fig. F34A). However, GRA densities are slightly higher in the uppermost 30 mbsf and slightly lower below 70 mbsf (the difference may be as much as 0.2 g/cm³). GRA density data also show considerably more scatter at all depths (Fig. F34A). Results from previous ODP legs typically exhibit higher MAD bulk densities compared to GRA densities. These differences have been attributed to differences in core diameter (e.g., Moore, Taira, Klaus, et al., 2001), but at this site the role of gas expansion cannot be disregarded. Compared to the MAD data, the MWD data underestimate density in the uppermost 30 mbsf, probably because of the larger borehole diameter in this section. MWD densities are slightly higher than MAD bulk densities below 70 mbsf. The lower MAD densities may be explained by expansion of the cores in the laboratory.

The following interpretation of density variations is based on MAD data. Bulk densities in lithostratigraphic Unit I (0–3.33 mbsf) increase rapidly with depth from 1.32 to 1.8 g/cm³ (Fig. F34A). Grain densities vary from 2.41 g/cm³ at the top of the unit to 2.74 g/cm³ at the bottom (Fig. F34B). The lowest values are probably due to the presence of organic matter that has a lower grain density relative to minerals. Porosities rapidly decrease from 81% at the top to ~60% at the bottom of this unit (Fig. F34C).

Low bulk densities in lithostratigraphic Unit II (3.33–17.25 mbsf) are correlated to low grain densities (e.g., 2–2.5 g/cm³) (Fig. F34). These grain densities were remeasured and the low values were confirmed. This change in grain density corresponds with lithostratigraphic Subunit IIB, a homogeneous black clay, rich in organic matter (see "Lithostratigraphy"). A bulk density peak at 1.6 g/cm³ in lithostratigraphic Subunit IIC correlates with the presence of silty laminae. Lithostratigraphic Subunit IID and Units III and IV show gradual increases in bulk density from 1.55 to 1.65 g/cm³ down to 26 mbsf, corresponding to additional silt laminae and thin beds. This increase in density is mirrored by a decrease in porosity from ~70% to 62% (Fig. F34C).

In Lithostratigraphic Unit V (29.5–31 mbsf) bulk densities measured by MAD, MST, and MWD all recorded sharp increases from ~1.59 g/ cm³ at the top to ~1.75 g/cm³ at the base. There is fairly wide scatter in grain density measurements including a peak value of 2.78 g/cm³. Porosity declines rapidly from ~70% at the top to ~60% at the base, a 10% drop in only 1.5 m.

In lithostratigraphic Unit VI (31–156 mbsf), bulk densities increase from 1.57 to 1.99 g/cm³ (Fig. F34A). As density increases, porosity decreases from 65% to 44.5% within this unit (Fig. F34C), with a single major shift occurring at ~80 mbsf, where den-

sity is down to 0.1 cm^3 lower than surrounding values. Grain densities range from 2.62 to 2.8 g/cm^3, but the overall trend remains near constant around a mean value of 2.74 g/cm^3 (Fig. F34B). Cores 308-U1319A-14X through 18X were cored using the XCB. MAD and GRA bulk densities are lower than MWD bulk densities in these cores (Fig. F34A). The difference between measurements shows that coring methodology may affect bulk density.

Noncontact resistivity

Noncontact resistivity (NCR) increases with depth in lithostratigraphic Units I, II, and III, with local resistivity peaks (Fig. F35A) that correlate to silty sediments (see "Lithostratigraphy"). In lithostratigraphic Units IV and V, NCR increases to 1.4 Ωm. This increase is followed by a slight decrease at ~40 mbsf near the top of lithostratigraphic Unit VI. NCR is constant at ~0.9 Ωm to TD. This pattern mirrors the porosity pattern derived from MAD data (Fig. F34C).

Magnetic susceptibility

Magnetic susceptibility increases from ~17 × 10^{-5} to ~30 × 10^{-5} with depth in lithostratigraphic Unit I (Fig. F35B). Lithostratigraphic Unit II has relatively constant values (~30 × 10^{-5} SI) with peaks superimposed. Two of these peaks correlate with silt layers (see "Lithostratigraphy"). Mudstones in lithostratigraphic Units III, IV, and V show variable magnetic susceptibilities centered at ~20 × 10^{-5} SI. In lithostratigraphic Unit IV, peaks correlate with silt and sand layers.

At the top of lithostratigraphic Unit VI (31–156 mbsf), magnetic susceptibility sharply increases and then remains relatively constant, with mean values centered at ~60 × 10^{-5} SI (Fig. F35B). This unit contains wide scatter, especially in the lower part of the section below 80 mbsf, where the lithology log shows alternation between reddish brown and greenish gray clay layers with interspersed pyritic dark gray clay layers. The magnetic susceptibility lows seem to be associated with the reddish brown clay layers.

Thermal conductivity

Thermal conductivity increases with depth (Fig. F36A). Measured thermal conductivities at 68 mbsf and below 117 mbsf are not considered in the analysis because these values are almost equal to the thermal conductivity of water at 25°C (0.58 W/[m·K]), which is considered too low in view of the sediment densities and porosities. Most likely the probe was not in full contact with the sediment and thus did not accurately measure thermal conductivity of fully saturated sediments. The resolution of measurements is low and data are relatively scattered, oscillating between 0.75 and 1.24 W/(m·K) (Fig. F36A).

P-wave velocity

Only velocity measurements above 30 mbsf were reasonable. Below this depth, voids within the core due to gas expansion compromised the measurements. Velocity measurements in the upper 15 m of cores, measured both longitudinally (PWS1) and perpendicular to the core axis (PWS2), are close to the velocity of water, reflecting high porosity (Fig. F36B). *P*-wave velocities increase with depth, and a small peak corresponds to the more silty material of lithostratigraphic Subunit IIA (see "Lithostratigraphy").

The x-axis (PWS3) measurements are lower than the y- (PWS2) or z- (PWS1) axis measurements (Fig. F36). These low values likely result from bad picks of the first arrival wavelet.

Shear strength

Undrained shear strengths increase with depth (Fig. F37A). The trend is approximately linear in the uppermost 80 mbsf, with a maximum value of 40 kPa and then suddenly increases and displays more erratic behavior, with values ranging from as high as 90 to as low as 40 kPa. Variations in peak shear strength increased when the coring method changed from APC to XCB, implying that the XCB coring process strengthens core material relative to the APC coring process. Peak shear strength measurements by both automated vane shear [AVS] and pocket penetrometer are quite similar (Fig. F37B). The sedimentary sequence below 80 mbsf appears to have low undrained shear strength in several intervals, possibly linked to the presence of weaker layers. The irregular undrained shear strength pattern observed in lithostratigraphic Unit VI is probably associated with a change in lithology in the lowest part of this unit (see "Lithostratigraphy"). The lower part of lithostratigraphic Unit VI alternates between greenish gray, reddish brown, and pyritic dark gray clay layers. Low sensitivity shows that most of the tested layers within the drilled section are nonsensitive (Fig. F37C). The high sensitivity observed at 147 mbsf is due to low residual shear strength.

The ratio between the measured undrained shear strengths and the vertical hydrostatic effective stresses derived from the sediment bulk densities and unit weights ranges between 0.025 and 0.1 (Fig. F38A). The increase in variation from ~115 mbsf downhole is probably due to disturbance by XCB coring. These ratios are relatively low, especially when compared to the values observed in the upper-

most sediment column for conventional piston cores.

Summary

Bulk densities generally increase linearly with depth from 1.3 to 2.0 g/cm³. Grain densities show relatively constant values (~2.7 g/cm³), except in the upper part of the sediment column where the presence of sediment with high organic matter content causes low densities. NCR and magnetic susceptibility also match variations in porosity and grain size.

Porosity measurements at this site show an approximately exponential trend with depth, with values decreasing from 80% to 45%. NCR measurements mirror porosities derived from MAD measurements. Silt-sand layers interbedded with clay are recognized in the NCR profile.

In lithostratigraphic Unit II, peak values of magnetic susceptibility are correlated to black clays containing pyritic minerals. In clay layers of lithostratigraphic Units III–VI, peak values correspond to silt and sand layers, indicating a change in mineral composition between these layers and the embedding clay.

Thermal conductivity values at Site U1319 are relatively low and the general trend is an increase with depth. Thermal conductivities increase from 0.75 to 1.24 W/(m·K) between 0 and 117 mbsf.

At Site U1319 undrained shear strengths tend to increase almost linearly with depth from 2 to ~80 kPa, as expected. Below 80 mbsf the sedimentary sequence is characterized by alternating clay layers of different colors, and undrained shear strength values show a more scattered pattern.

Downhole measurements

Site U1319 marked the first location drilled and the first time that logging while drilling (LWD) and measurement while drilling (MWD) operations were conducted during Expedition 308. The primary logging objectives in Hole U1319B were to

- Determine the extent and lateral variation of turbidite deposits,
- Correlate lithostratigraphic units to the southern flank of the basin, and
- Document the lateral change in petrophysical properties of sediments above seismic Reflector R60.

Logging while drilling and measurement while drilling

Operations

LWD operations began with the initial makeup of the BHA, tool initialization, and calibration. The LWD tools (17.1 cm collars) included the GeoVision Resistivity (GVR) tool with a 23.2 cm button sleeve, MWD (Powerpulse), Array Resistivity Compensated (ARC) tool, and Vision Density Neutron (VDN) tool. Memory and battery life allowed for ~40 h of drilling without circulation; when circulating at rates >375 gallons per min (gpm), battery power is not used. Hole U1319B was spudded at 1440.6 meters below rig floor (mbrf) 20 m north of Hole U1319A. Drilling proceeded at a rate of penetration (ROP) of ~30 m/h to a total depth of 180 mbsf. Real-time data were transmitted to the surface at 24 Hz during a total of 7 drilling hours. From 0–15 mbsf bit rotation was ~50 rpm and pump rates were ~80 gpm. At 1454 mbrf, pump rates were increased to ~395 gpm and the mud pulsing system began transmitting data to the surface. At 1616 mbrf, 150 bbl of 12.2 ppg water-based mud (seawater, sepiolite, and barite) was displaced into the hole. Hole U1319B was drilled 22.5 m deeper than Hole U1319A to ensure all MWD/LWD sensors recorded measurements to the total depth of Hole U1319A.

Logging data quality

Figure F39 shows the quality control logs for the Hole U1319B LWD data. The target ROP of 30 m/h (±5 m/h) was generally achieved except above 10 mbsf, where a rapid jet-in was necessary to start the hole. This ROP was sufficient to record 1 sample/4 cm over the majority of the hole. The quality of GVR images is good, and no significant resolution loss is observed with variation in ROP except from 0 to 11 mbsf where the images are degraded by the rapid ROP and low rotation rate of the bit. Time-after-bit (TAB) measurements are ~5 min for ring resistivity, 4 min for gamma ray logs, 43 min for density, and 46 min for neutron porosity logs.

The density caliper log (DCAV), which gives the diameter of the LWD borehole, is the best indicator of borehole conditions. The density caliper values range between 42.2 cm at the top of Hole U1319B where sediments are unconsolidated to ~25.4 cm toward the bottom of the hole where the sediments are more compacted. Only the uppermost 50 m of the hole has washouts >2.5 cm. A standoff of <2.5 cm between the tool and the borehole wall indicates high-quality density measurements with an accuracy of ±0.015 g/cm³. The bulk density correction (IDDR), calculated from the difference between the short- and long-spaced density measurements, varies from –0.05 to 0.16 g/cm³ (mean = 0.06 g/cm³) (Fig. F39), which shows that the bulk density measurements are of good quality.

The depths, in mbsf, for the LWD logs were fixed by identifying the gamma ray signal at the seafloor. For

Hole U1319B, it was determined that the gamma ray log pick for the seafloor was at a depth of 1441.0 mbrf. The rig floor logging datum was 10.4 m above sea level for this hole.

Annular pressure while drilling and equivalent circulating density

Annular pressure is measured within the borehole (APWD) but is monitored, as annular pressure while drilling in excess of hydrostatic (APWD*) and equivalent circulating density referenced to the seafloor (ECD_{rsf}) (see discussion in **"Array resistivity compensated tool"** in "Downhole measurements" in the "Methods" chapter). There were no abrupt pressure increases during operations in Hole U1319B (Fig. **F40**). APWD increased linearly with depth from the seafloor to 160 mbsf. APWD* was <0.25 MPa for the majority of the borehole. ECD_{rsf} decreased rapidly in the shallow section and then decreased slowly from 60 to 160 mbsf. Two pressure increases were measured below 160 mbsf, caused by mud sweeps that were part of drilling operations.

Interpretation

MWD operations in Hole U1319B provided data coverage by all LWD tools to at least 157.5 mbsf (Fig. **F41**). Hole quality was excellent below 50 mbsf, where the diameter was <28 cm. The gamma ray log (GR) gradually increases with depth in the first 50 mbsf where hole diameter is large; below this depth GR is nearly constant (~75 gAPI). Deep button resistivity increases from 0.6 to 1.8 Ωm from the seafloor to 175 mbsf. Over this same depth interval, bulk density increases from 1.4 to 2.0 g/cm^3 and porosity decreases from 75% to 50%. These trends represent normal compaction where pore volume and water content are decreasing with depth because vertical effective stress is increasing.

Deviations from this normal compaction trend exist at 25 mbsf where GR has a step decrease, from 30.5 to 31.5 mbsf where GR increases, and from 78 to 93 mbsf where bulk density decreases. The GR decrease at 25 mbsf correlates with the transition to foraminifer-bearing clay at the top of lithostratigraphic Unit III (see **"Lithostratigraphy"**), GR increases from 30.5 to 31.5 mbsf and correlates with fine laminae of sands identified in lithostratigraphic Unit IV (see **"Lithostratigraphy"**). The decrease in bulk density (78–93 mbsf) is consistent with decreases in gamma ray attenuation (GRA)- and moisture and density (MAD)-derived density measurements on core (see **"Physical properties"**). Overall, the resistivity and GR responses indicate that the sedimentary section on the edge of Brazos-Trinity Basin IV is condensed and minimally influenced by turbidite influx to the basin.

The PEF log from Hole U1319B gradually increases from 0 to 126 mbsf. Between 126 and 145 mbsf, PEF decreases slightly. We interpret these subtle variations as a change in silt/clay content. PEF anomalies are found at 148–149 and 153–155 mbsf, where values increase from a mean value of 3.4 b/e$^-$ to 7.0 and 9.6 b/e$^-$, respectively. These anomalies do not correlate with any other physical measurement obtained with LWD tools and are likely caused by barite in the mud cake generated after 150 bbl of 12 ppg mud was displaced at the bottom of the hole. These mud sweeps are also imaged in the APWD log (Fig. **F40**).

GVR resistivity images show some steeply dipping features between 172 and 174 mbsf within mass transport deposits (Fig. **F42**). These images also show a potential erosional surface at 167 mbsf and several alternating resistive and conductive bands that could reflect laminations observed within the cores (Fig. **F42**).

We used LWD density data to construct a synthetic seismogram for Hole U1319B (Fig. **F43**). Reflection coefficients were calculated using the LWD density data and a constant compressional wave velocity of 1600 m/s. A 200 Hz minimum-phase Ricker wavelet was convolved with the reflection coefficient series to create the synthetic seismogram. The correlation of events between the synthetic seismogram and the high-resolution seismic data indicates that the time-depth model is appropriate for these sediments in the shallow section (e.g., seismic Reflectors R10–R40). A time-depth mismatch occurs at seismic Reflectors R50 and R60, where the synthetic reflections occur shallower than the same events in the high-resolution seismic data (Fig. **F43**). The overall quality of the time-depth model allows correlation of seismic reflections with observations in core and log data.

Six regional reflections (seafloor [SF] and seismic Reflectors R10, R30, R40, R50, and R60) mapped on high-resolution seismic data have been correlated with logging data in Hole U1319A. The sediments between seismic Reflectors R30 and R40 have a constant bulk density. Bulk density has a small, abrupt increase, and the GR also shows an increase at seismic Reflector R40. Seismic Reflector R50 correlates with subtle decreases in GR, resistivity, and bulk density. A minor increase in bulk density may be associated with the low amplitude of seismic Reflector R60; however, the time-depth tie at Reflector R60 is not well constrained. In general, the logging data indicate a relatively homogeneous mud-prone section that is normally compacted.

Temperature and pressure measurements

Advanced piston corer temperature tool

The advanced piston corer temperature (APCT) tool was deployed before collecting Core 308-U1319A-5H (42.5 mbsf) (Table T14). Temperature was measured in the sediment for 10 min to establish the temperature decay curve (Fig. F44). Extrapolation of the temperature decay curve with an assumed thermal conductivity of 1.24 W/(m·K) provides an equilibrium temperature of 5.86°C (Fig. F44). Data from the deployment are available in "Downhole" in "Supplementary material."

Temperature/dual pressure probe

Two deployments of the temperature/dual pressure probe (T2P) were completed in Hole U1319A (Table T14). The first deployment, completed in the water column, was the first sea deployment of the T2P. The deployment was intended as a pressure test for the instrument. The second deployment penetrated the sediment at 80.5 mbsf immediately beneath Core 308-U1319A-9H.

T2P Deployment 1

The T2P was deployed prior to Core 308-U1319A-1H to a depth of 1388 meters below sea level (mbsl). The drill bit was positioned at 1380 mbsl and the T2P was deployed while preparing the seafloor camera survey. The primary objectives of the deployment were to (1) pressure test the T2P, (2) check pressure transducer calibrations, and (3) confirm that the T2P could successfully pass through the lockable float valve (LFV) of the bottom-hole assembly (BHA). Data were continuously recorded in memory on the tool at 1 Hz sampling rate.

T2P Deployment 1 occurred in the drill pipe with the T2P connected to the colleted delivery system (CDS). The deployment methodology is provided in "Temperature/dual pressure probe" in "Downhole measurements" in the "Methods" chapter. The T2P was lowered until the tip was at 511 mbsl, where a hydrostatic reference was recorded for 2 min. The tool was then lowered until the tip was at 1011 mbsl for another 2 min reference measurement. The T2P was then lowered through the LFV. The T2P tip reached a maximum depth of 1388 mbsl (–41.6 mbsf), where a 5 min reference was recorded. References were also taken during retrieval of the T2P when the tip was at 1010 and 511 mbsl. No drilling fluid was circulated during the deployment. Table T15 provides the time-event log for T2P Deployment 1.

The pressure test deployment was successful. The tool recorded pressure and temperature for the entire deployment (Fig. F45) and passed through the LFV without problem. The tip pressures were consistent with hydrostatic pressure assuming an average fluid density of 1.024 g/cm^3 (Fig. F45). The shaft pressures were higher. The offset in pressure at the shaft is interpreted to reflect an errant calibration factor. The temperature record showed a downhole decrease in temperature to 4.82°C at 1388 mbsl. Comparison of the pressures and temperatures during deployment and recovery documented <2% drift during the experiment. Measurements during retrieval drifted upward for fluid pressure and downward for temperature.

T2P Deployment 2

The second T2P deployment occurred after Core 308-U1319A-9H; therefore, the T2P measured pressure and temperature at 80.5 mbsf in sediment recovered in Core 308-U1319A-10H. The deployment occurred with the drill bit initially raised to 68.5 mbsf. Once the T2P was latched in the CDS, the drill string pushed the T2P into the formation (deployment procedure is described in "Temperature/dual pressure probe" in "Downhole measurements" in the "Methods" chapter). Formation pressure and temperature were monitored for 30 min before retrieving the T2P (Fig. F46). Overpull of 7000 lb was measured when pulling the T2P out of the hole. This overpull was interpreted to be the force required to unseat the CDS from the BHA, not the force required to pull the T2P out of the formation. Drilling fluid was circulated during the deployment; however, circulation was stopped when taking hydrostatic reference measurements, when pushing the probe into the sediment, and for the first 10 min that the T2P was in the sediment. Table T16 provides a timeline for the deployment.

When the T2P was recovered on the rig floor, the protective shroud was not covering the tip. We interpret that the shroud never reseated over the tip during retrieval of the tool. The tip of the tool was damaged (Fig. F47). Damage was interpreted to result from bending of the tip during penetration followed by a straightening of the tip when the T2P was pulled into the BHA. Secondary inspection of the tool revealed that the drive tube was bent slightly.

Pressure and temperature data were recorded throughout the deployment, despite the damage to the tip. The pressure and temperature increased before the drill string pushed the T2P into the formation (Fig. F46; Table T16). This response reflects the tip of the tool entering the formation while engaging the CDS in the BHA; it indicates that the weight of the tool is sufficient to cause penetration in the formation. The shaft pressure and temperature increased after the drill string pushed the T2P into the

sediment. The tip pressure decreased during penetration.

After 30 min in the sediment, the pressure at the tip was 15.95 MPa, whereas the shaft pressure was 15.5 MPa. Hydrostatic pressure at 80.5 mbsf was 15.2 MPa. The equilibrium temperature was 7.3°C (Fig. F46). These preliminary pressure and temperature interpretations should be viewed cautiously because of the damage incurred during the deployment.

Most likely, the T2P and drive tube were damaged because the T2P did not enter the sediment vertically. One possible reason the shaft was not vertical when it penetrated is the 12 m distance between the drill bit and the bottom of the hole. Future deployments were modified with the drill bit <2 m off the bottom of the hole. The goal is to achieve vertical penetration of the probe and thus preserve the integrity of the T2P and the recorded data.

References

Anderson, R.N., and Fillon, R.H. (Ed.), 2004. Late Quaternary Stratigraphic Evolution of the Northern Gulf of Mexico Margin. *Spec. Publ.—SEPM (Soc. Sediment. Geol.),* 79.

Badalini, G., Kneller, B., and Winker, C.D., 2000. Architecture and processes in the late Pleistocene Brazos-Trinity turbidite system, Gulf of Mexico continental slope. *Deep-Water Reservoirs of the World: Proc. GCSSEPM 20th Annu. Res. Conf.,* 16–34.

Baker, P.A., and Burns, S.J., 1985. The occurrence and formation of dolomite in organic-rich continental margin sediments. *AAPG Bull.,* 69:1917–1930.

Bassinot, F.C., Labeyrie, L.D., Vincent, E., Quidelleur, X., Shackleton, N.J., and Lancelot, Y., 1994. The astronomical theory of climate and the age of the Brunhes-Matuyama magnetic reversal. *Earth Planet. Sci. Lett.,* 126:91–108. **doi:10.1016/0012-821X(94)90244-5**

Beaubouef, R.T., Abreu, V., and Van Wagoner, J.C., 2003. Basin 4 of the Brazos-Trinity slope system, western Gulf of Mexico: the terminal portion of a late Pleistocene lowstand system tract. *In* Roberts, H.H., Rosen, N.C., Fillon, R.H., and Anderson, J.B. (Eds.), *Shelf Margin Deltas and Linked Downslope Petroleum Systems: Global Significance and Future Exploration Potential:* Proc. 23 Ann. Res. Conf., GCSSEPM Found., 45–66.

Beaubouef, R.T., and Friedmann, S.J., 2000. High resolution seismic/sequence stratigraphic framework for the evolution of Pleistocene intra slope basins, western Gulf of Mexico: depositional models and reservoir analogs. *Deep-Water Reservoirs of the World: Proc. GCSSEPM 20th Annu. Res. Conf.,* 40–60.

Beaubouef, R.T., and Pirmez, C., 1999. Mixed sand/mud submarine fan systems: comparing the Amazon Fan to intraslope basin fans of the Gulf of Mexico. *AAPG Annu. Mtg., Expanded Abstr.,* A10.

Berggren, W.A., Hilgen, F.J., Langereis, C.G., Kent, D.V., Obradovich, J.D., Raffi, I., Raymo, M.E., and Shackleton, N.J., 1995. Late Neogene chronology: new perspectives in high-resolution stratigraphy. *Geol. Soc. Am. Bull.,* 107:1272–1287. **doi:10.1130/0016-7606(1995)107<1272:LNCNPI>2.3.CO;2**

Bouloubassi, I., Rullkötter, J., and Meyers, P.A., 1999. Origin and transformation of organic matter in Pliocene-Pleistocene Mediterranean sapropels: organic geochemical evidence. *Mar. Geol.,* 153:177–197. **doi:10.1016/S0025-3227(98)00082-6**

Cisowski, S.M., and Hall, F.R., 1997. An examination of the paleointensity record and geomagnetic excursions recorded in Leg 155 cores. *In* Flood, R.D., Piper, D.J.W., Klaus, A., and Peterson, L.C. (Eds.), *Proc. ODP, Sci. Results,* 155: College Station, TX (Ocean Drilling Program), 231–243. [**PDF**]

Culver, S.J., and Buzas, M.A., 1983. Recent benthic foraminiferal provinces in the Gulf of Mexico. *J. Foraminiferal Res.,* 13:21–31.

D'Hondt, S.L., Jørgensen, B.B., Miller, D.J., et al., 2003. *Proc. ODP, Init. Repts.,* 201 [CD-ROM]. Available from: Ocean Drilling Program, Texas A&M University, College Station TX 77845-9547, USA. [**HTML**]

Drexler, J.W., Rose, W.I., Jr., Sparks, R.S.J., and Ledbetter, M.T., 1980. The Los Chocoyos ash, Guatemala: a major stratigraphic marker in middle America and three ocean basins. *Quat. Res.,* 13:327–345. **doi:10.1016/0033-5894(80)90061-7**

Ericson, D.B., and Wollin, G., 1968. Pleistocene climates and chronology in deep-sea sediments. *Science,* 162:1227–1234.

Flood, R.D., Piper, D.J.W., Klaus, A., et al., 1995. *Proc. ODP, Init. Repts.,* 155: College Station, TX (Ocean Drilling Program).

Fraticelli, C.M., 2003. Linking climate, sea level, and sedimentary response on the Texas shelf and upper slope: examples from the Brazos and Colorado fluvial-deltaic system [Ph.D. dissert.]. Rice Univ., Houston, TX.

Freed, W.K., and Healy, N., 1974. Excursions of the Pleistocene geomagnetic field recorded in Gulf of Mexico sediments. *Earth Planet. Sci. Lett.,* 24:99–104. **doi:10.1016/0012-821X(74)90013-2**

Friedmann, S.J., and Beaubouef, R.T., 1999. Relationships between depositional processes, stratigraphy and salt tectonics in a closed intraslope basin: E breaks area, Gulf of Mexico. *AAPG Annu. Mtg., Extended Abstr.,* A43.

Gieskes, J.M., 1983. The chemistry of interstitial waters of deep-sea sediments: interpretation of deep-sea drilling data. *In* Riley, J.P., and Chester, R. (Eds.), *Chemical Oceanography* (Vol. 8): London (Academic), 221–269.

Hine, N., and Weaver, P.P.E., 1998. Quaternary. *In* Bown P.R. (Ed), *Calcareous Nannofossil Biostratigraphy:* Dordrecht (Kluwer Academic Publishers), 266–283.

Kennett, J.P., and Huddlestun, P., 1972. Late Pleistocene paleoclimatology, foraminiferal biostratigraphy, and tephrochronology, western Gulf of Mexico. *Quat. Res.,* 2:38–69. **doi:10.1016/0033-5894(72)90004-X**

Kohl, B., 1985. Late Quaternary planktonic foraminifers from the Pigmy Basin, Gulf of Mexico, Site 619, Deep Sea Drilling Project Leg 96. *In* Bouma, A.H., Coleman, J.M., Meyer, A.W., et al., *Init. Repts. DSDP*, 96: Washington (U.S. Govt. Printing Office), 657–670.

Mallarino, G., Droxler, A.W., Beaubouef, R.T., Abreu, V., and Laberye, L., in press. Sea level influence on the nature and timing of a mini-basin sedimentary fill (northwestern slope of the Gulf of Mexico). *AAPG Bull.*

Martin, R.E., Johnson, G.W., Neff, E.D., and Krantz, D.W., 1990. Quaternary planktonic foraminiferal assemblage zones of the northeast Gulf of Mexico, Columbia basin (Caribbean Sea), and tropical Atlantic Ocean: graphic correlation of microfossil and oxygen isotope datums. *Paleoceanography,* 5:531–555.

Moore, G.F., Taira, A., Klaus, A., et al., 2001. *Proc. ODP, Init. Repts.,* 190 [CD-ROM]. Available from: Ocean Drilling Program, Texas A&M University, College Station TX 77845-9547, USA. [**HTML**]

Morton, R.A., and Suter, R.J., 1996. Sequence stratigraphy and composition of late Quaternary shelf-margin deltas, northern Gulf of Mexico. *AAPG Bull.,* 80:505–530.

Newberry, C.J., Webster, G., Cragg, B.A., Parkes, R.J., Weightman, A.J., and Fry, J.C., 2004. Diversity of prokaryotes and methanogenesis in deep subsurface sediments from the Nankai trough, Ocean Drilling Program Leg 190. *Environ. Microbiol.,* 6:274–287. **doi:10.1111/j.1462-2920.2004.00568.x**

Parkes, R.J., Cragg, B.A., Bale, S.J., Getliff, J.M., Goodman, K., Rochelle, P.A., Fry, J.C., Weightman, A.J., and Harvey, S.M., 1994. Deep bacterial biosphere in Pacific Ocean sediments. *Nature (London, U. K.),* 371:410–413. **doi:10.1038/371410a0**

Phleger, F.B., and Parker, F.L., 1951a. Ecology of foraminifera, Northwest Gulf of Mexico, Part I. Foraminiferal distribution. *Mem.—Geol. Soc. Am.,* 46:1–88.

Phleger, F.B., and Parker, F.L., 1951b. Ecology of foraminifera, Northwest Gulf of Mexico, Part II. Foraminifera species. *Mem.—Geol. Soc. Am.,* 46:1–64.

Poag, C.W., 1981. *Ecologic Atlas of Benthic Foraminifera of the Gulf of Mexico:* Stroudsburg, PA (Hutchinson Ross).

Satterfield, W.M., and Behrens, E.W., 1990. A late Quaternary canyon channel system, northwest Gulf of Mexico continental slope. *Mar. Geol.,* 92:51–67. **doi:10.1016/0025-3227(90)90026-G**

Shipboard Scientific Party, 1996. Sites 980/981. *In* Jansen, E., Raymo, M.E., Blum, P., et al., *Proc. ODP, Init. Repts.,* 162: College Station, TX (Ocean Drilling Program), 49–90.

Stupavsky, M., and Gravenor, C.P., 1984. Paleomagnetic dating of Quaternary sediments: a review. *In* Mahaney, W.C. (Ed.), *Quaternary Dating Methods:* Amsterdam (Elsevier), 123–140.

van Morkhoven, F.P.C.M., Berggren, W.A., and Edwards, A.S., 1986. *Cenozoic Cosmopolitan Deep-Water Benthic Foraminifera*. Bull. Cent. Rech. Explor.—Prod. Elf-Aquitaine, Mem. 11.

Winker, C.D., 1996. High-resolution seismic stratigraphy of a late Pleistocene submarine fan ponded by salt-withdrawal minibasins on the Gulf of Mexico continental slope. *Proc. 3rd Annu. Offshore Technol. Conf.,* 28(1):619–628.

Winker, C.D., and Booth, J.R., 2000. Sedimentary dynamics of the salt-dominated continental slope, Gulf of Mexico: integration of observations from the seafloor, near-surface, and deep subsurface. *Deep-Water Reservoirs of the World: Proc. GCSSEPM 20th Annu. Res. Conf.,* 1059–1086.

Publication: 8 July 2006
MS 308-103

Figure F1. Bathymetric map of the Gulf of Mexico and the two drilling areas (Brazos-Trinity and Ursa) in this study.

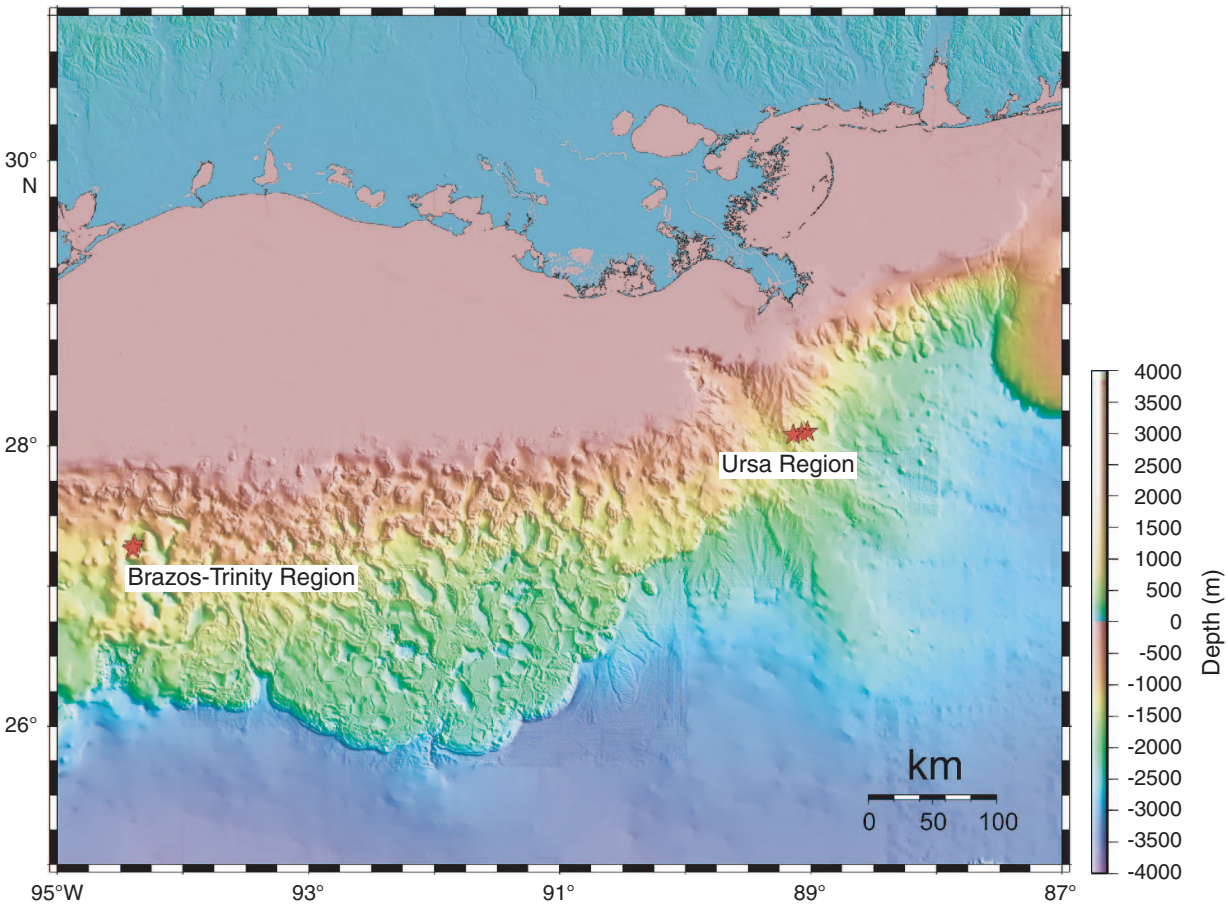

Figure F2. Physiography and latest Pleistocene paleogeographic features offshore Texas (simplified from Winker, 1996, and Badalini et al., 2000).

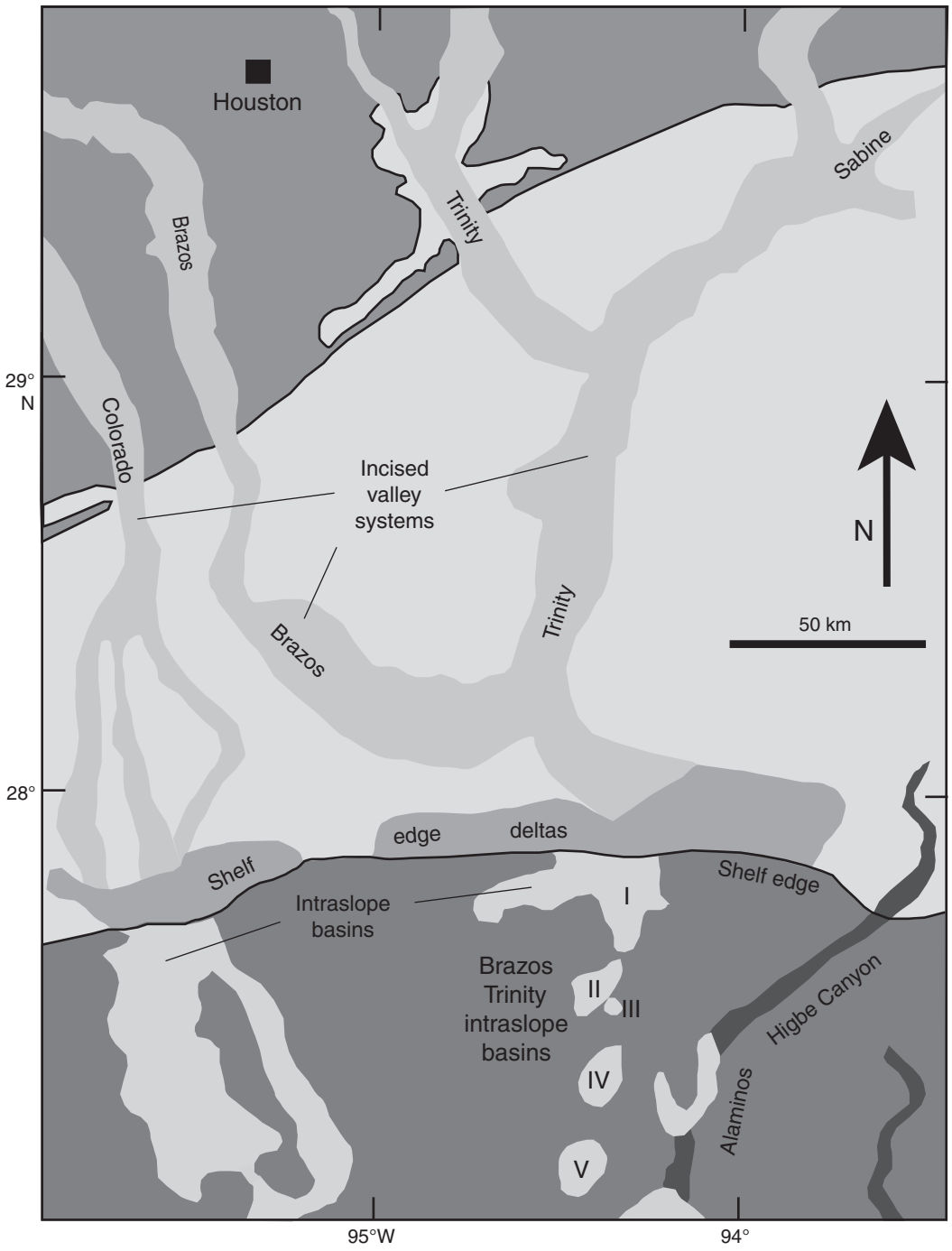

Figure F3. Relationship between seismic surfaces (seafloor [SF] and R10–R60) and published interpretations. Mallarino = Mallarino et al. (in press), Badalini = Badalini et al. (2000), Beaubouef = Beaubouef and Friedman (2000).

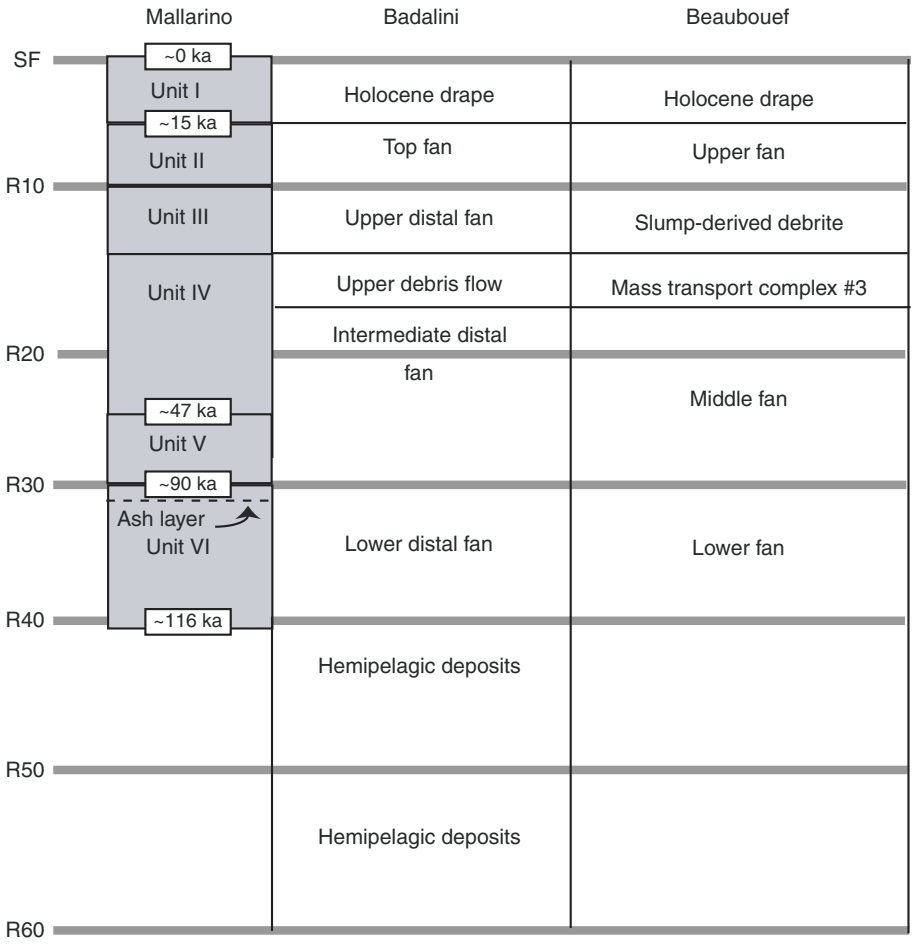

Figure F4. Bathymetric chart of Brazos-Trinity Basin IV, showing locations of dip seismic Line 3020 and the three sites drilled in Brazos-Trinity Basin IV during Expedition 308. Depth contours at 10 m intervals; artificial sun illumination from the northwest (bathymetric information adapted from report number 3060-TAMU-GOM).

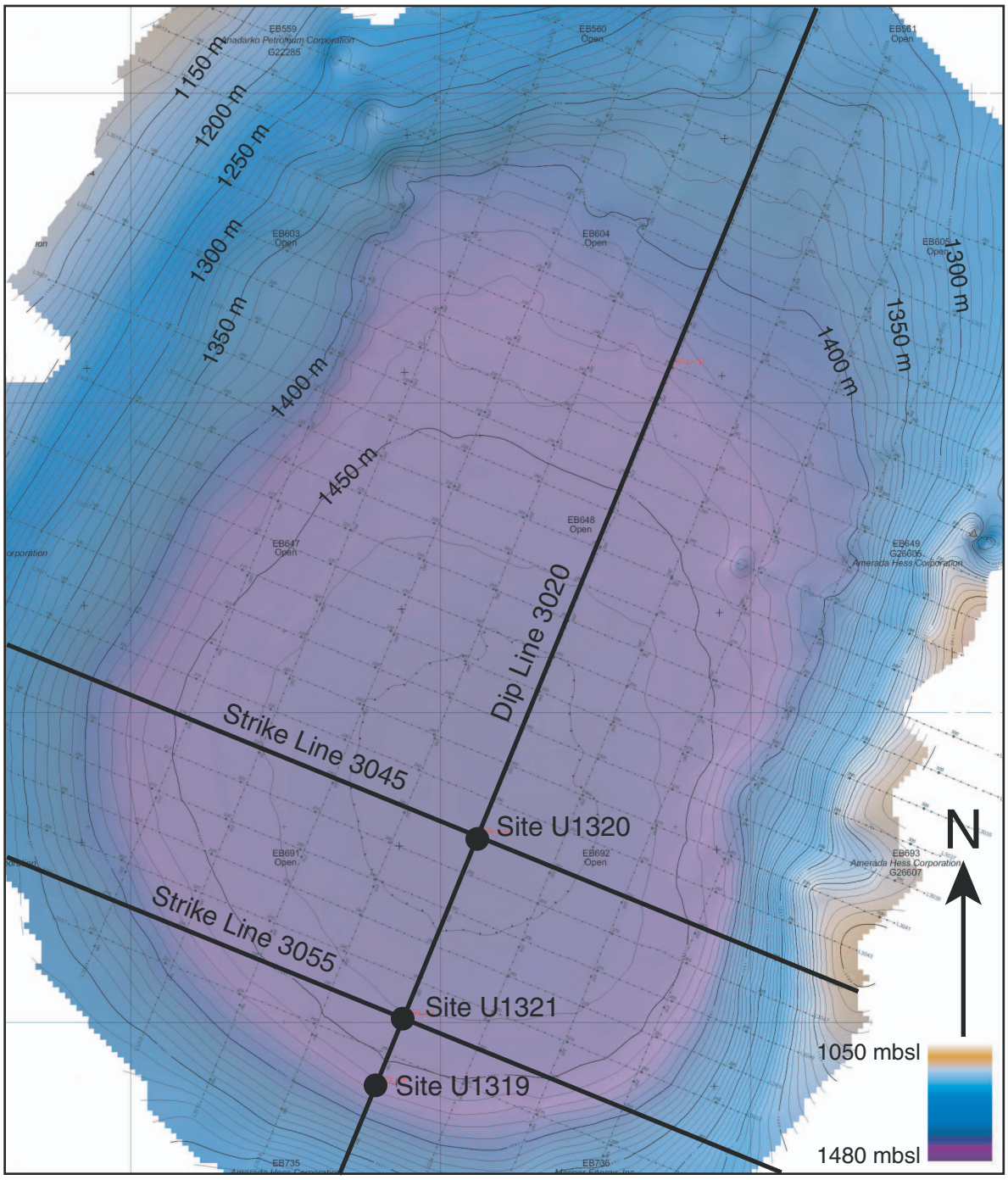

Figure F5. Dip seismic Section 3020 showing the location of Sites U1319, U1320, and U1321. Seismic line is located in Figure F4.

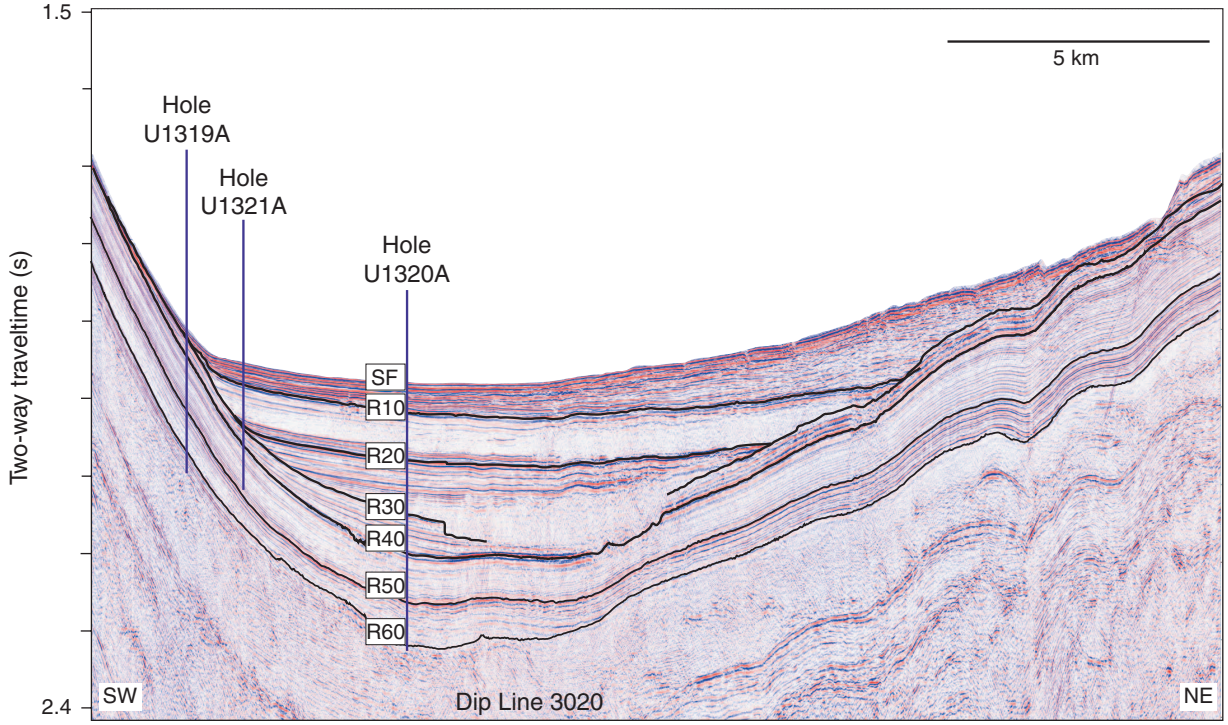

Figure F6. Strike seismic Section 3045 showing the location of Site U1320. Seismic line is located in Figure F4.

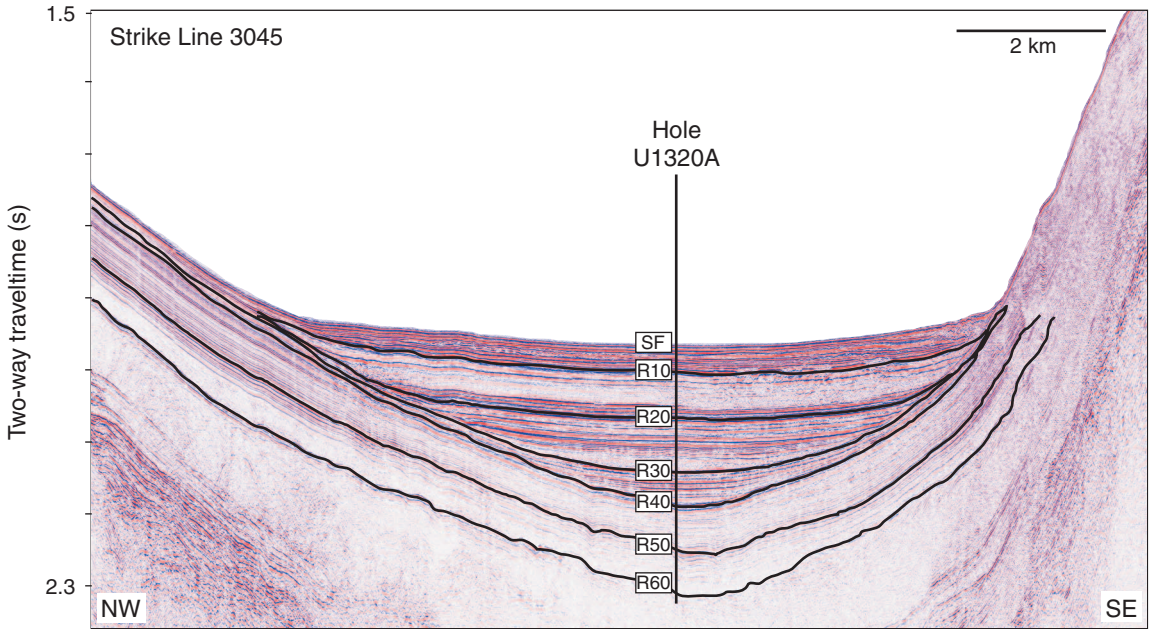

Figure F7. Strike seismic Section 3055 showing the location of Site U1321. Seismic line is located in Figure F4.

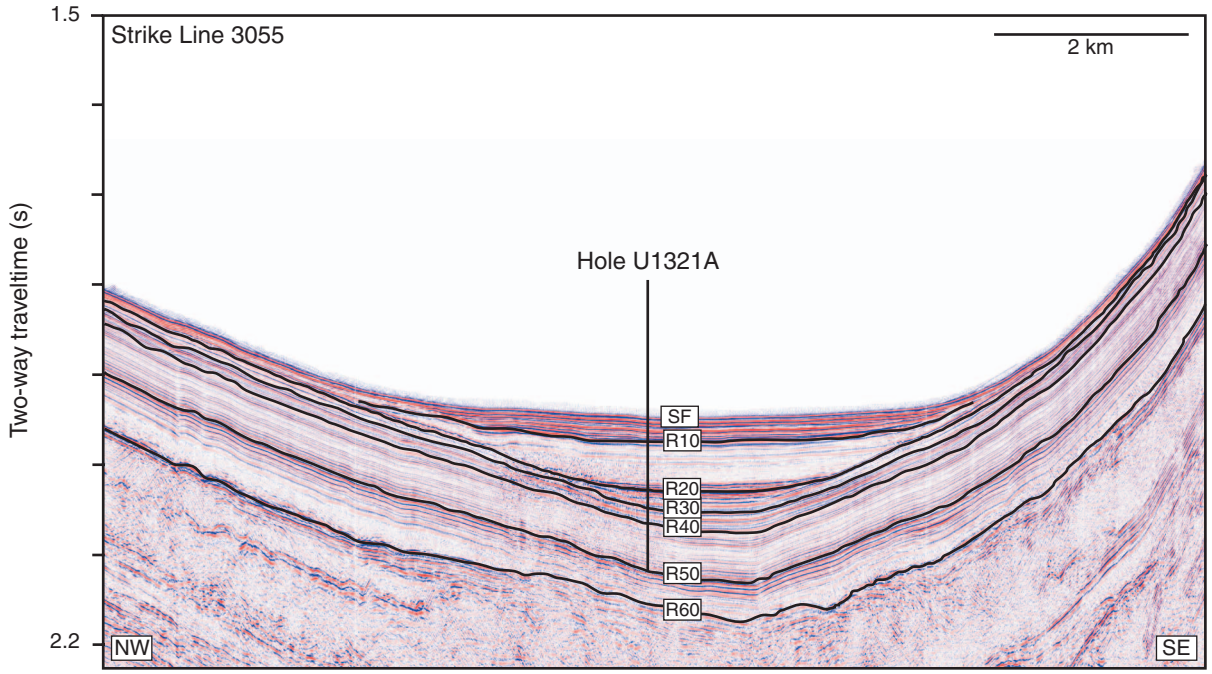

Figure F8. Seismic reflection profile over Site U1319 from dip seismic Line 3020.

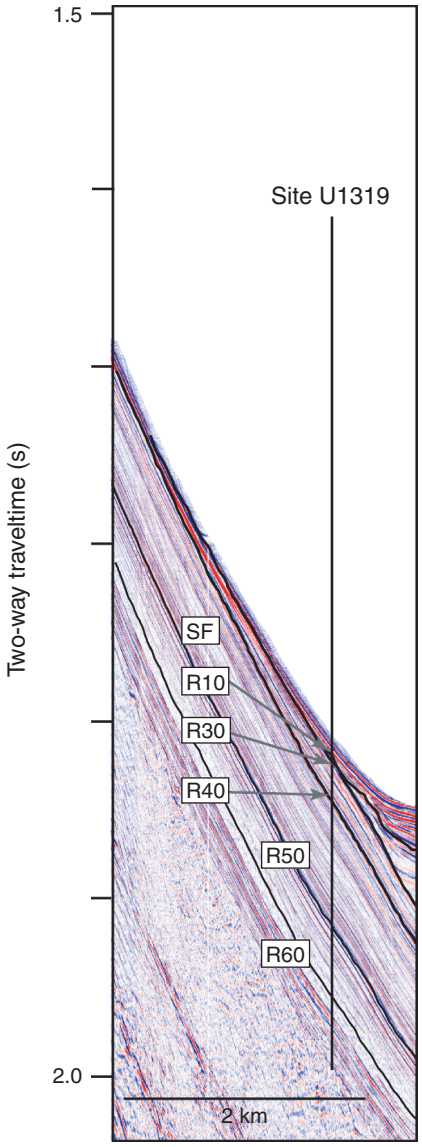

Figure F9. Lithostratigraphic summary. Core recovery, seismic reflectors mapped through Basin-Trinity Basin IV, lithology, and lithostratigraphic description by unit.

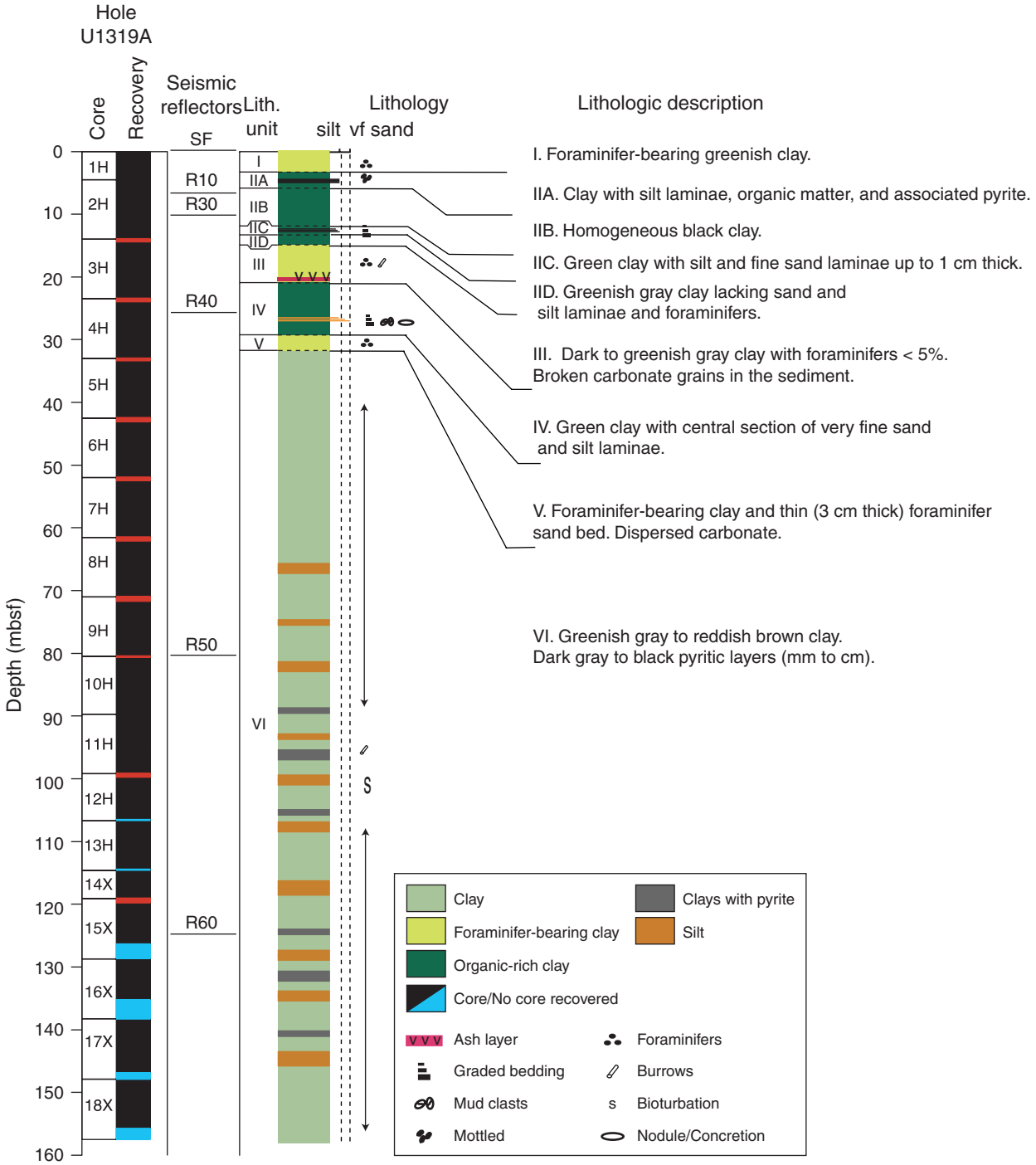

Figure F10. Spectrophotometric lightness values for the upper 60 m of Hole U1319A. Note how the foraminifer-rich hemipelagic Units I, III, and V show relatively high reflectance.

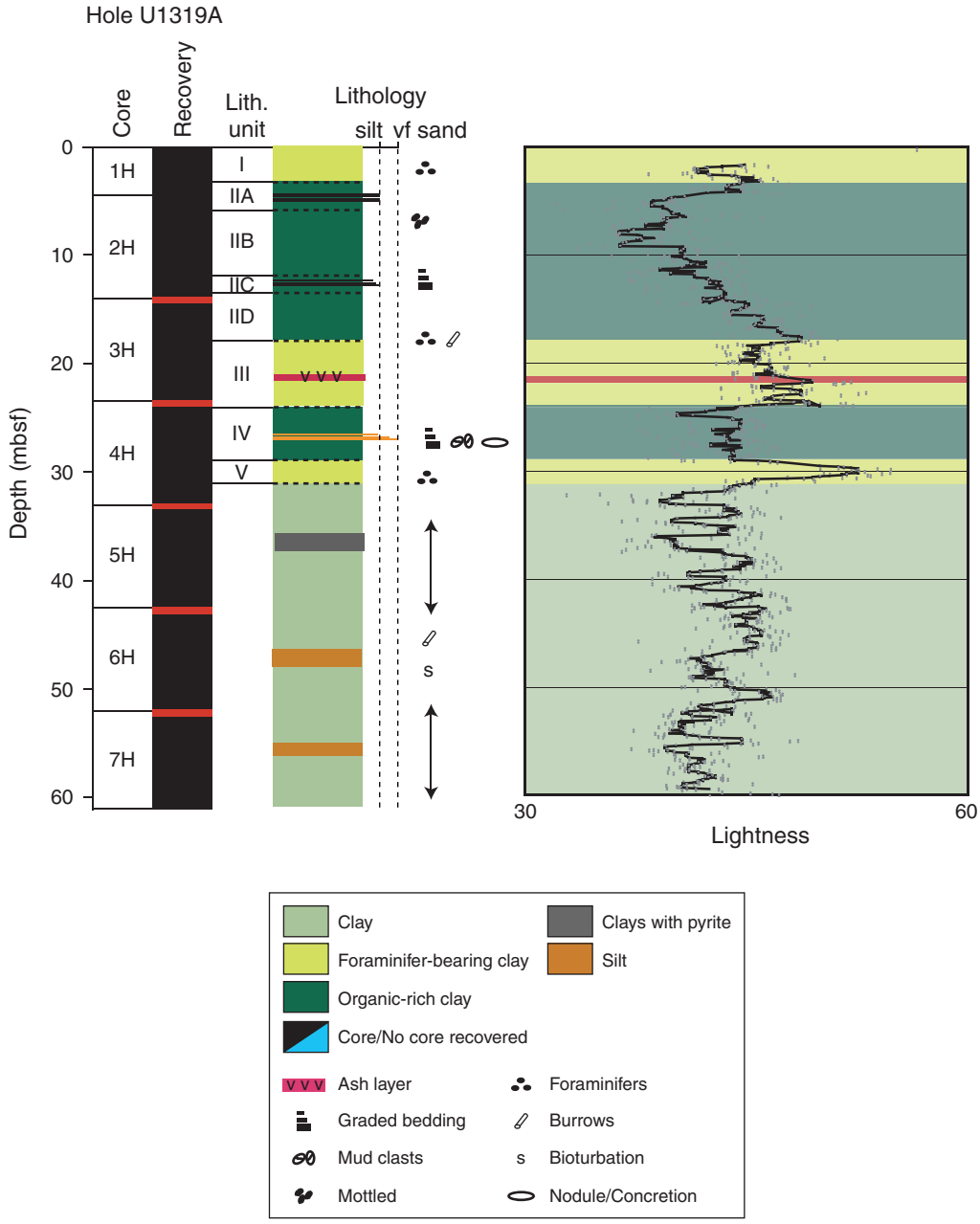

Figure F11. Black clay near the top of Subunit IIB (interval 308-U1319A-2H-2, 35–55 cm). This unit is mostly homogeneous except at the upper and lower transition zones.

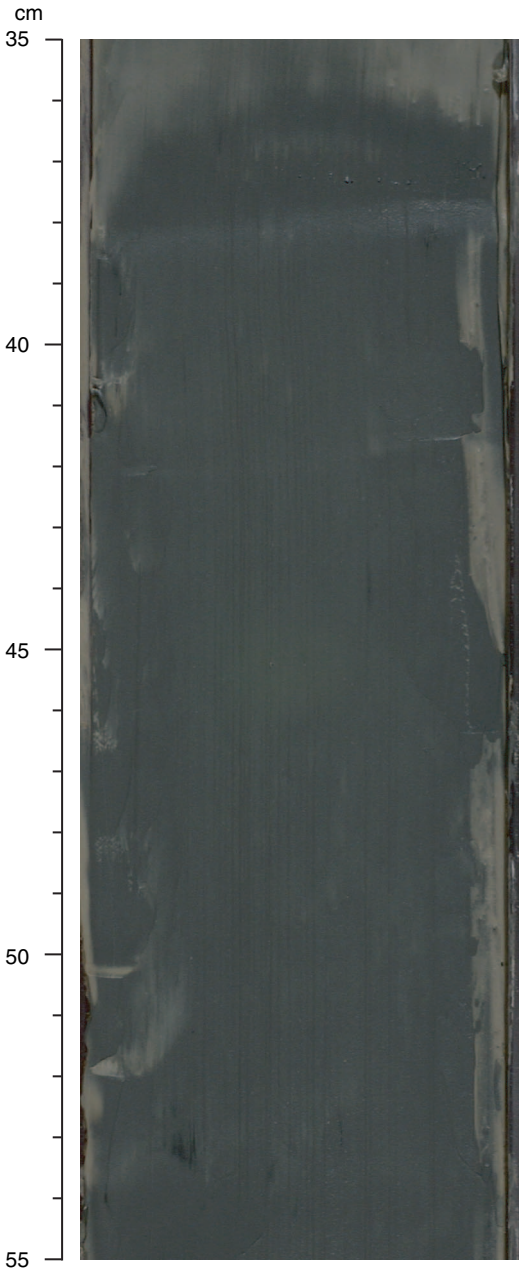

Figure F12. Fine to very fine, graded sand laminae characteristic of turbidite deposition in Subunit IIC (interval 308-U1319A-2H-6, 118–128 cm).

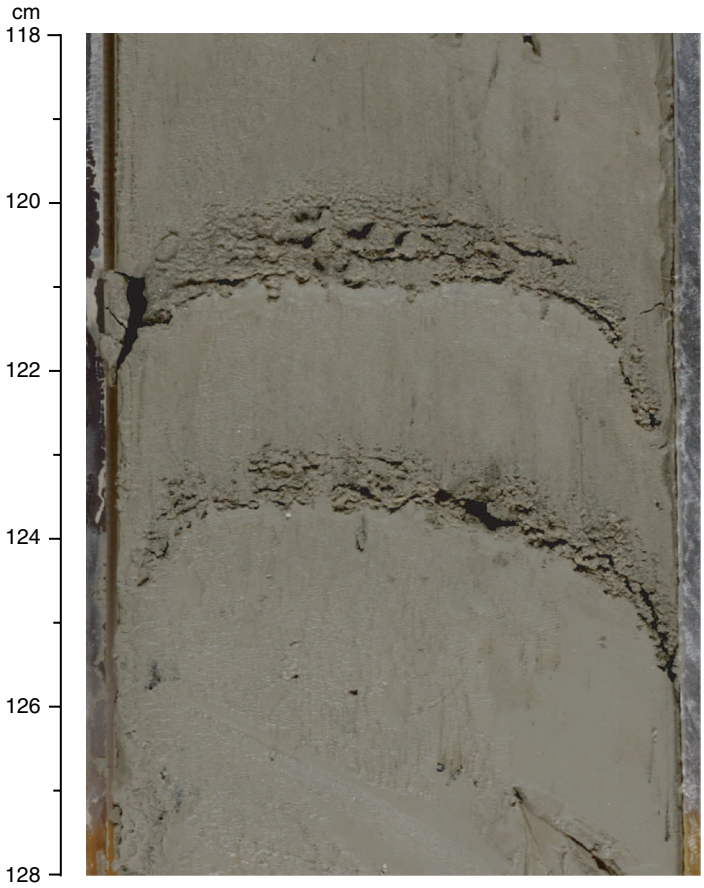

Figure F13. Ash bed (118–121 cm) and background hemipelagic sedimentation in Unit III (interval 308-U1319A-3H-6, 113–128 cm). Note the relatively light color of the sediment and the evidence for bioturbation.

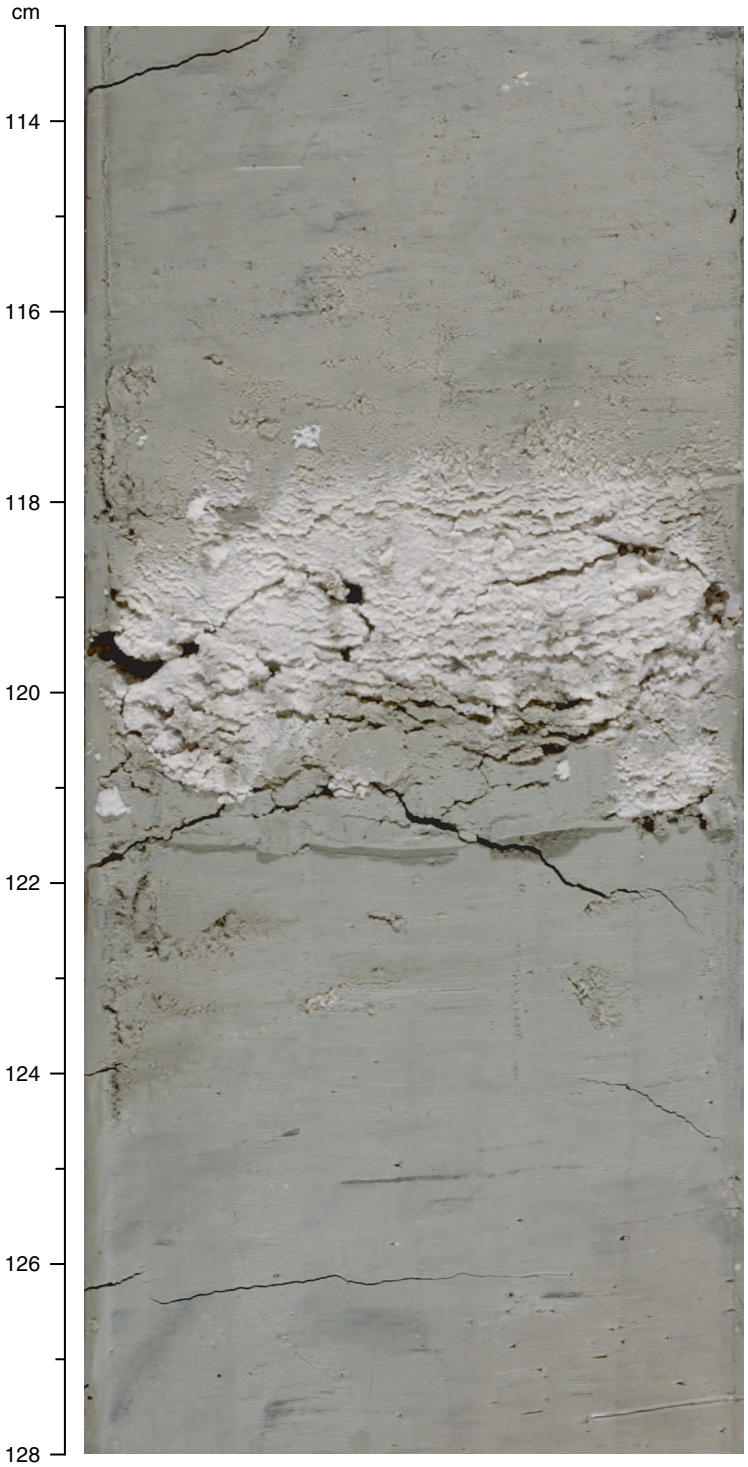

Figure F14. Photomicrograph of ash in Unit III at 22.7 mbsf (Sample 308-U1319A-3H-6, 117 cm).

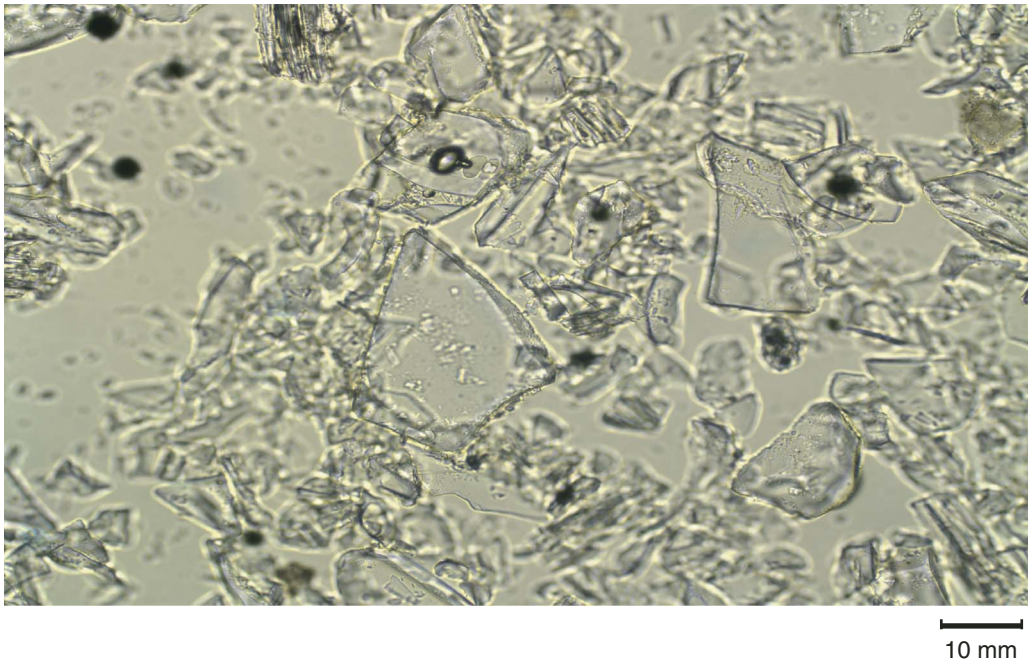

Figure F15. Types of layering in Unit VI. **A.** Greenish gray and reddish brown layers, typically tens of centimeters thick and variously bioturbated (interval 308-U1319A-4H-6, 50–68 cm). **B.** Thin centimeter-scale layering in greenish gray clays, not appreciably disrupted by bioturbation (interval 308-U1319A-5H-2, 48–70 cm). **C.** Bioturbated black organic- and pyritic-rich layers (interval 308-U1319A-7H-3, 107–125 cm).

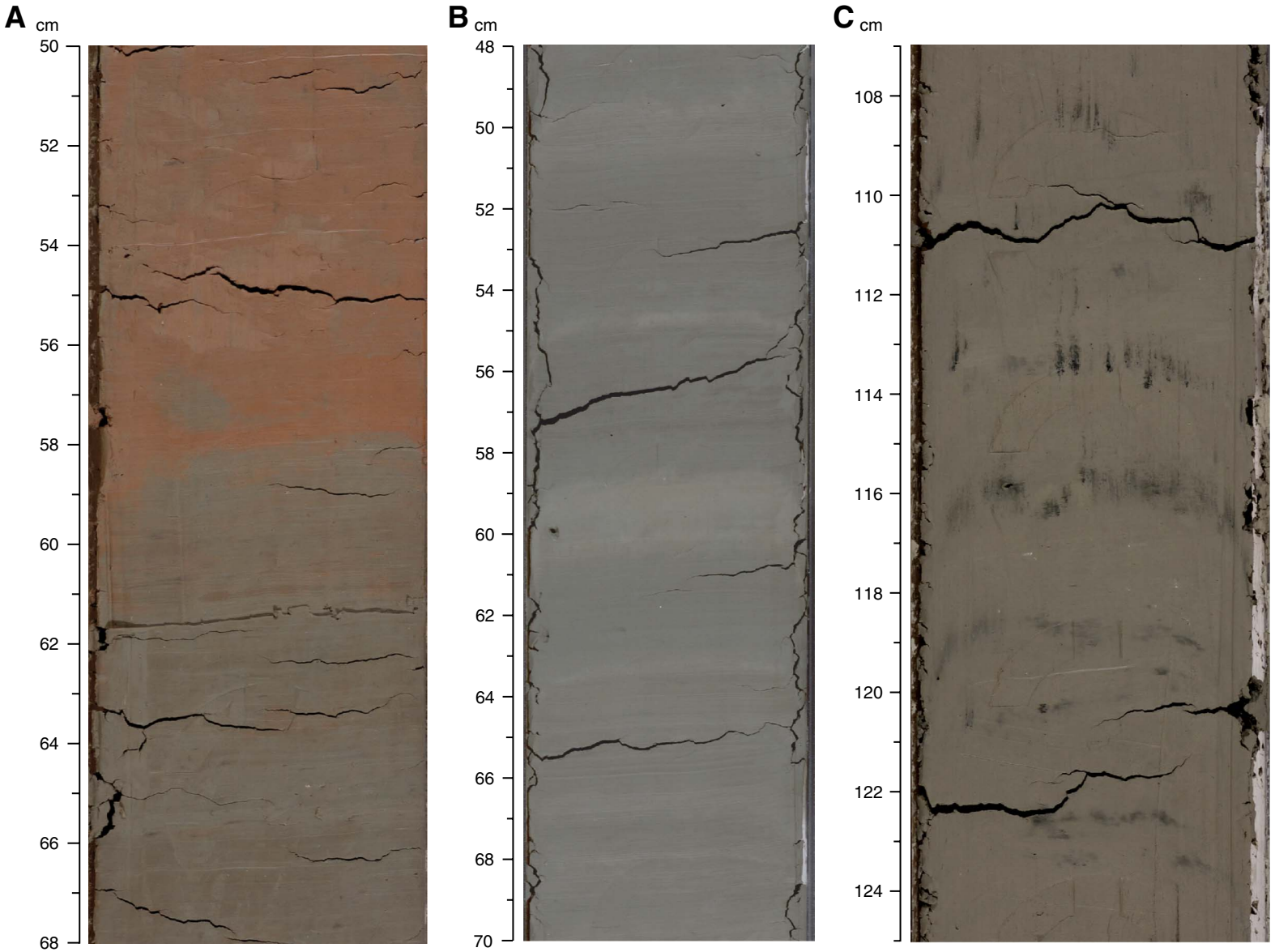

Figure F16. Graphic summary of smear slide analyses in Hole U1319A.

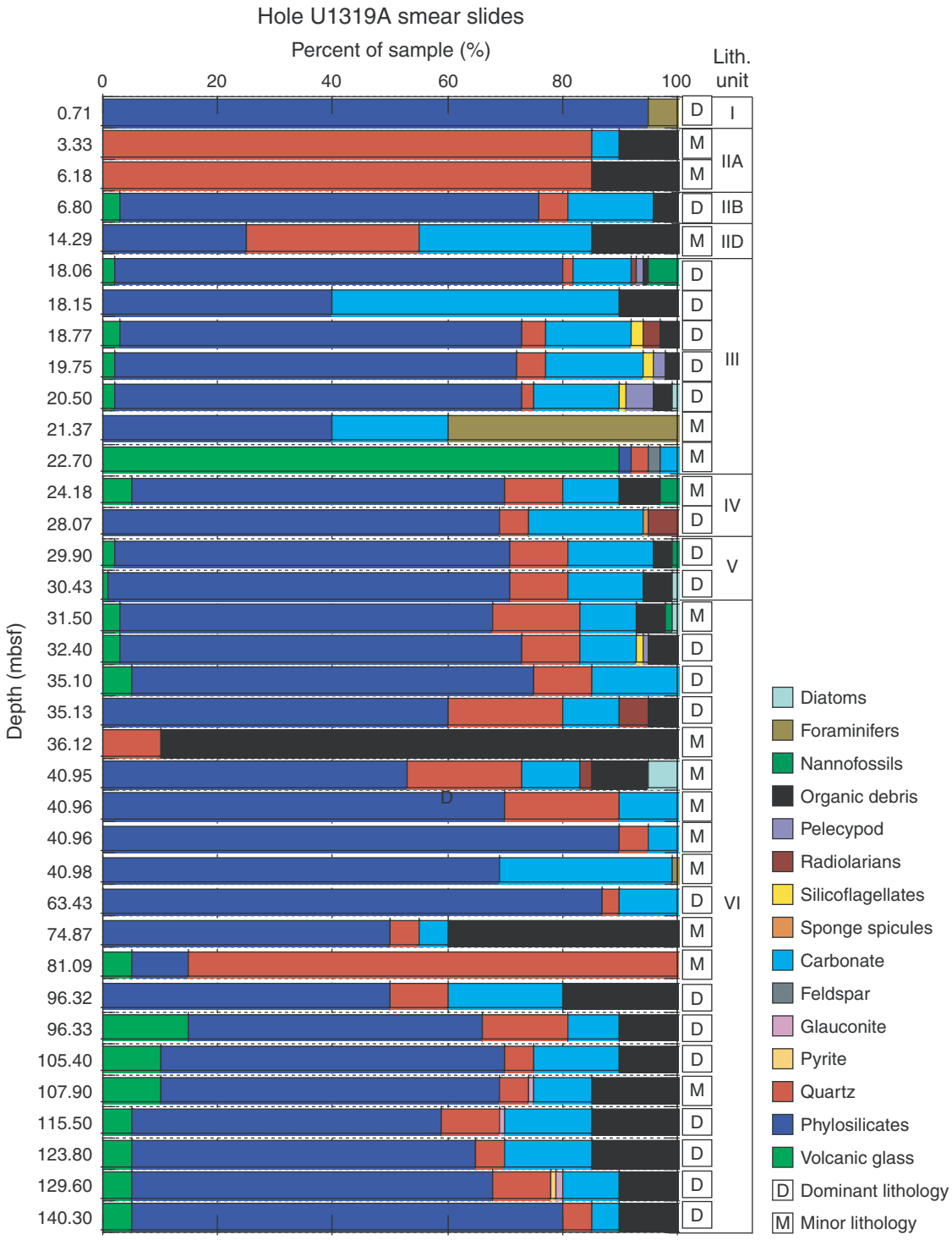

Figure F17. Biostratigraphic summary for Site U1319 shown with lithostratigraphy and seismic reflectors.

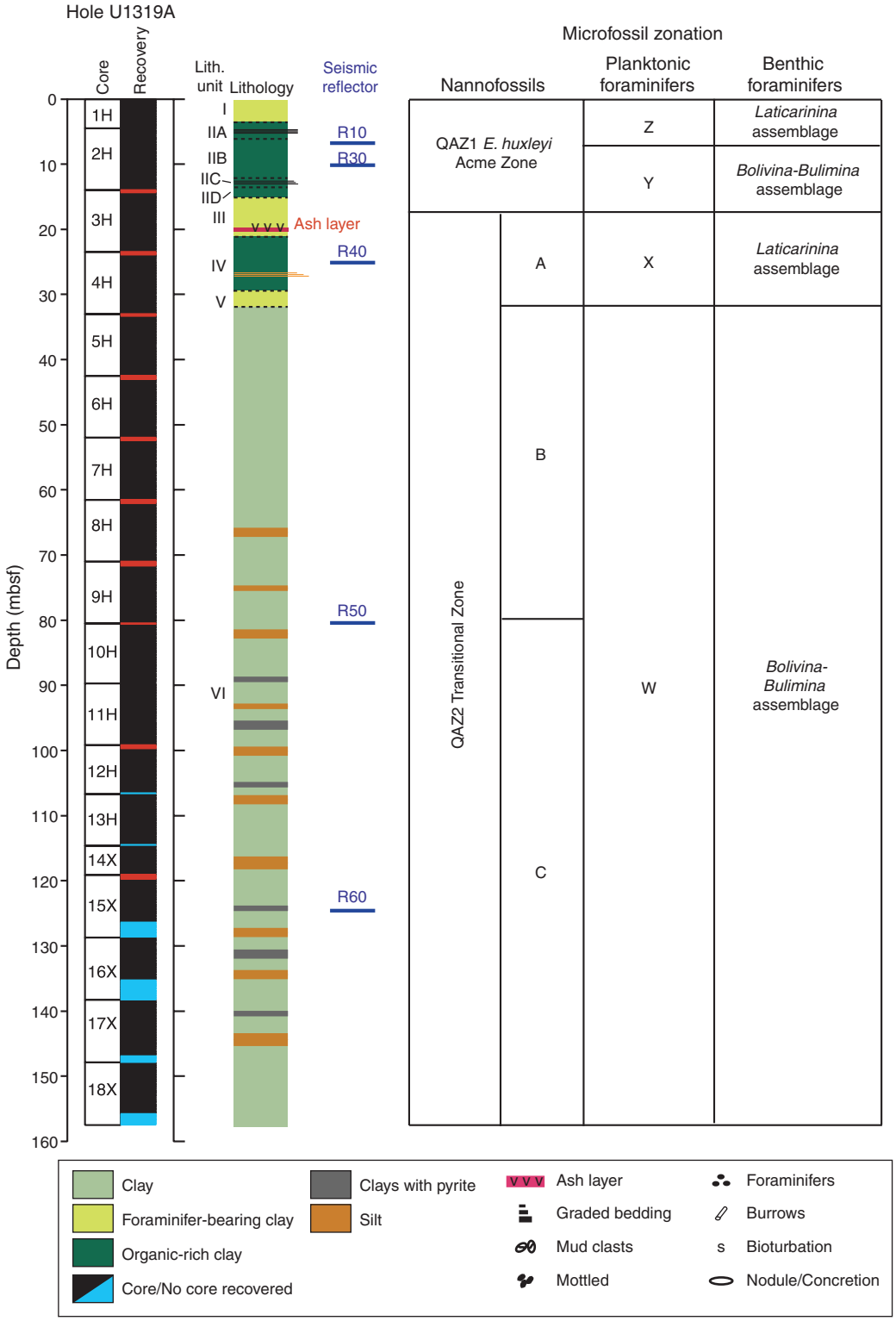

Figure F18. Nannofossil distribution and zones for Hole U1319A showing relative abundances of important nannofossil groups and species.

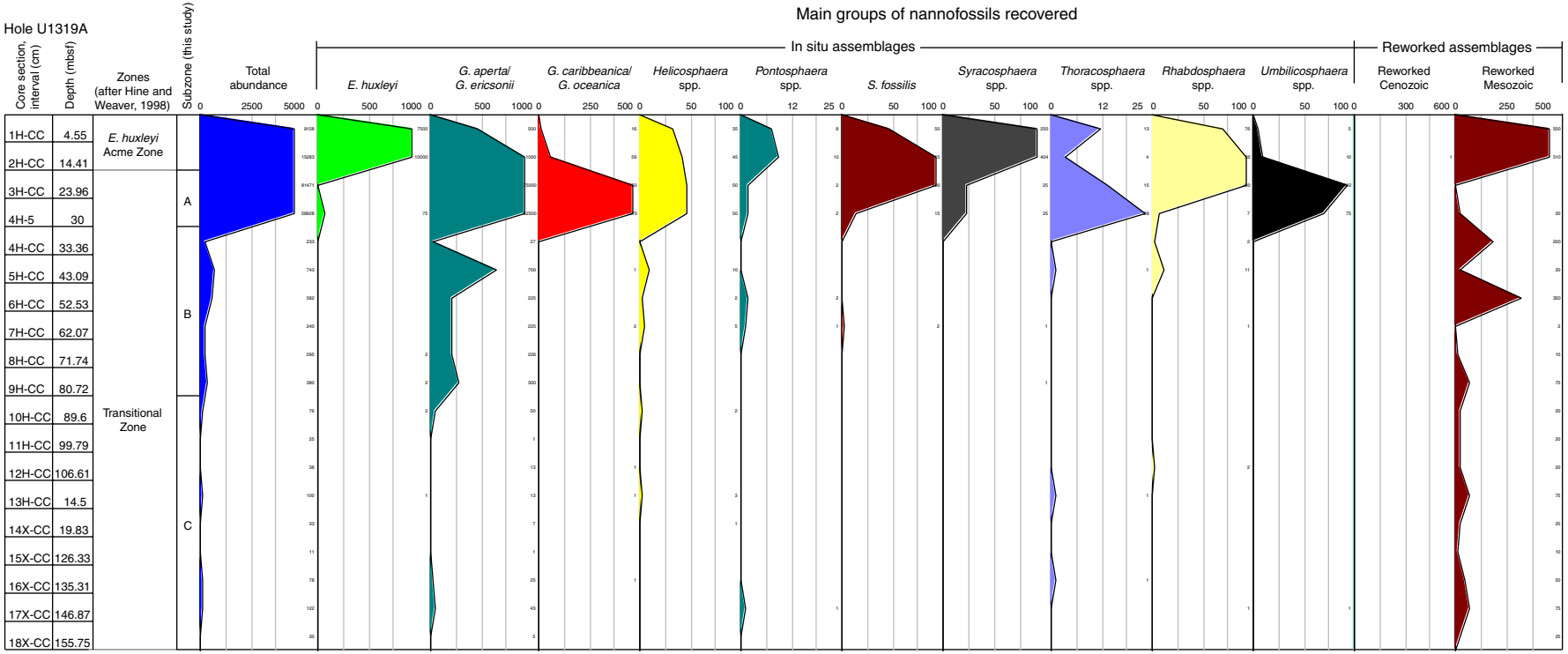

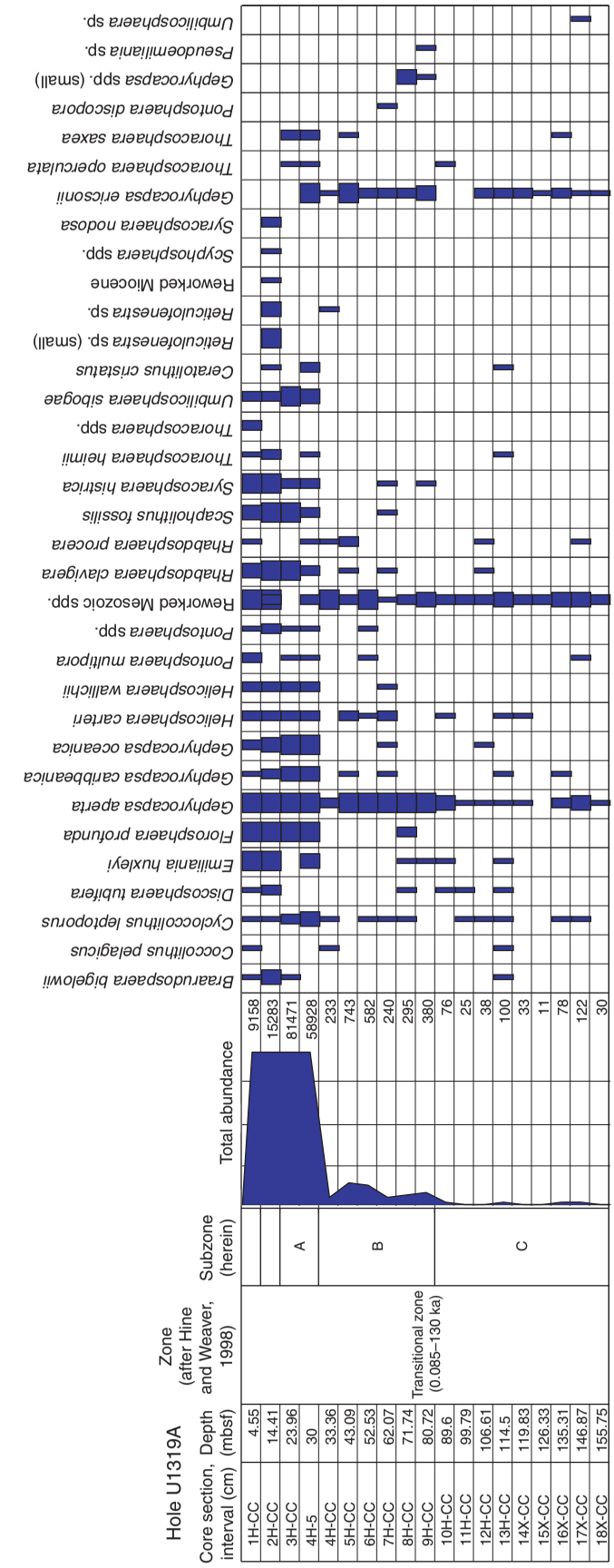

Figure F19. Nannofossil distribution and zonation in Hole U1319A, showing the sporadic pattern for most species.

Figure F20. Planktonic foraminifer biostratigraphy and abundance of selected taxa from Hole U1319A along with marine isotopic stages (MIS).

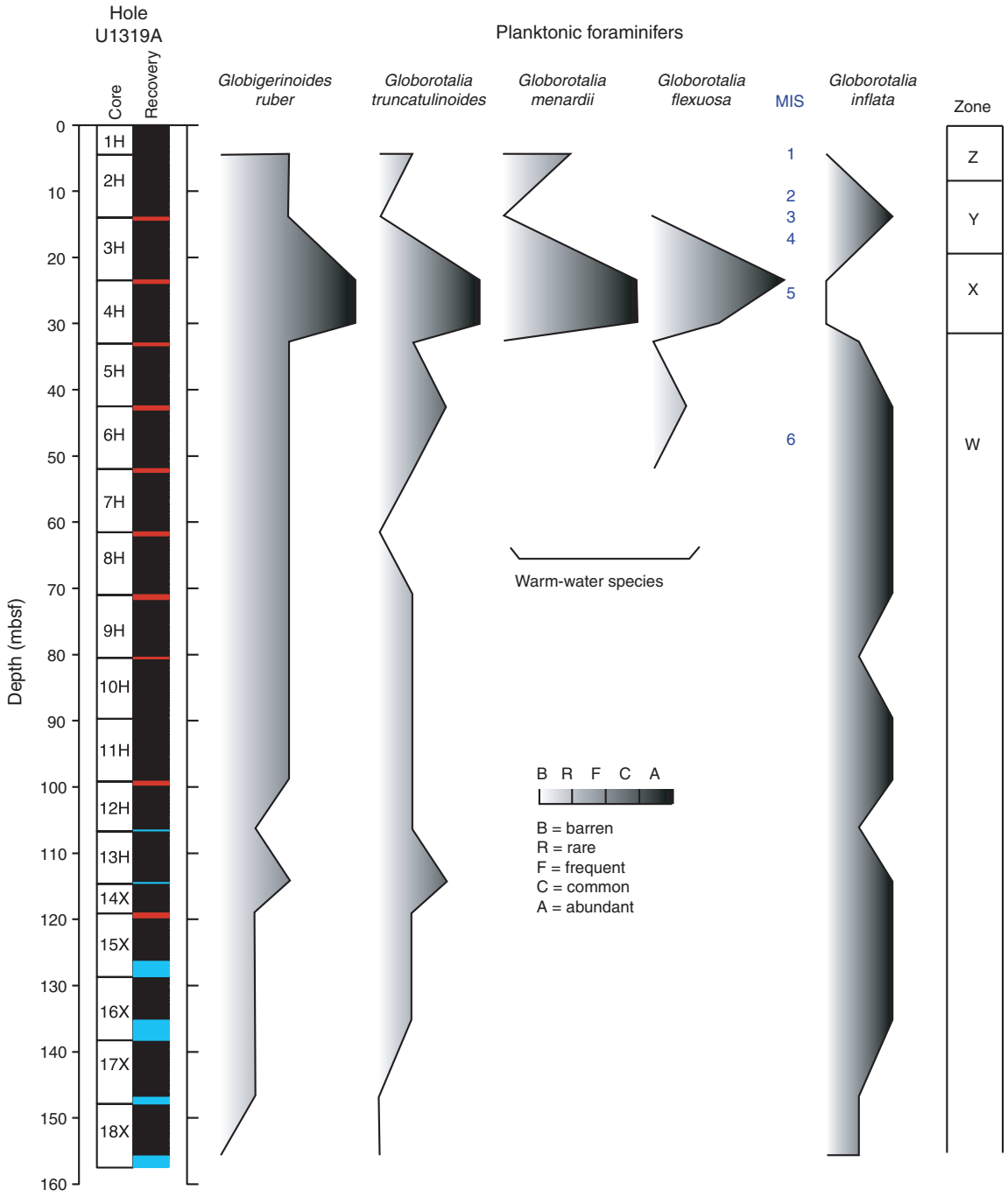

Figure F21. Distribution of selected epifaunal and infaunal benthic foraminifer species from Hole U1319A along with marine isotopic stages (MIS).

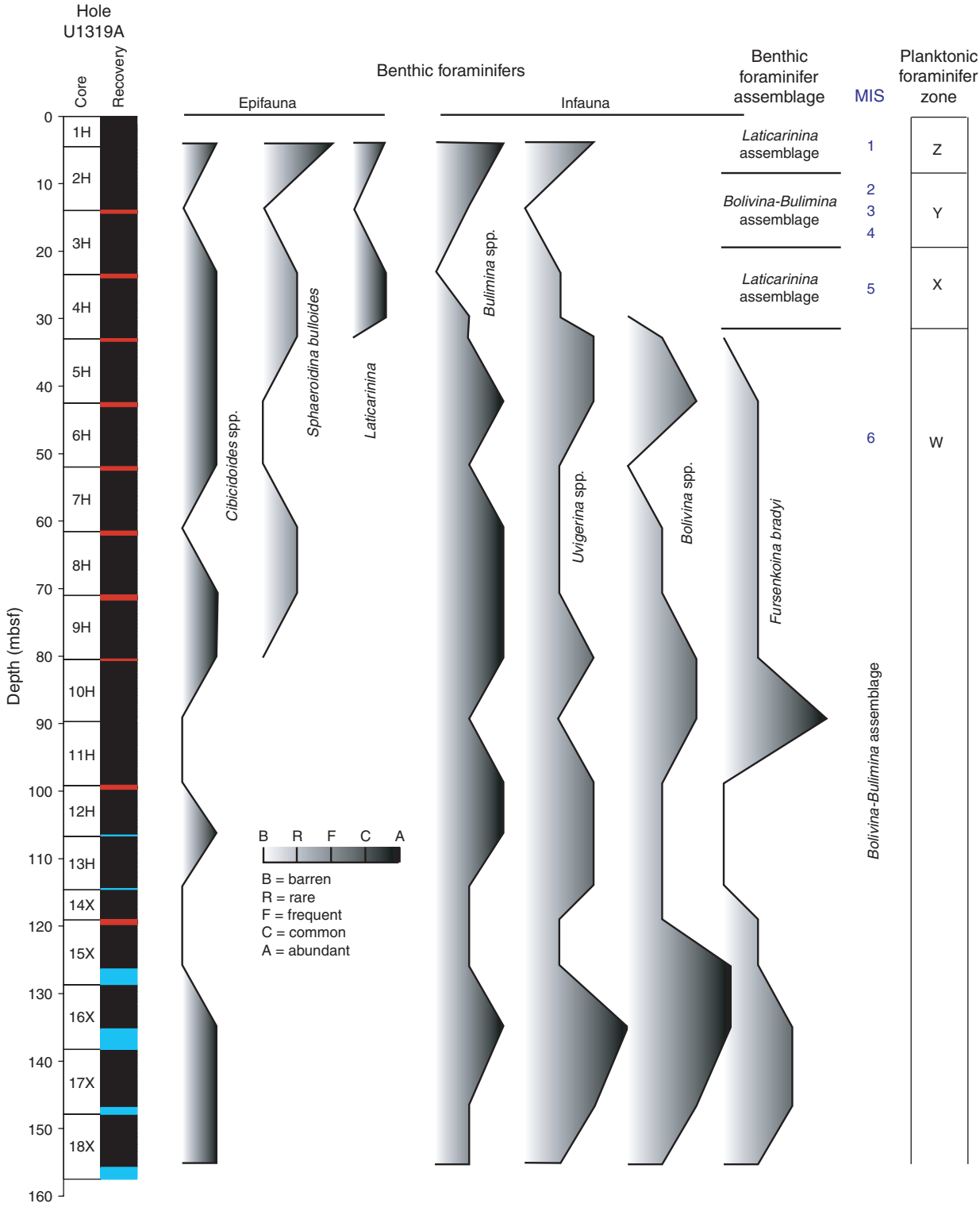

Figure F22. A plot of litho-, bio-, and magnetostratigraphic datums for Hole U1319A, showing rapid sedimentation rate changes at ~30 mbsf (122 ka). Lithostratigraphic units and seismic reflectors are described in "Background and objectives" and "Lithostratigraphy," respectively. SF = seafloor reflector, MIS = marine isotope stage.

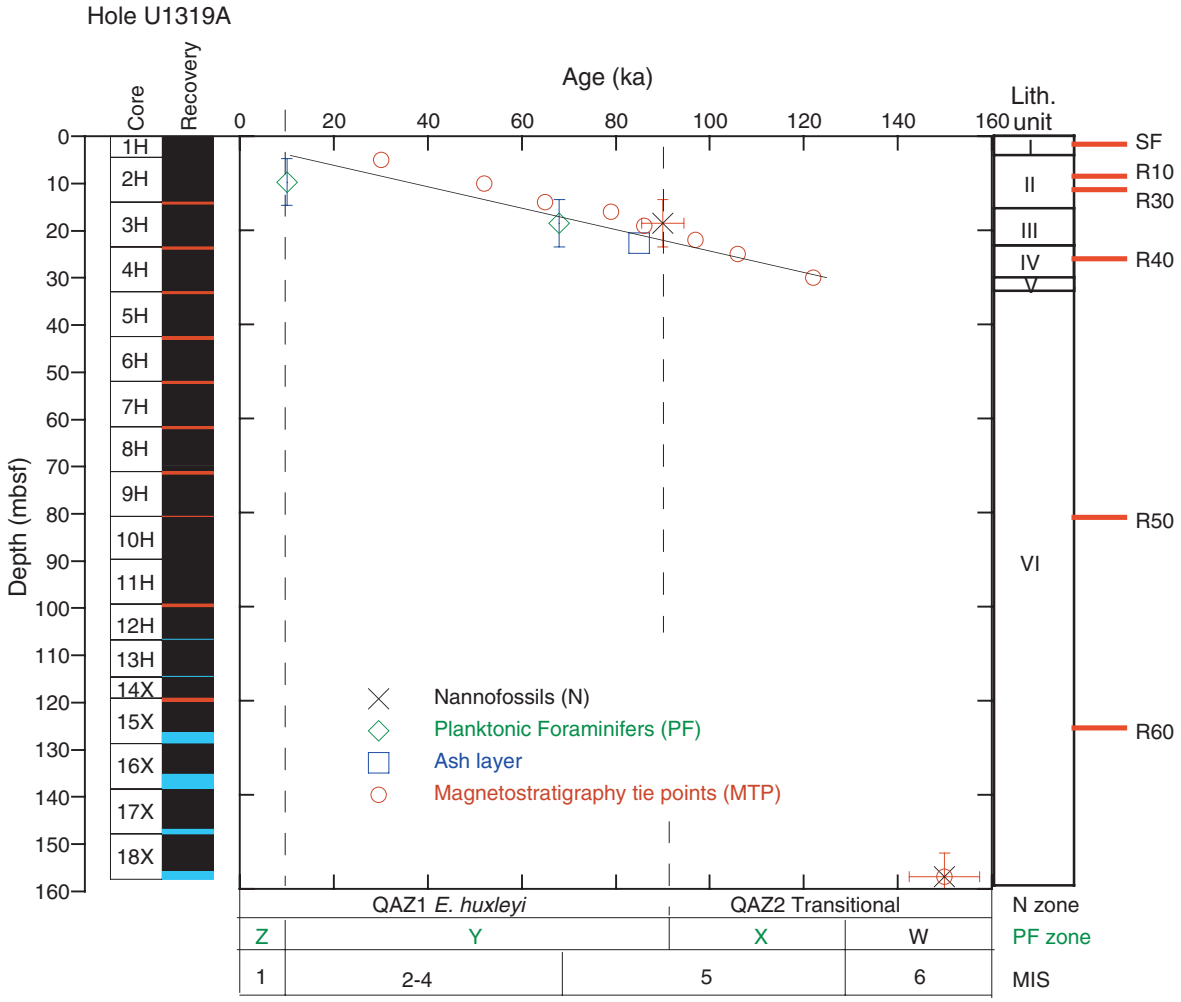

Figure F23. Uncorrected shipboard measurements on archive halves of (**A**) Natural remanent magnetization at 30 mT AF demagnetization (NRM_{30mT}), (**B**) declination, and (**C**) inclination. Depths have been corrected for voids in the core; paleomagnetic intervals, lithostratigraphic units, seafloor (SF), and seismic Reflectors (R) are also shown.

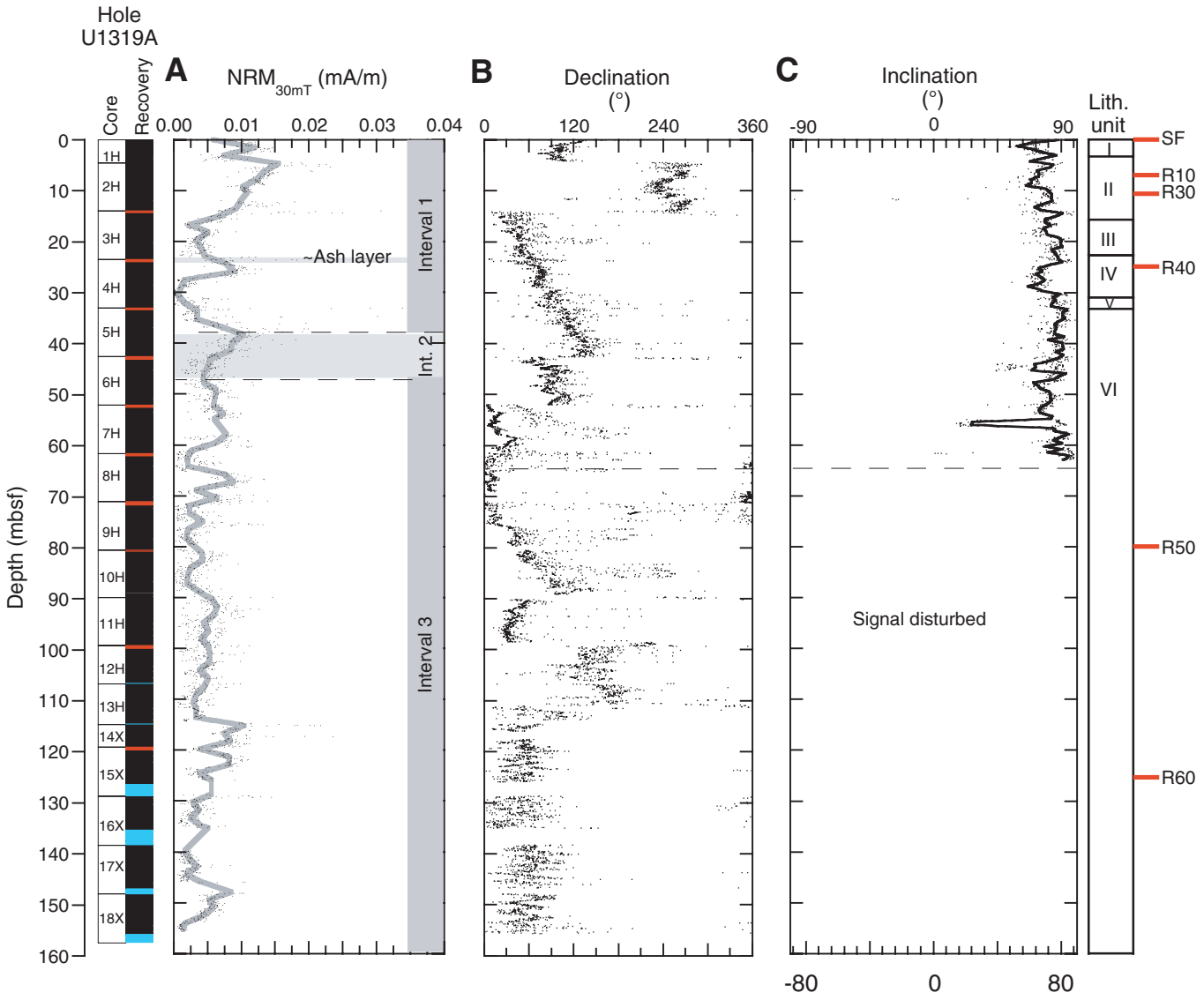

Figure F24. A. Red clay layers (interval 308-U1319A-8H-2, 31–55 cm; 63.05–64.45 mbsf). **B.** Brown silt laminae (interval 308-U1319A-9H-3, 79–112 cm; 74.05–75.45 mbsf).

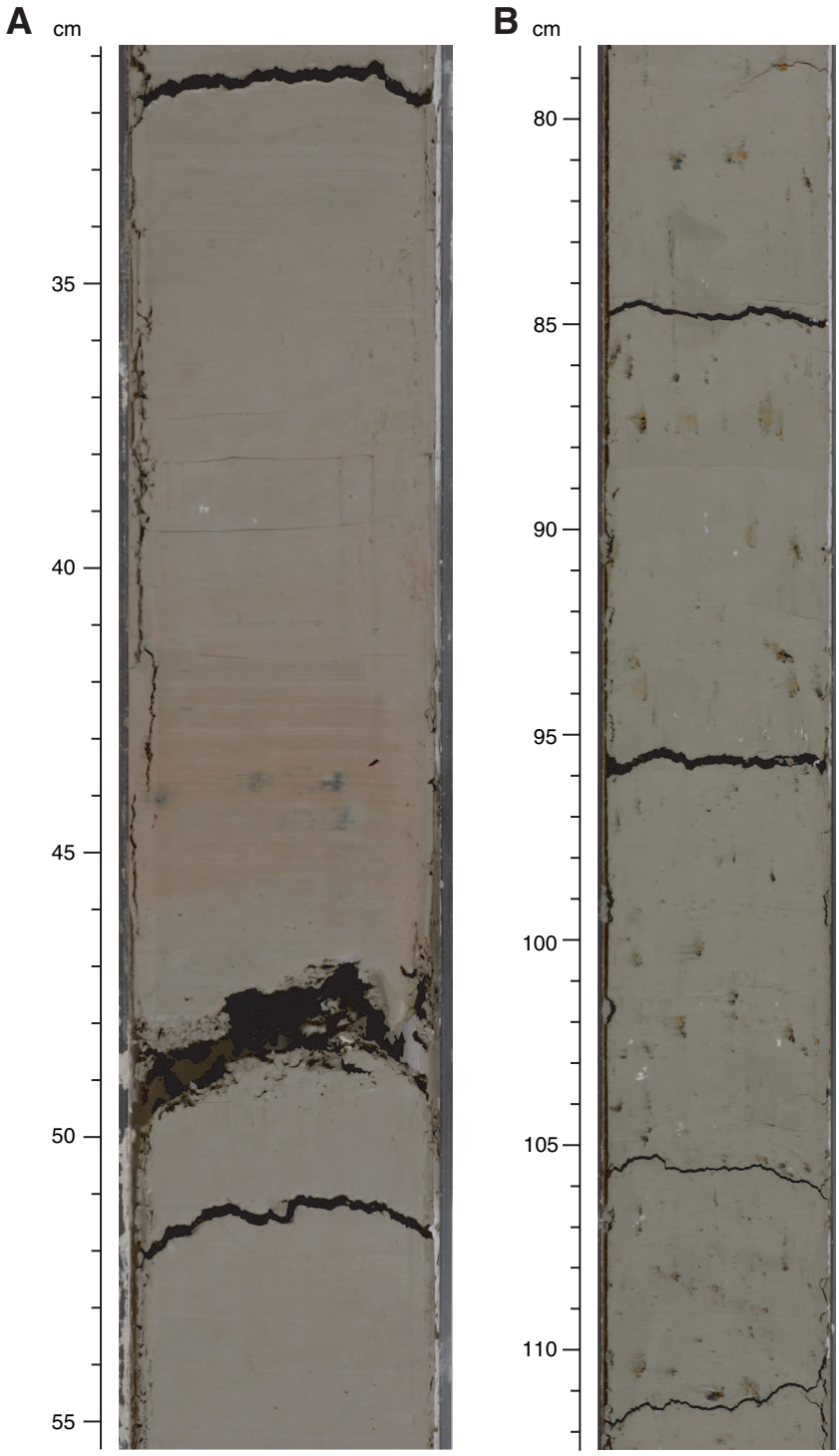

Figure F25. Magnetostratigraphic tie points (MTP) and their relationship with $\delta^{18}O$. Note that the age model can only be tentatively constrained for Interval 1. **A.** $\delta^{18}O$ record (Bassinot et al., 1994) versus age. **B.** NRM_{30mT} intensity, showing the graphical correlation of MTP1–MTP12 with marine isotope stages. **C.** MS2F sensor magnetic point susceptibility performed on archive halves at 5 cm resolution from 0 to 60 mbsf and at 10 cm resolution from 60 mbsf to total depth. **D.** Magnetic susceptibility core logger (multisensor track [MST]) measurements performed on whole cores on the multisensor track at 1 cm resolution throughout Hole U1319A. **E.** Bulk density. Depths have been corrected for voids in the core. Lithostratigraphic units and seismic reflectors (R) are also shown (SF = seafloor reflector).

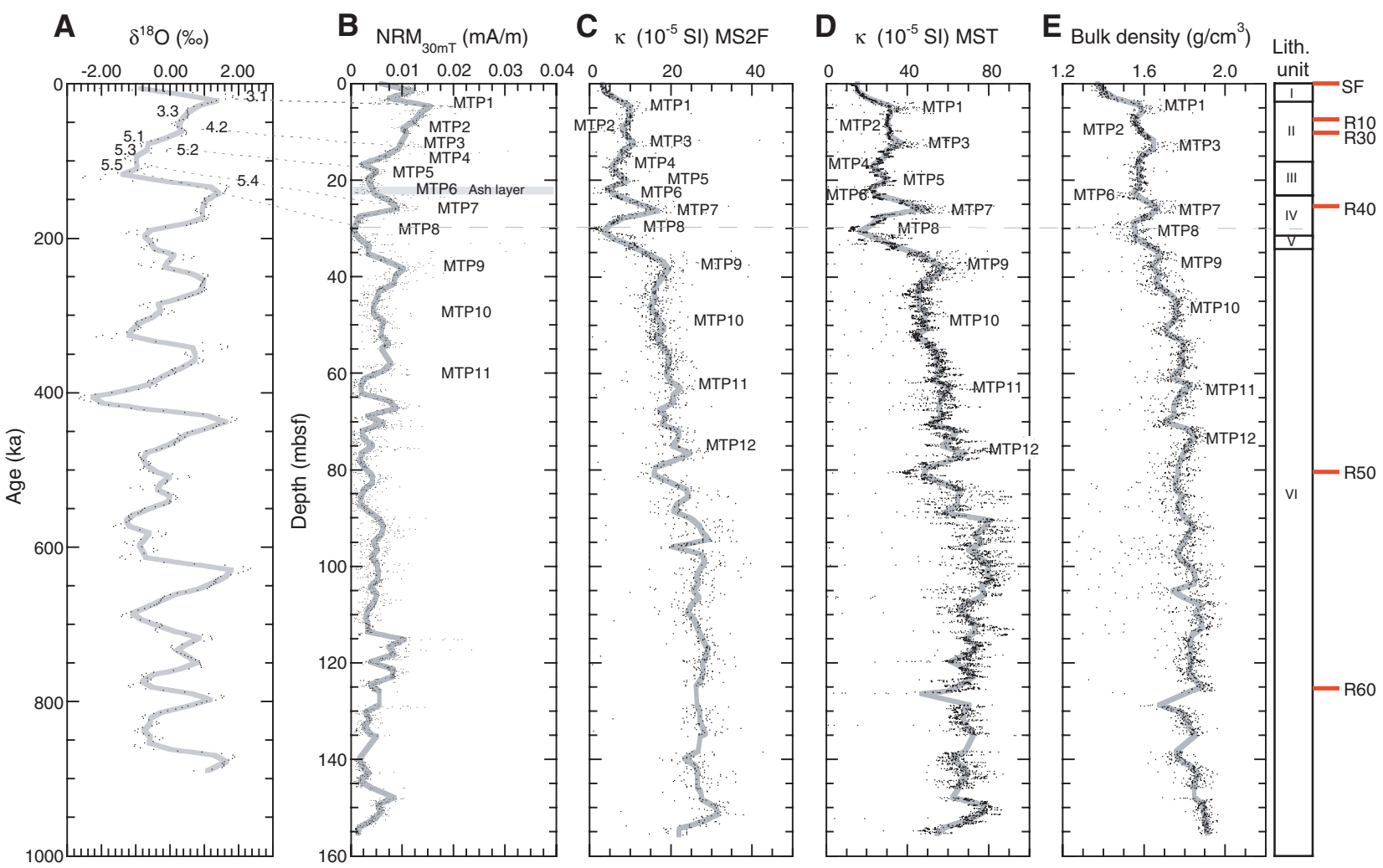

Figure F26. Interstitial water concentration profiles for alkalinity, pH, salinity, and chlorinity along with core recovery, lithostratigraphic units, and seismic reflectors (SF = seafloor).

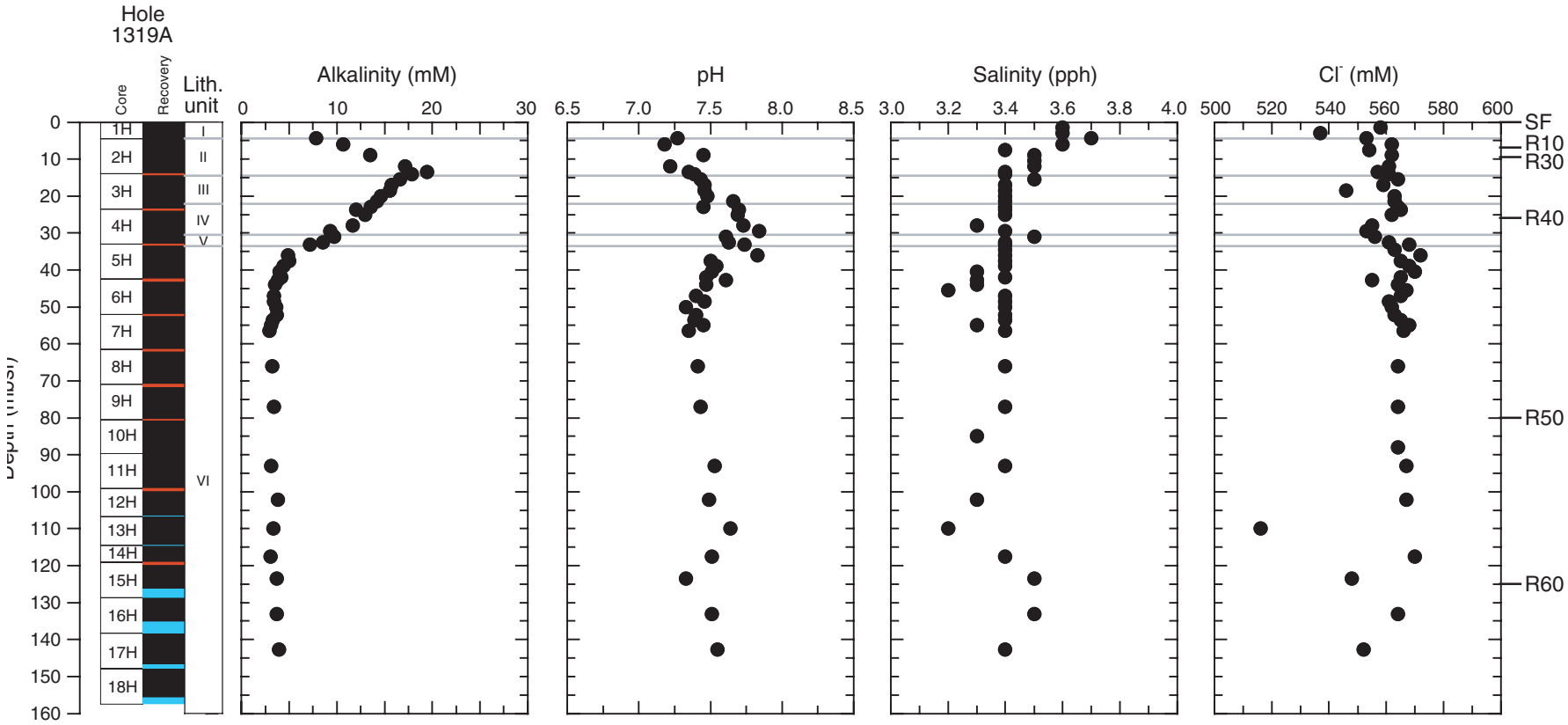

Figure F27. Interstitial water concentration profiles for sulfate, phosphate, ammonium, and silica along with core recovery, seismic lithostratigraphic units, and seismic reflectors (SF = seafloor).

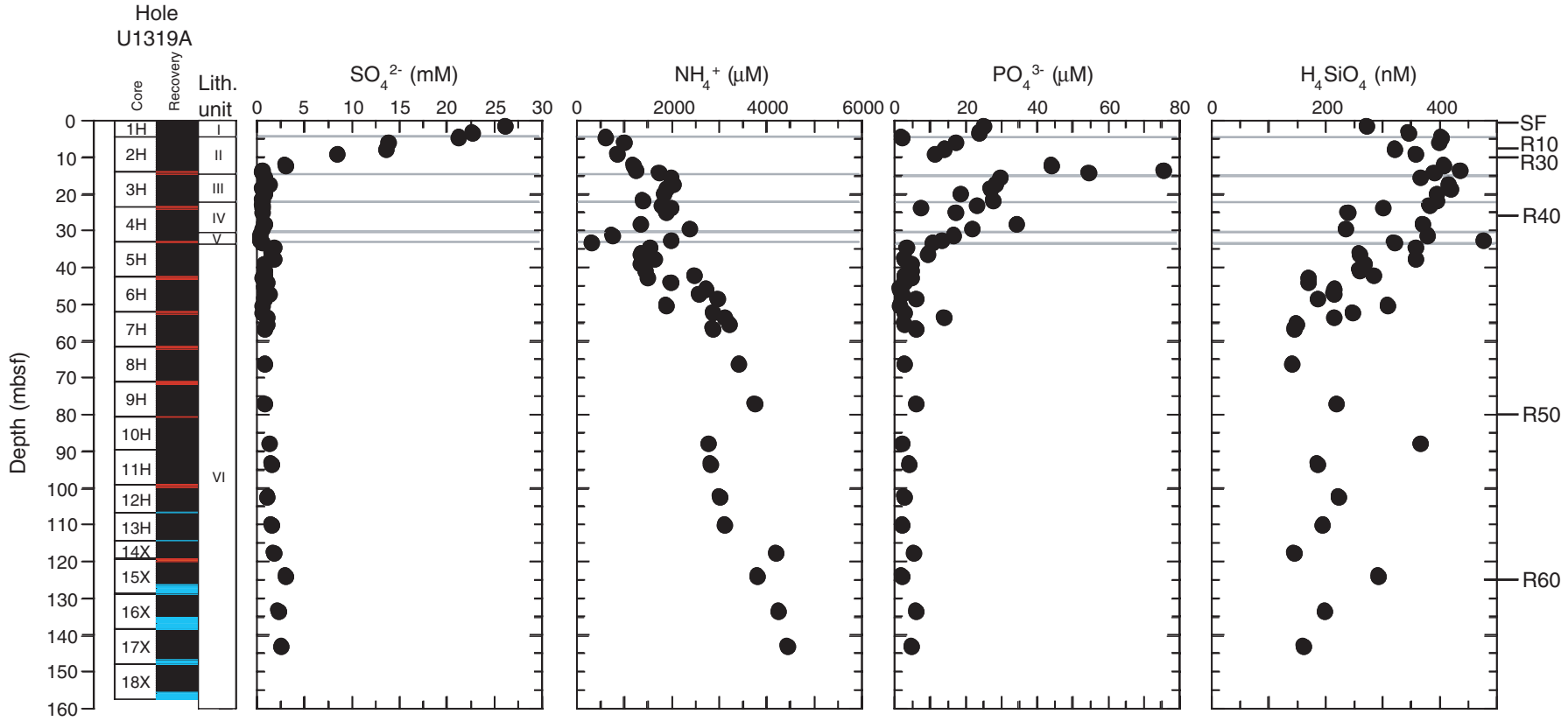

Figure F28. Interstitial water variations in major cations Na^+, K^+, Ca^{2+}, and Mg^{2+} along with core recovery, lithostratigraphic units, and seismic reflectors (SF = seafloor).

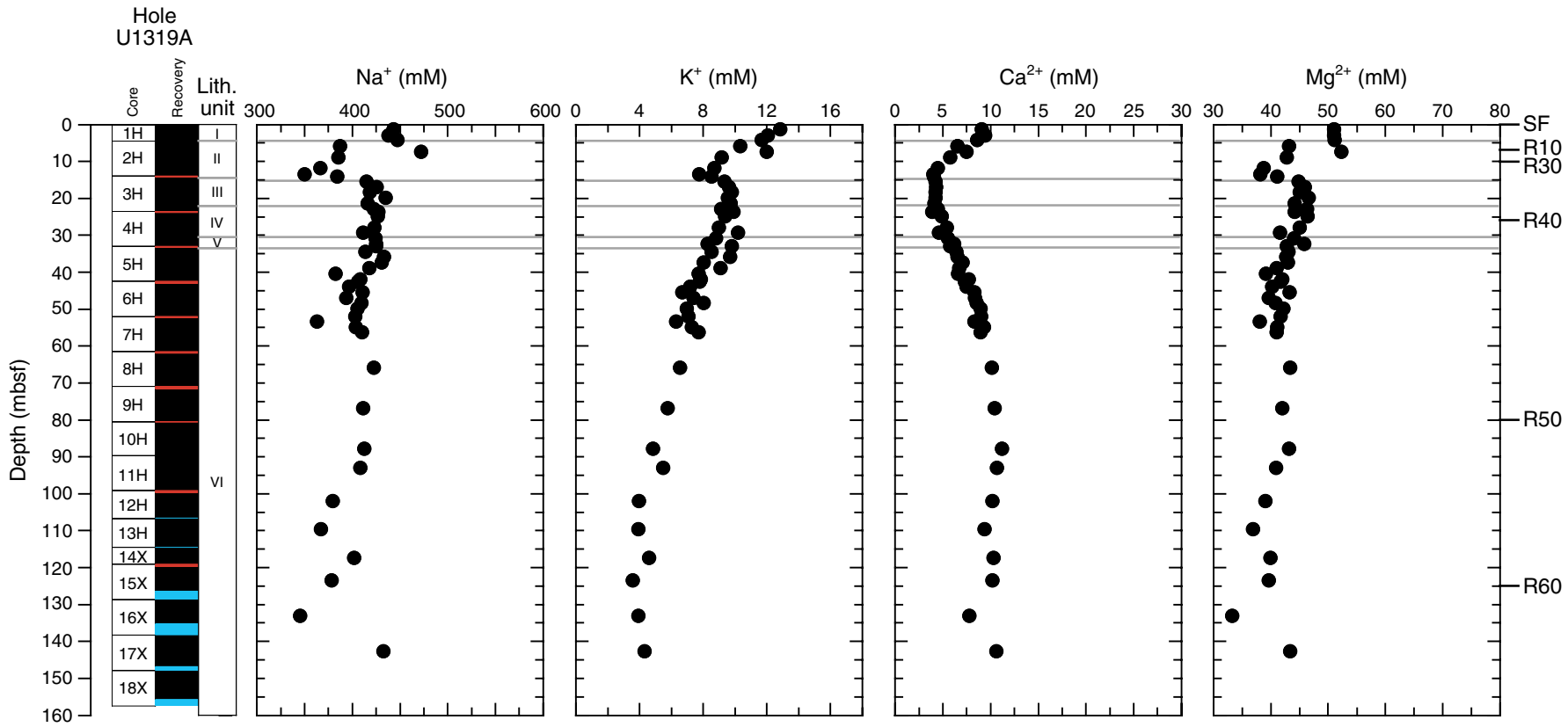

Figure F29. Interstitial water variations in trace metals B^{3+}, Li^{+}, and Sr^{2+} along with core recovery, lithostratigraphic units, and seismic reflectors (SF = seafloor). (Continued on next page).

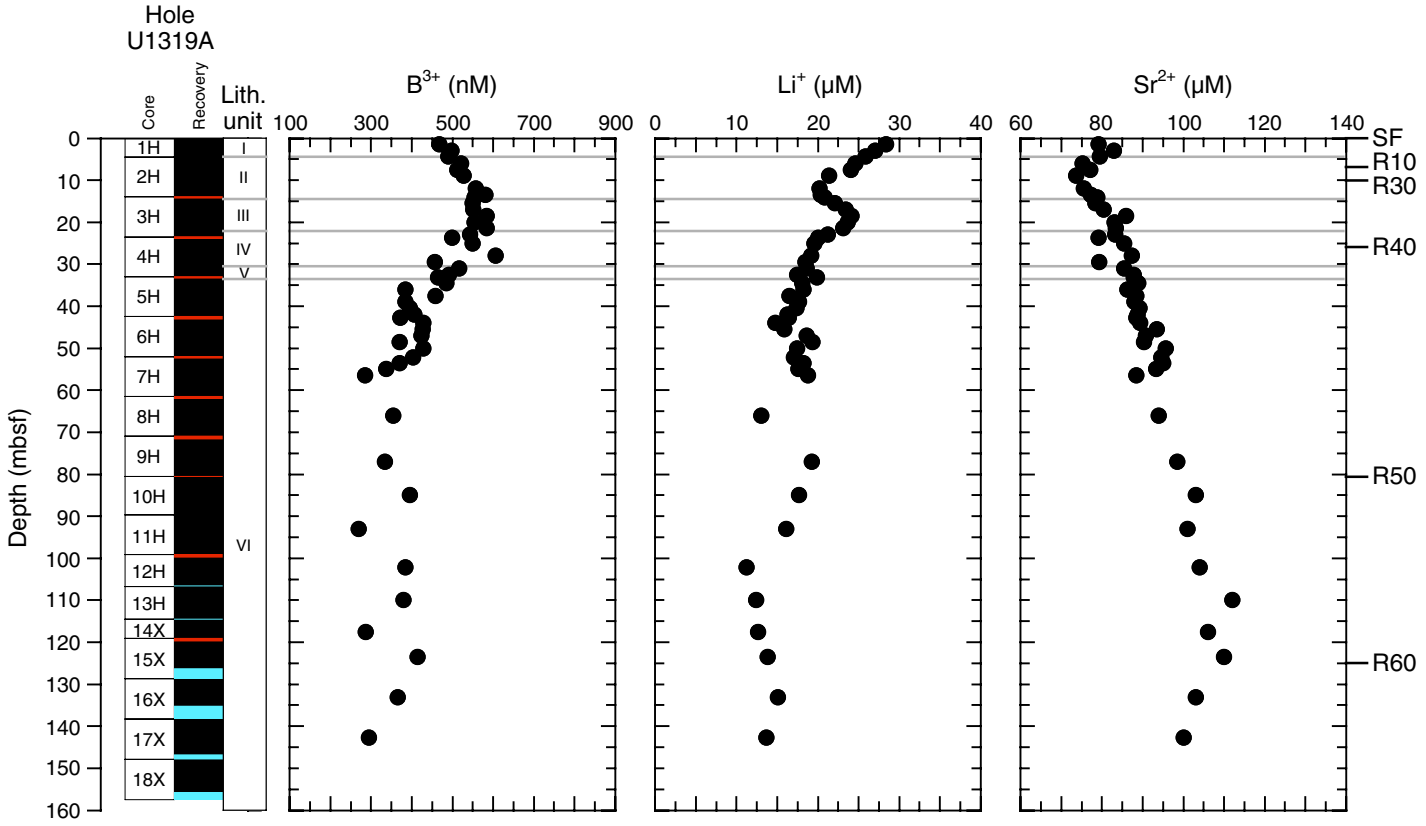

Figure F29 (continued). Ba^{2+}, Fe^{2+}, and Mn^{2+} profiles.

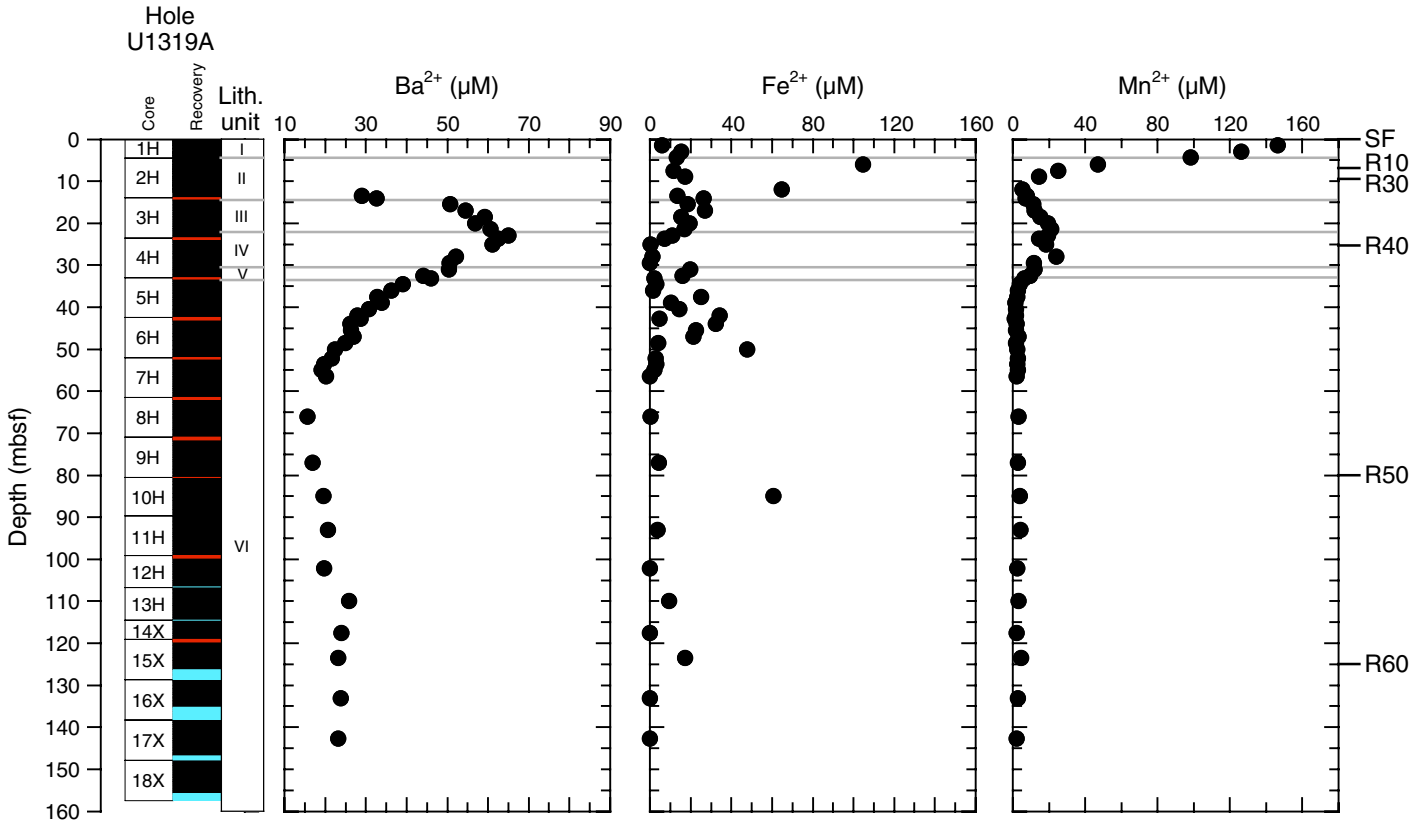

Figure F30. Downhole variations in total inorganic carbon (TIC), calcium carbonate ($CaCO_3$), total organic carbon (TOC), total nitrogen (TN), C/N, and total hydrogen (TH) in sediments from Hole U1319A along with core recovery, lithostratigraphic units, and seismic reflectors (SF = sea-floor).

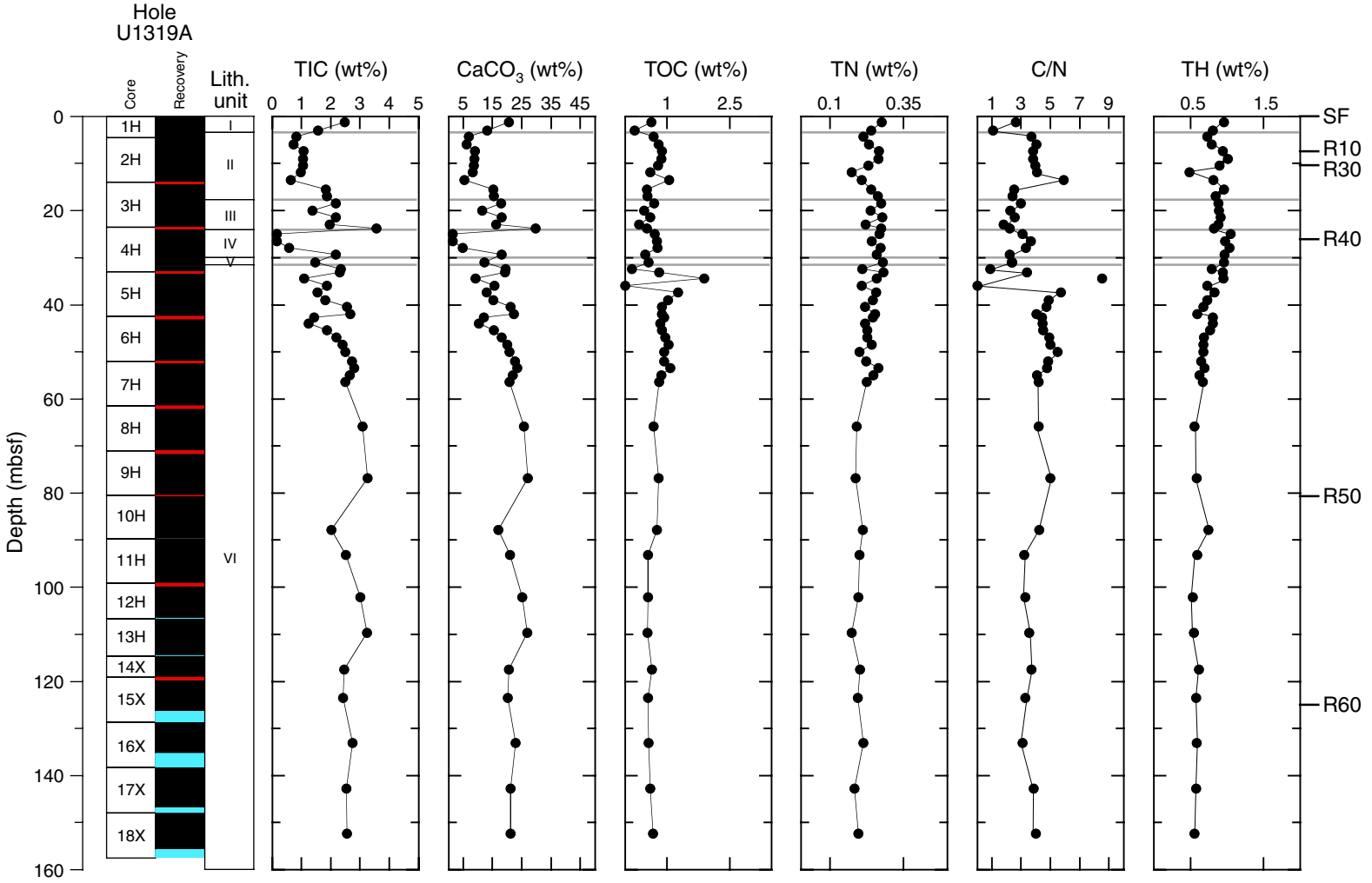

Figure F31. Headspace gases methane and ethane in Hole U1319A along with core recovery, lithostratigraphic units, and seismic reflectors (SF = seafloor).

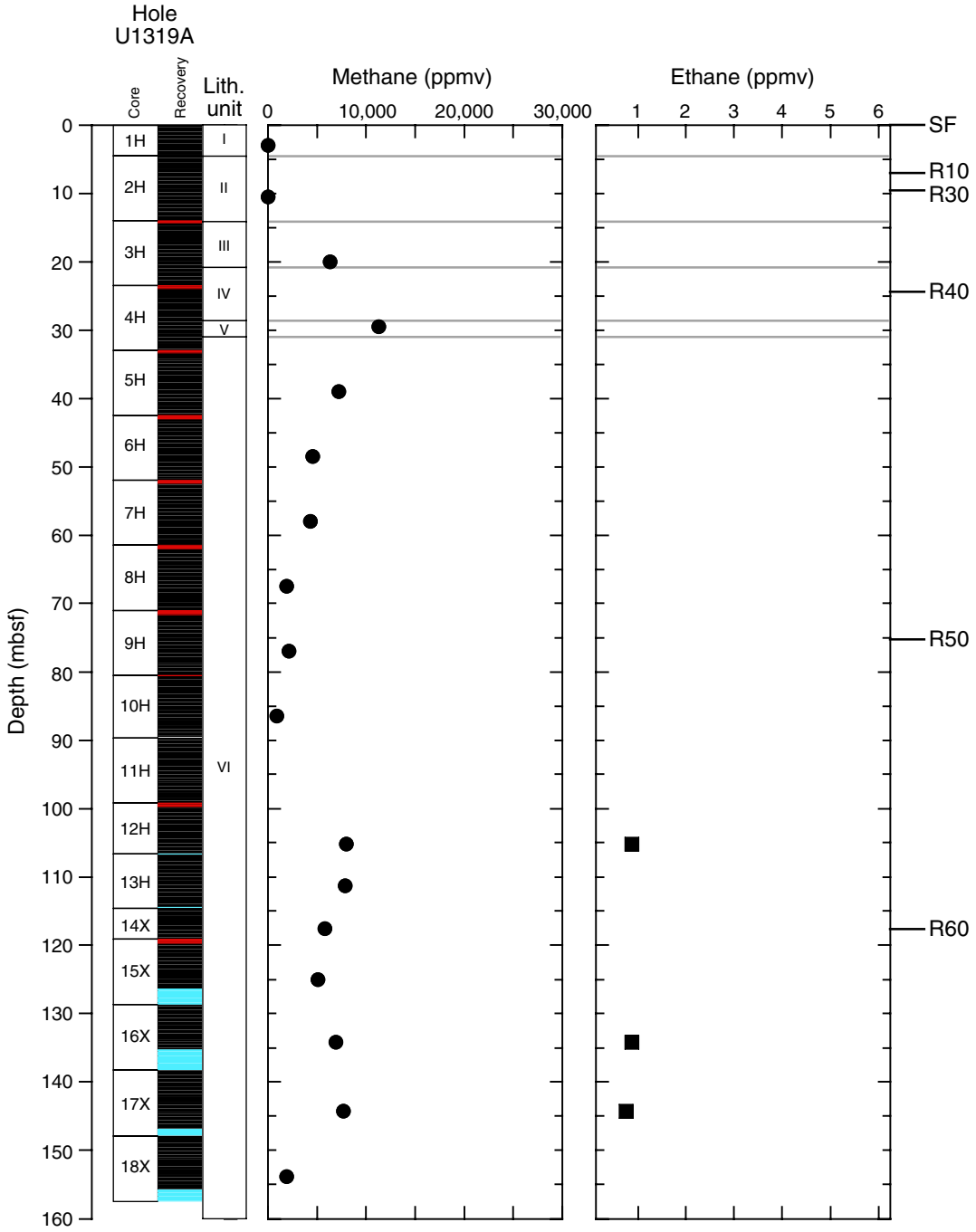

Figure F32. Profiles of methane and sulfate concentrations in Hole U1319A along with lithostratigraphic units and seismic reflectors (SF = seafloor).

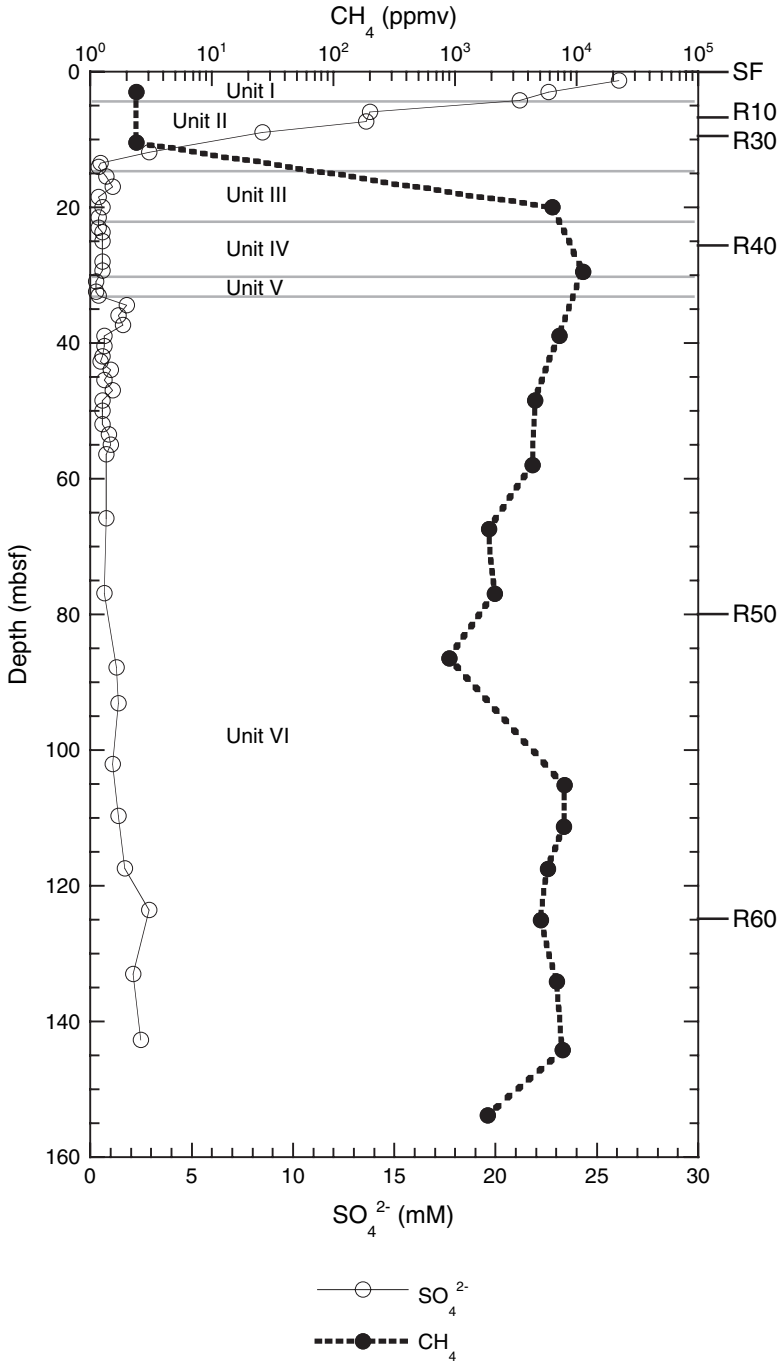

Figure F33. Depth profile of cell densities in Hole U1319A along with core recovery, lithostratigraphic units, and seismic reflectors (SF = seafloor). Closed symbols = detected density, open symbols = not detected or below detection.

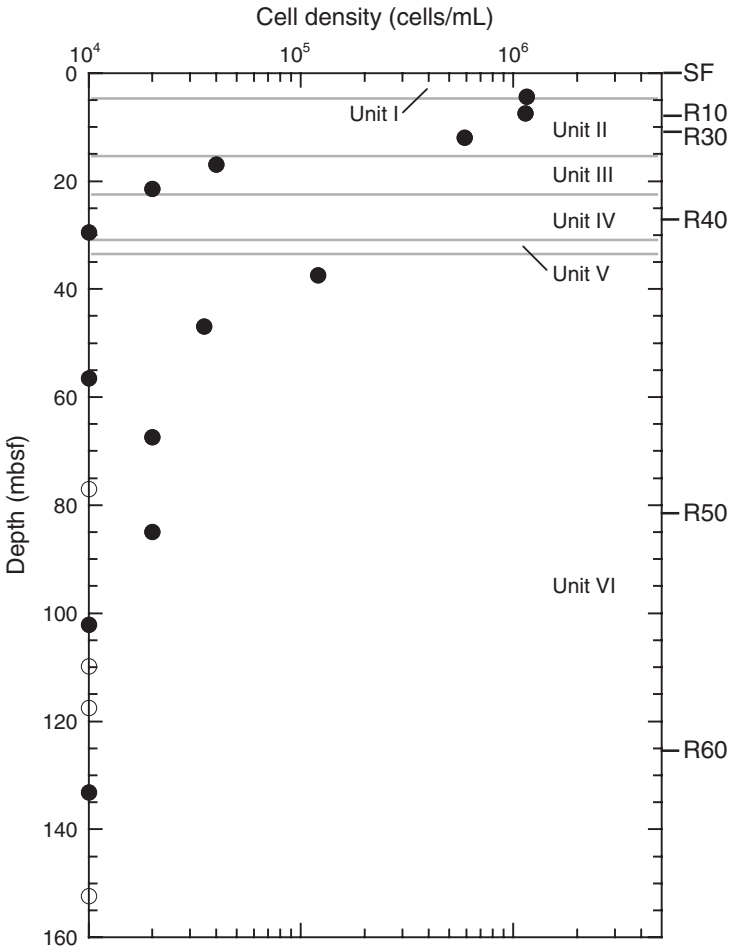

Figure F34. (**A**) Bulk density from moisture and density (MAD), multisensor track (MST), and measurement while drilling (MWD), (**B**) grain density, and (**C**) porosity, along with lithostratigraphic units and seismic reflectors (SF = seafloor).

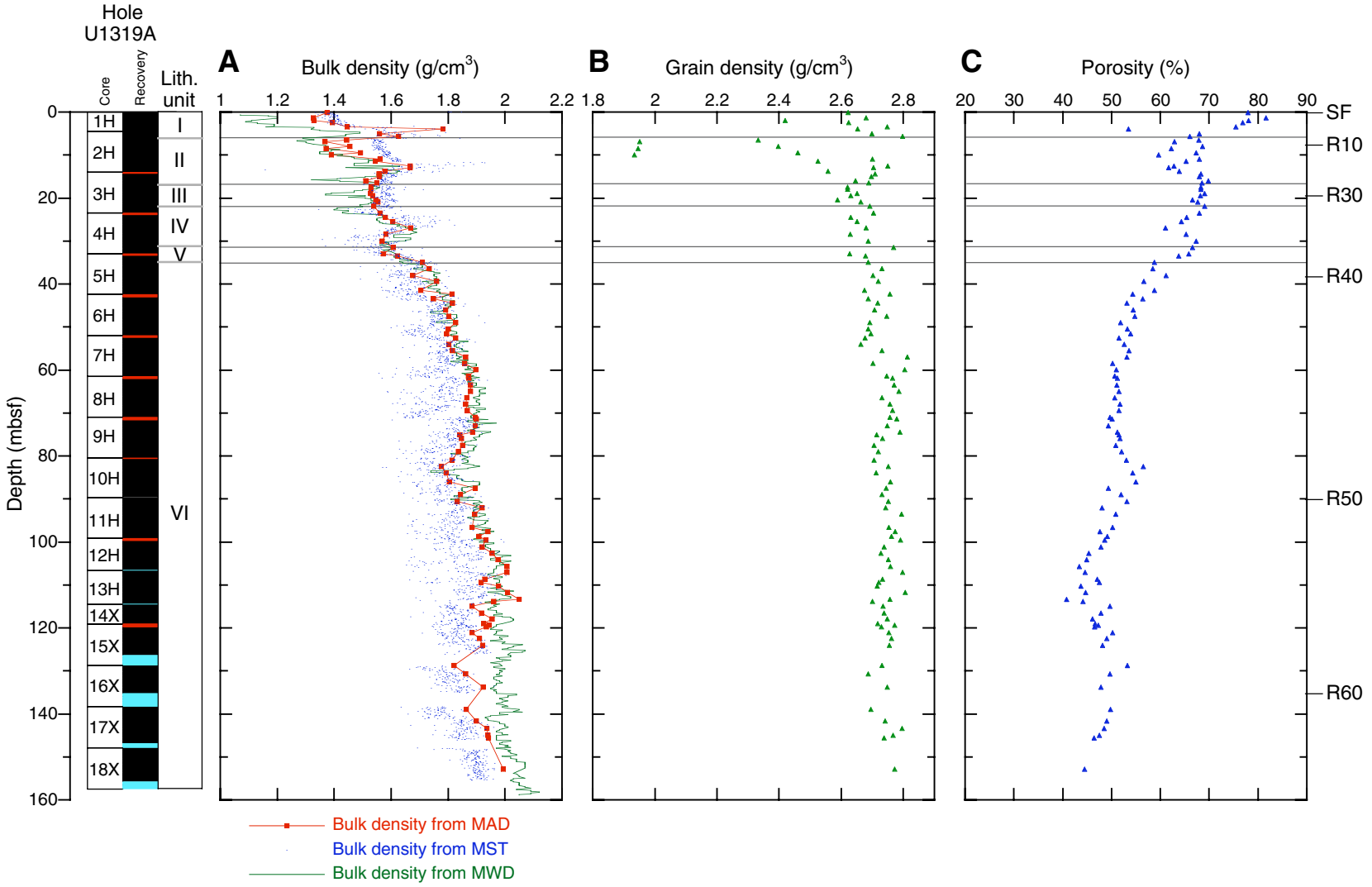

Figure F35. (**A**) Noncontact resistivity and (**B**) magnetic susceptibility, along with lithostratigraphic units and seismic reflectors (SF = seafloor).

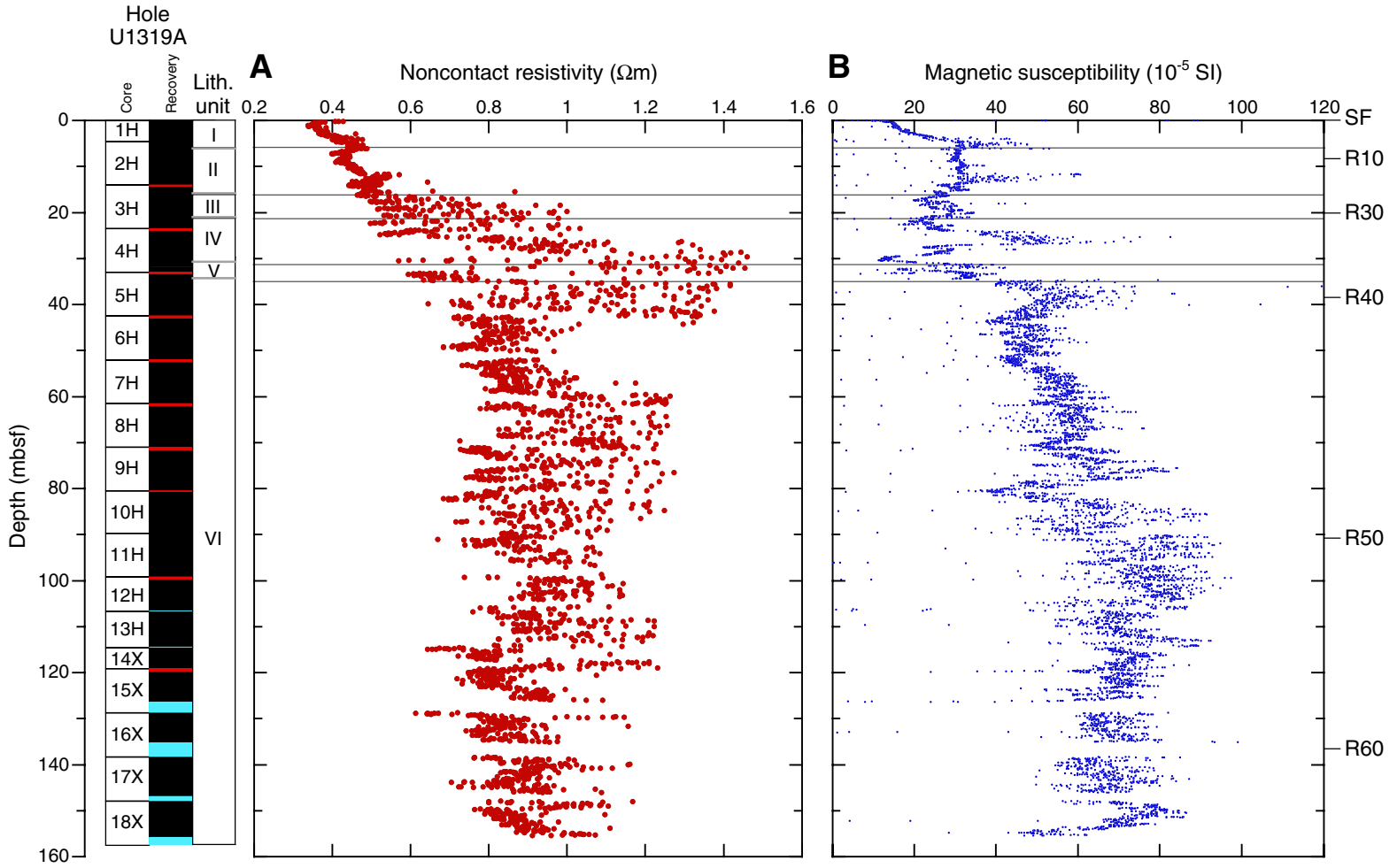

Figure F36. (**A**) Thermal conductivity and (**B**) *P*-wave velocity, along with lithostratigraphic units and seismic reflectors (SF = seafloor). x, y, z = *P*-wave velocity (PWS) measured in the x-, y-, and z-directions, respectively.

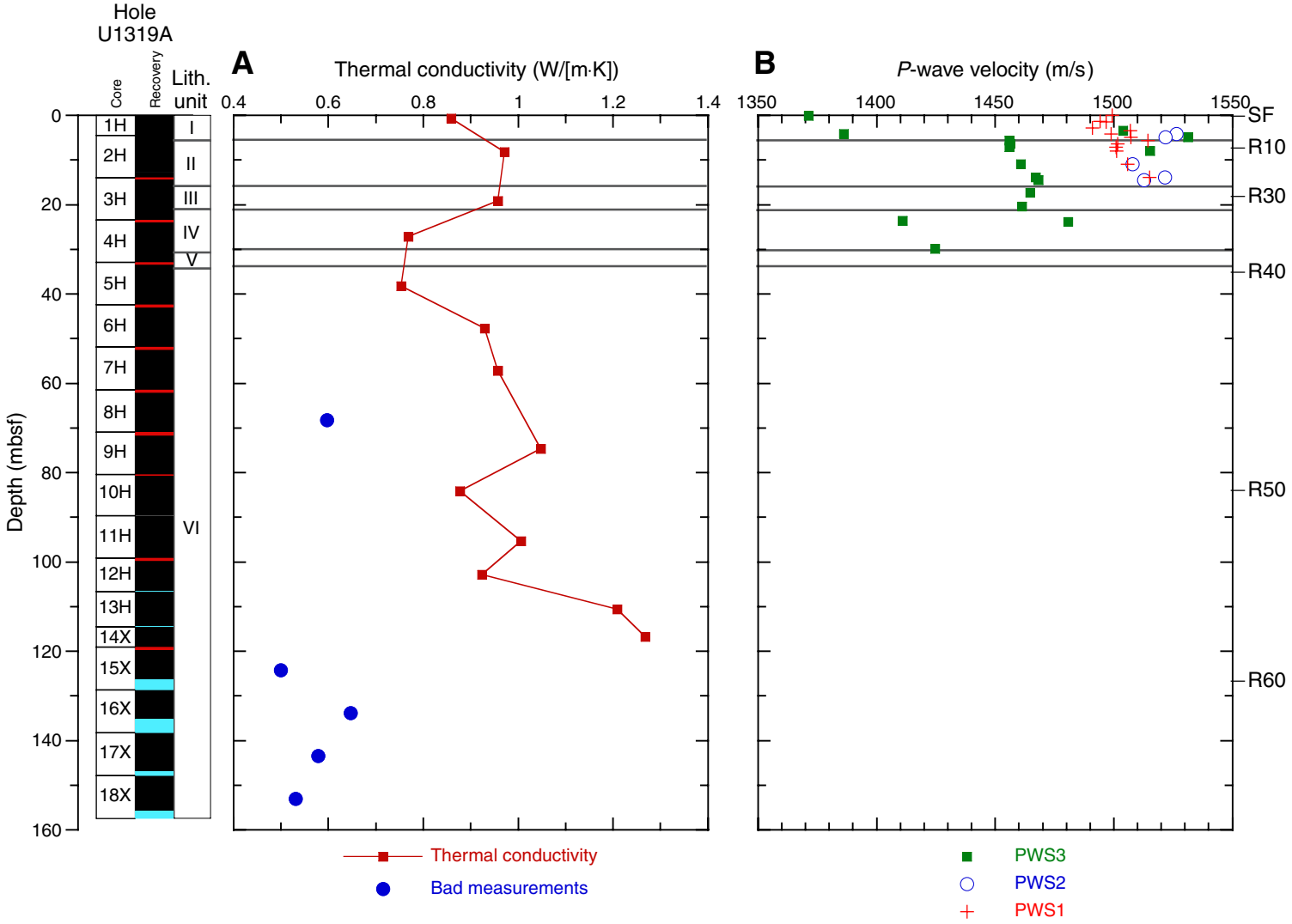

Figure F37. (**A**) Peak and residual undrained shear strength from vane shear tests, (**B**) peak undrained shear strengths measured using the vane and pocket penetrometer, and (**C**) sensitivity (peak/residual undrained shear strength), along with lithostratigraphic units and seismic reflectors (SF = seafloor).

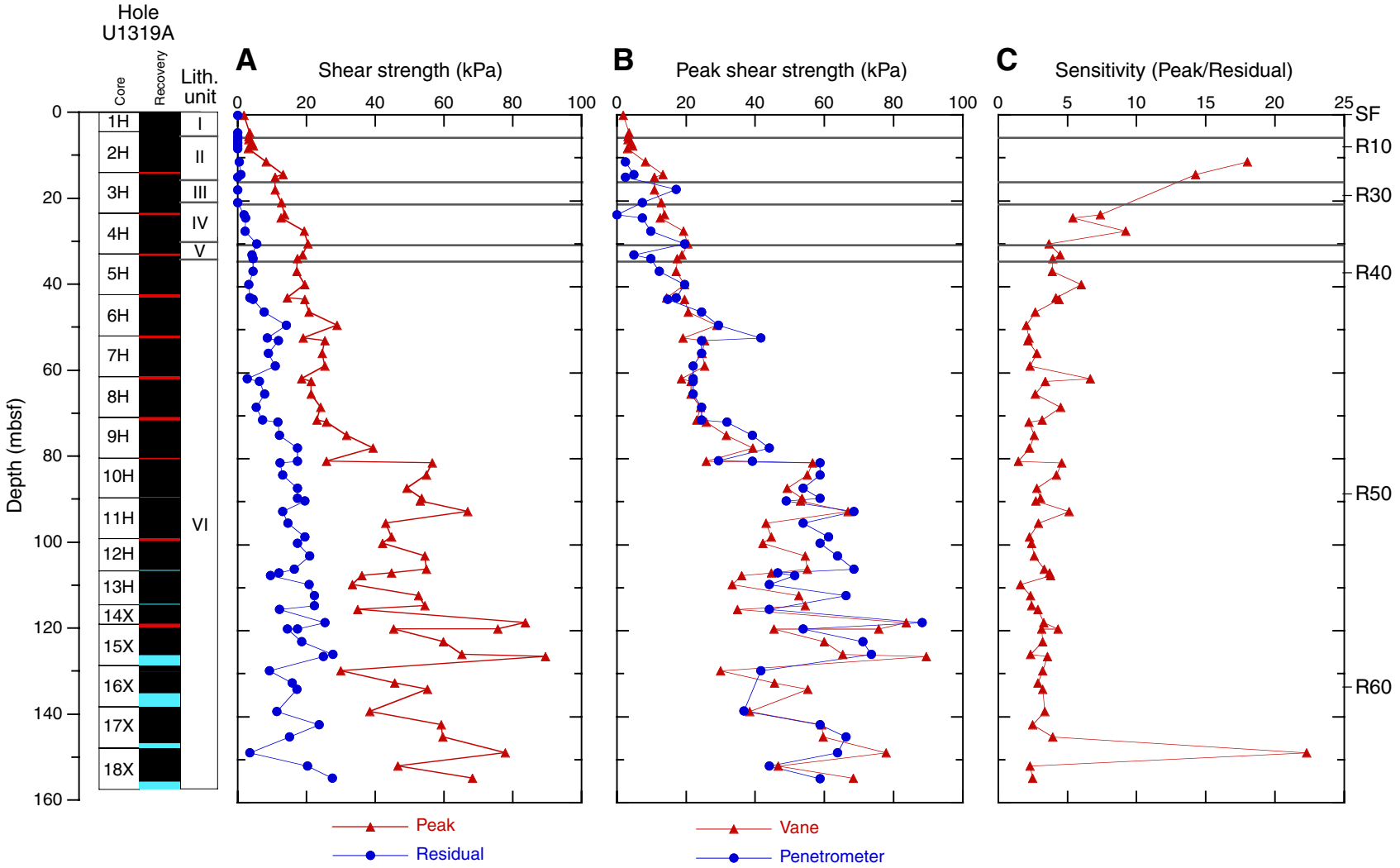

Figure F38. (**A**) Comparison between the undrained peak shear strength (red squares) and isolines representing constant peak shear strength to vertical hydrostatic effective stress (σ_{vh}') ratios and (**B**) vertical hydrostatic effective stress (σ_{vh}') and total vertical stress (σ_v) based on hydrostatic conditions, along with lithostratigraphic units and seismic reflectors (SF = seafloor).

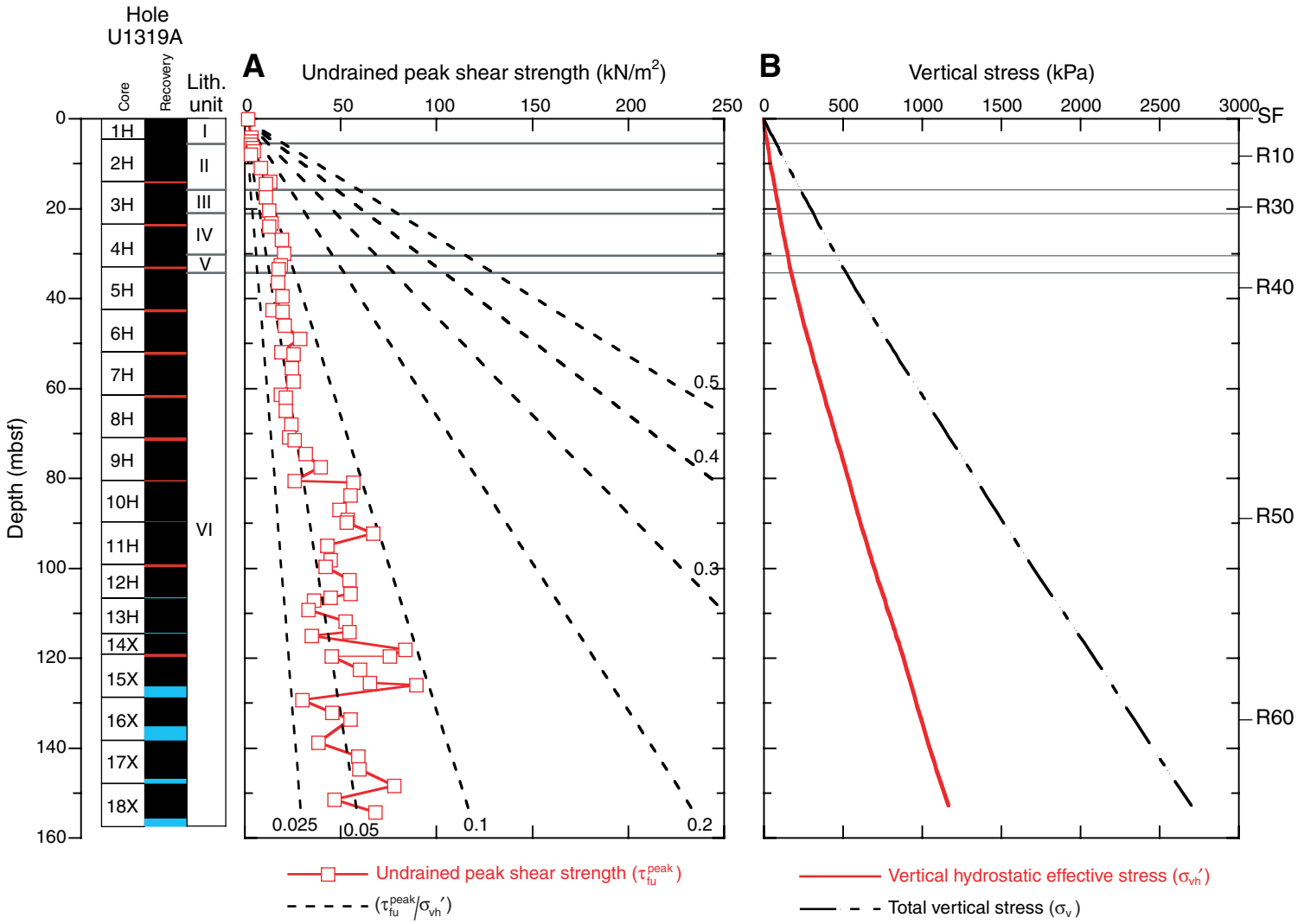

Figure F39. Data quality of curves for MWD/LWD measurements showing the rate of penetration, density-derived caliper, and density correction based on hole diameter.

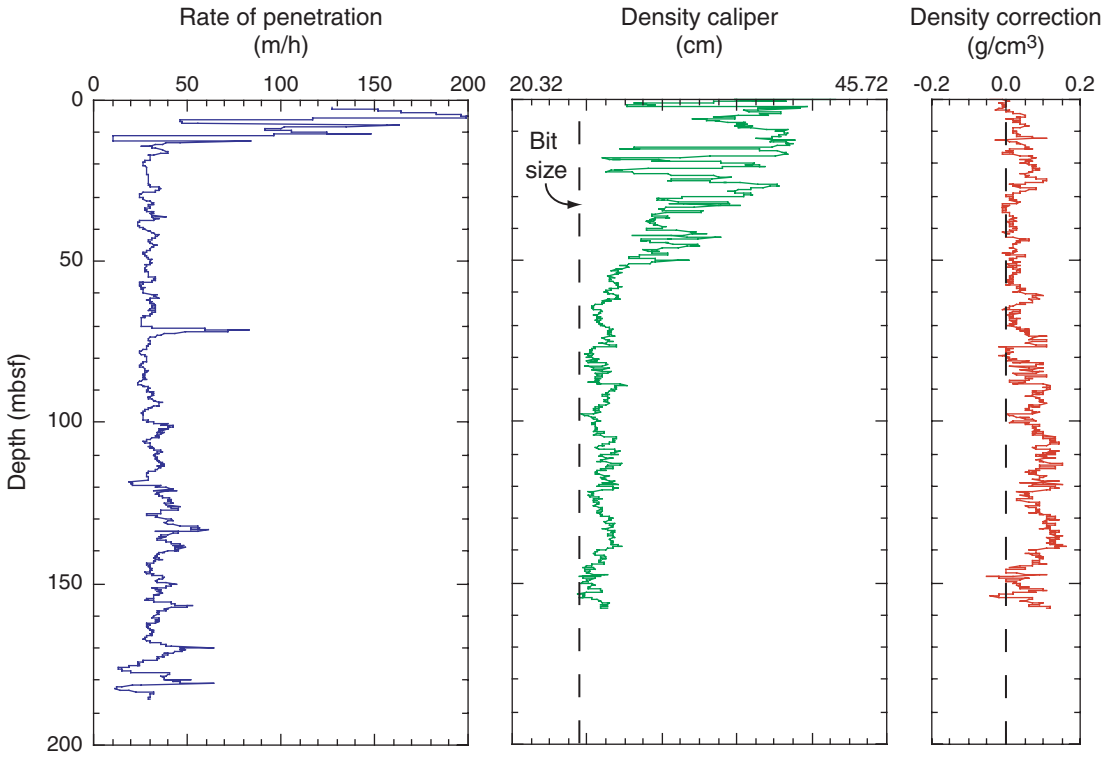

Figure F40. Caliper log, gamma radiation (GR), equivalent circulating density referenced to the seafloor (ECD_{rsf}), and annular overpressure while drilling (APWD*) in Hole U1319B. Linear increase of annular pressure while drilling (APWD), near-constant APWD*, and decreasing ECD_{rsf} are interpreted as features of a stable borehole without flow problems. SF = seafloor.

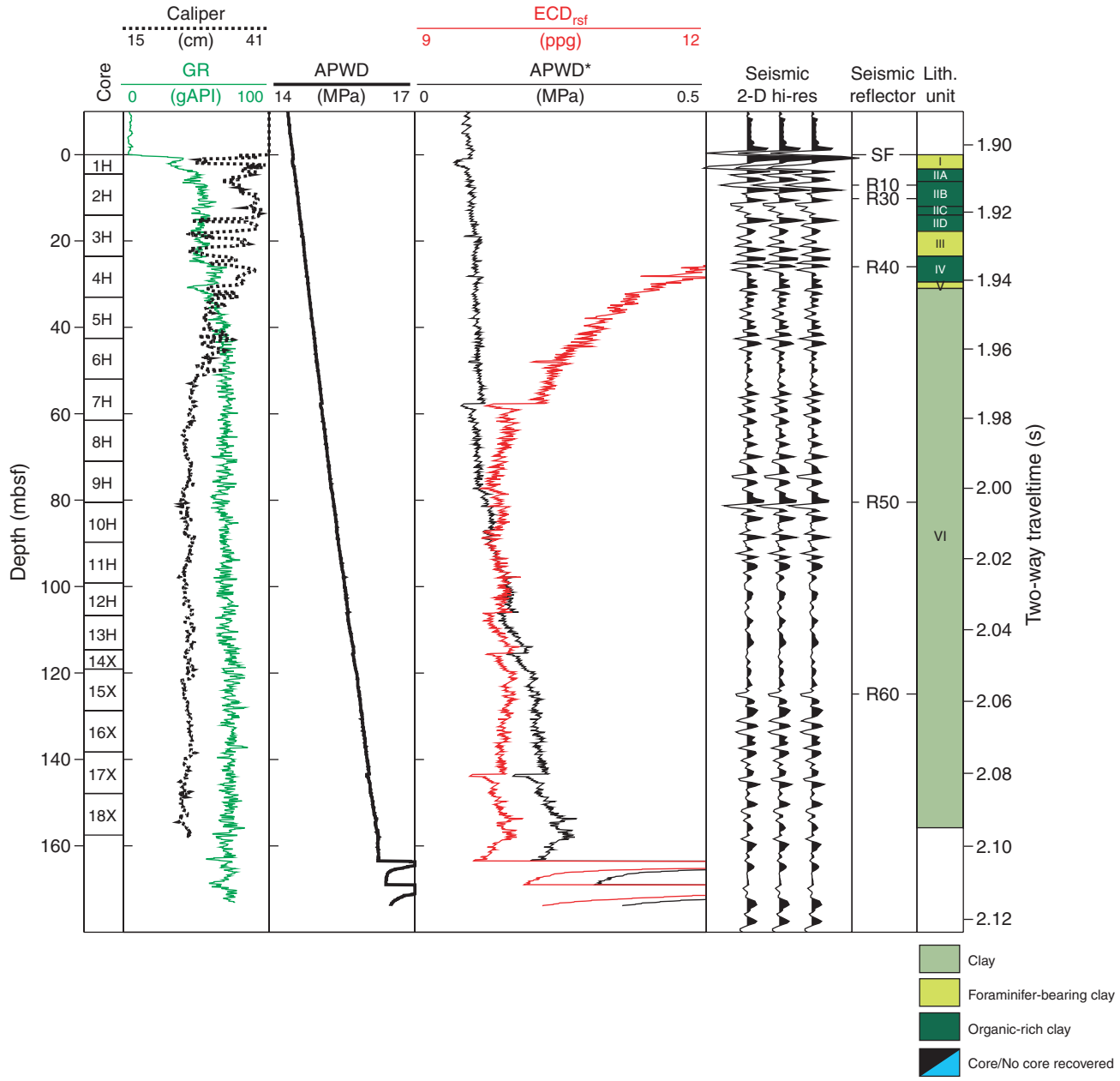

Figure F41. LWD logs recorded in Hole U1319B. Density caliper, photoelectric factor (PEF), and neutron porosity were recorded with the VDN tool, whereas gamma ray and resistivity measurements were obtained with the GVR tool. Superimposed on the PEF log is a five-point sliding window curve.

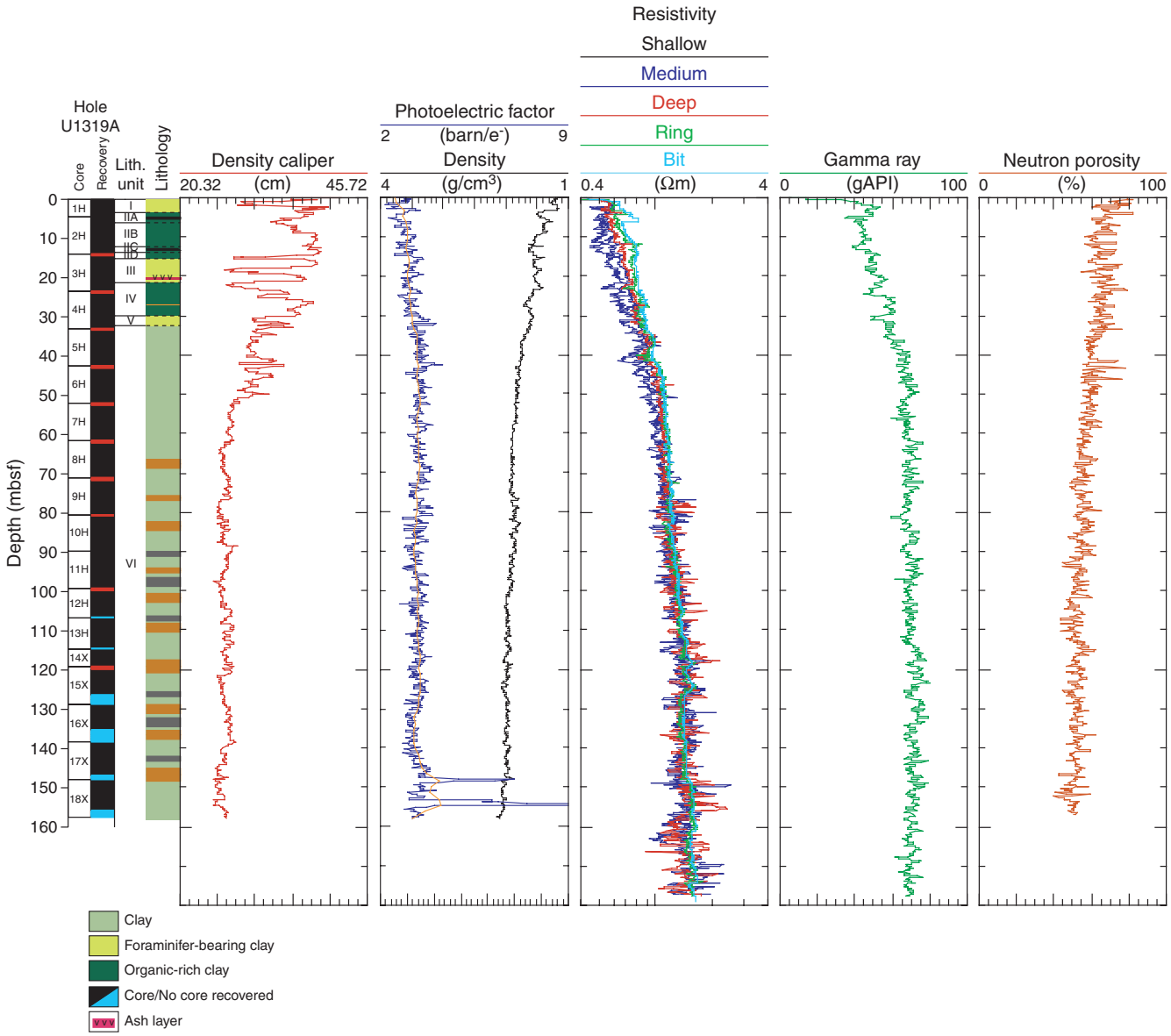

Figure F42. Resistivity-at-the-bit (RAB) GeoVision deep resistivity (GVR) static (left) and dynamic (right) image of the bottom of Hole U1319B showing steep features that may represent mass transport deposits and an erosional surface. Gamma radiation and resistivity curves are overlain.

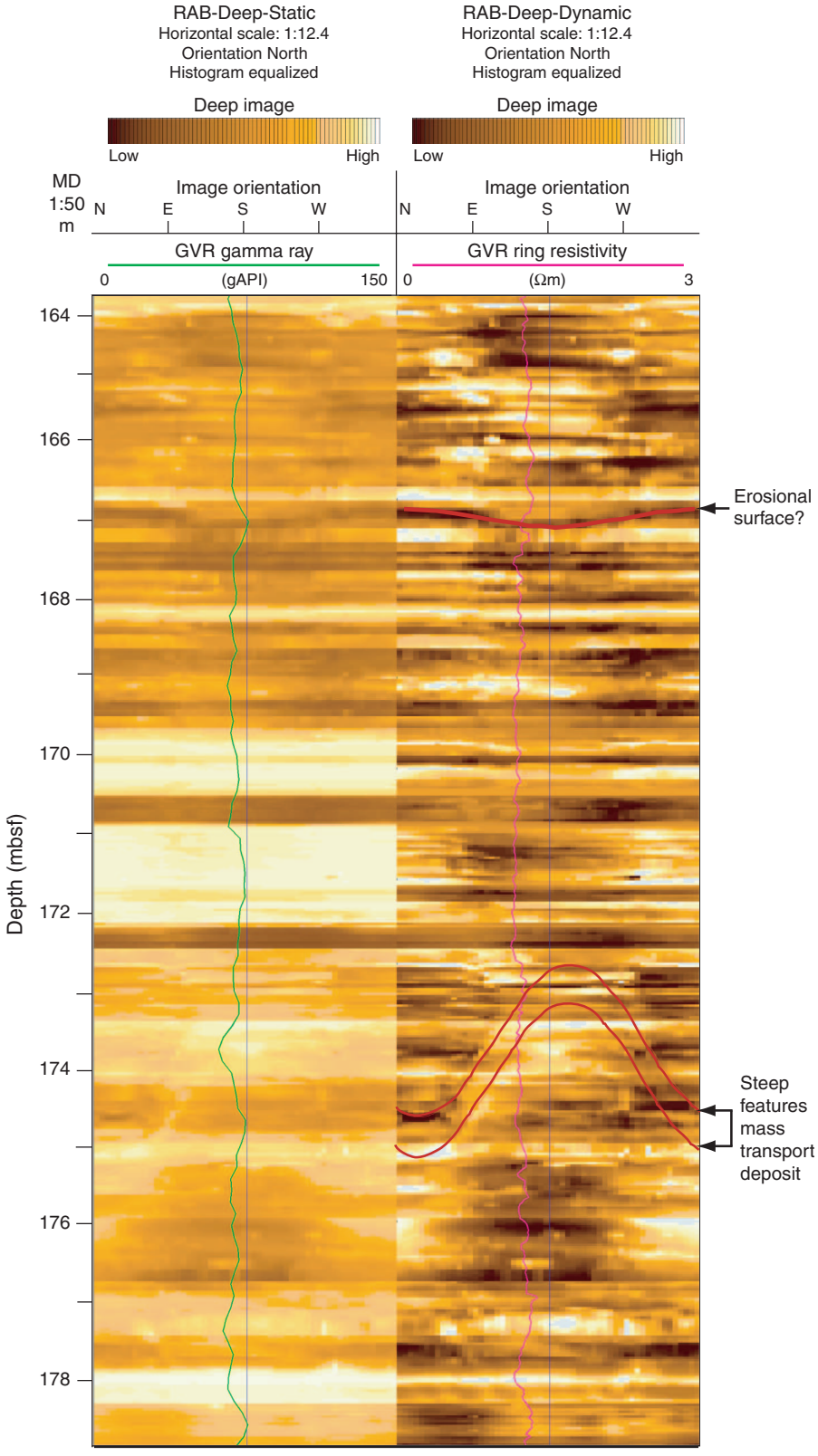

Figure F43. Log-core-seismic correlation for Site U1319. Synthetic seismogram was constructed by convolving a 200 Hz minimum-phase Ricker wavelet with the reflection coefficient series based on LWD bulk density and a constant velocity (1600 m/s). Seismic high-resolution (hi-res) trace is extracted from two-dimensional (2-D) high-resolution multichannel seismic data at the location of Site U1319. GR = gamma radiation. SF = seafloor.

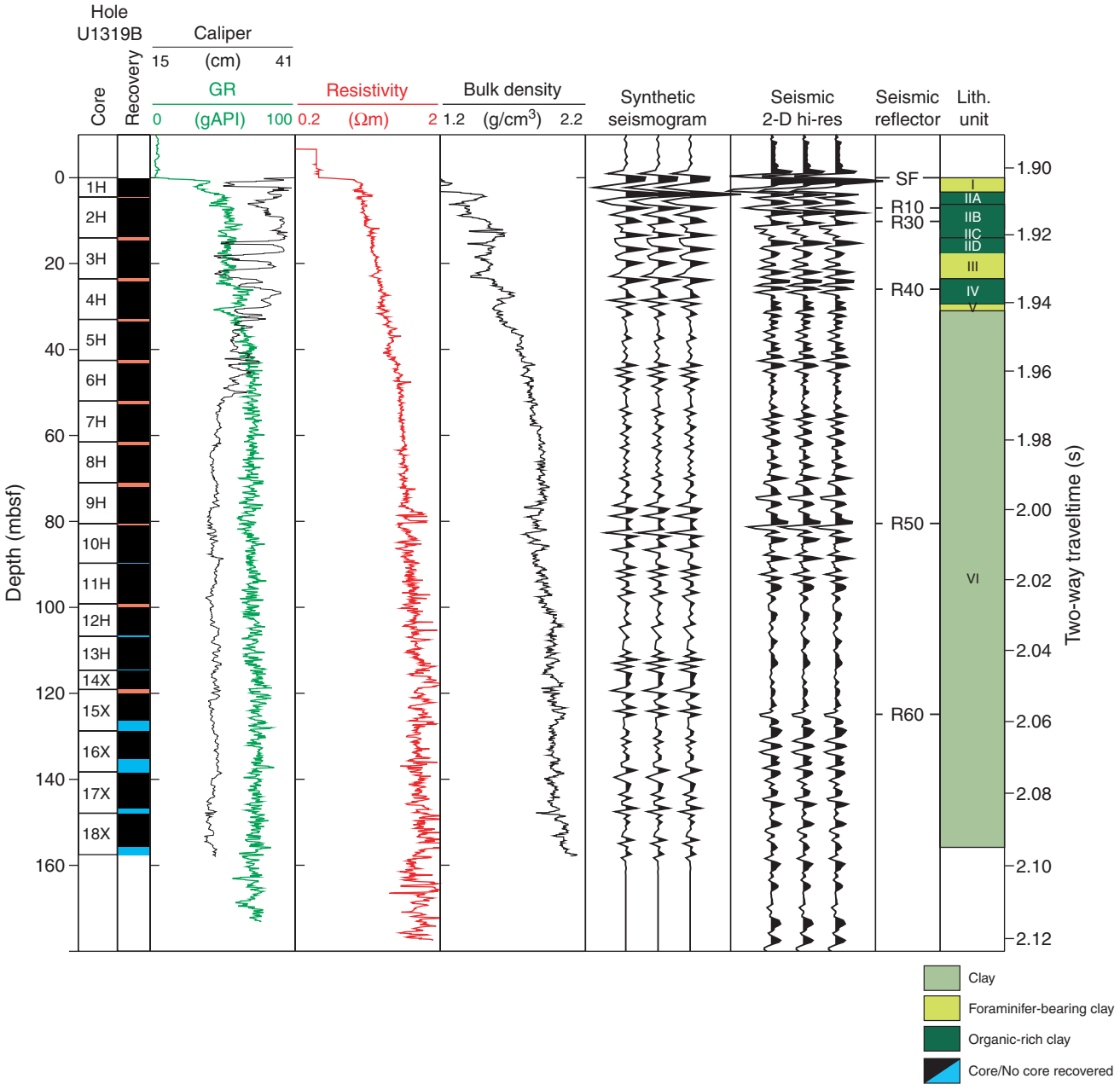

Figure F44. Time series data for advanced piston corer temperature (APCT) tool deployment at 42.5 mbsf (above Core 308-U1319A-5H). Equilibrium temperature is interpreted to be 5.86°C. Temperature spikes caused by friction are measured during insertion into the sediment and removal from the sediment. Data are available in "Downhole" in **"Supplementary material."**

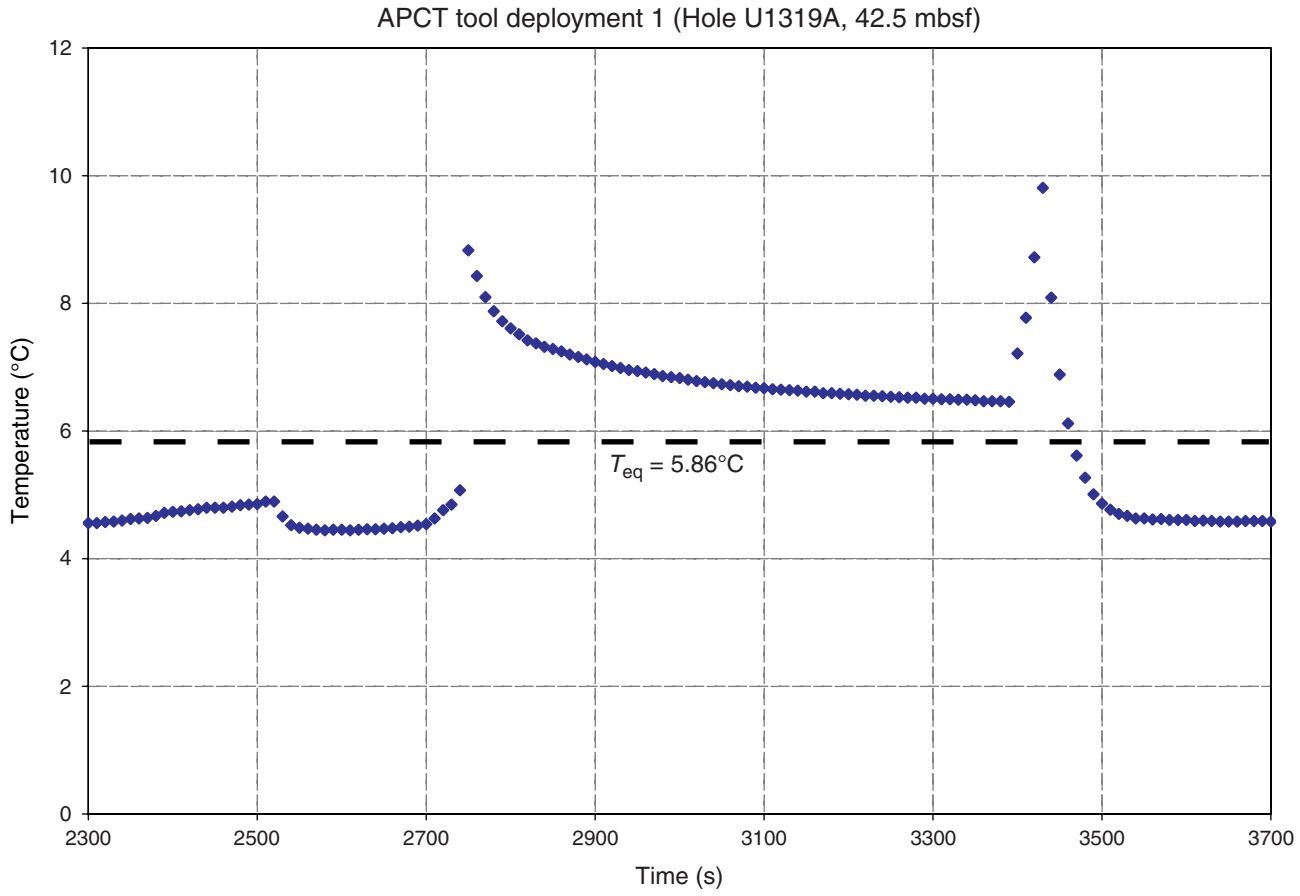

Figure F45. Pressure and temperature measured during Deployment 1 of the temperature/dual pressure (T2P) probe. A time series of deployment events (circled numbers) is provided in Table **T15.** Calculated hydrostatic pressure (green line) is plotted for comparison to the reference pressure measurements. Water density is assumed to be 1.024 g/cm^3 for the hydrostatic calculation. CDT = Central Daylight Time. Raw data are provided in "Downhole" in **"Supplementary material."**

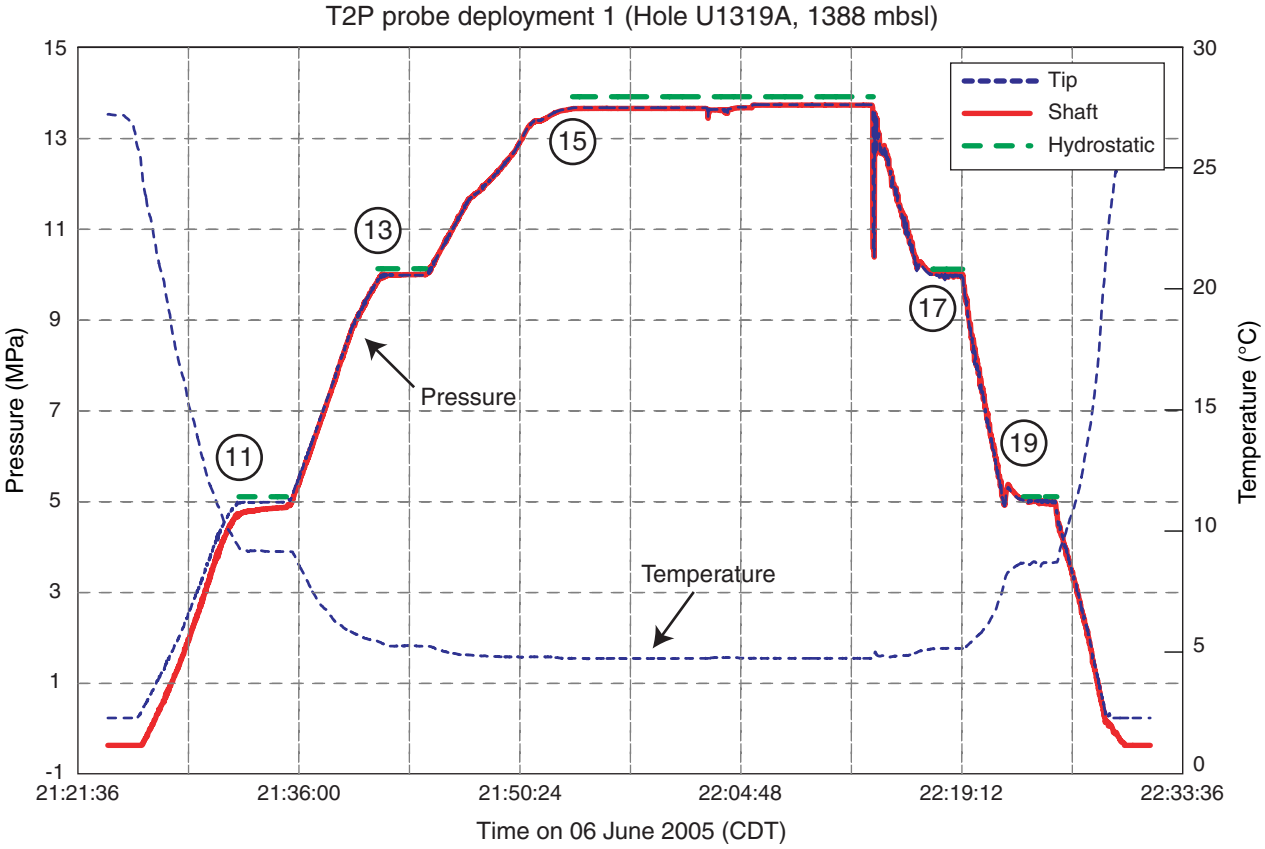

Figure F46. Fluid pressure and temperature measured during temperature/dual pressure (T2P) probe Deployment 2. The probe measurements were made in the top of the sediments recovered in Core 308-U1319A-10H. Table T16 provides the time-event log for this deployment (circled numbers). CDT = Central Daylight Time. Raw data are provided in "Downhole" in **"Supplementary material."**

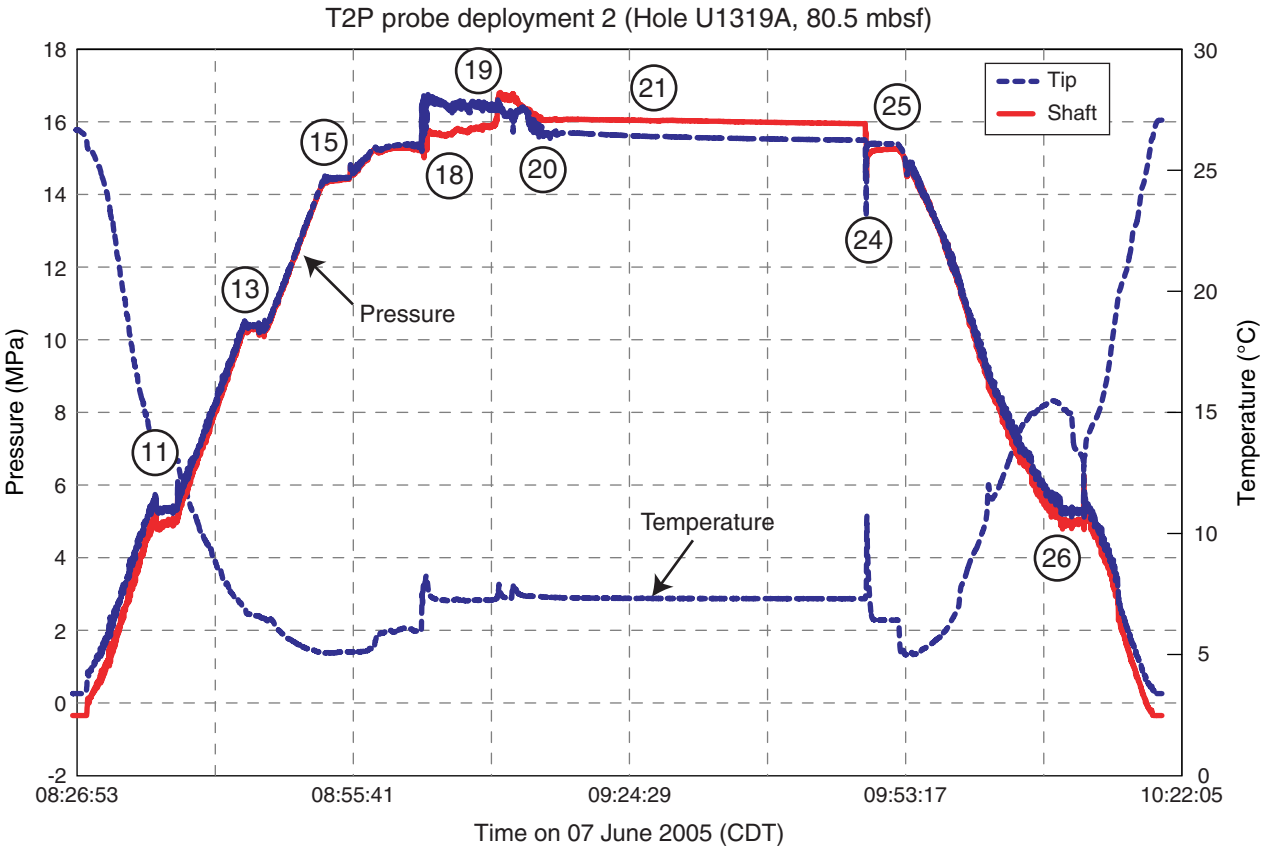

Figure F47. Damaged needle shaft from T2P Deployment 2.

Table T1. Two-way traveltime and depth of seismic surfaces, Holes U1319A, U1320A, and U1321A.

Reflector	Hole U1319A TWT (ms)	Hole U1319A Depth (mbsf)	Hole U1320A TWT (ms)	Hole U1320A Depth (mbsf)	Hole U1321A TWT (ms)	Hole U1321A Depth (mbsf)
SF	1903	0	1970	0	1946	0
R10	1912	7.03	2008	29.9	1973	21.2
R20	NA	NA	2070	79.6	2024	61.8
R30	1916	10.2	2141	138.2	2036	71.5
R40	1936	25.9	2189	178.8	2054	86.2
R50	2004	80.5	2254	229.6	2119	139.9
R60	2058	124.9	2310	284.3	2160	174.5

Notes: TWT = two-way traveltime. SF = seafloor reflector. NA = not applicable. See Equation **E1** for velocity model for time-depth conversion.

Table T2. Coring summary, Hole U1319A.

Hole U1319A
Latitude: 27°15.9751′N
Longitude: 94°24.1908′W
Time on site (h): 32.25
Seafloor (drill pipe measurement from rig floor, mbrf): 1440
Distance between rig floor and sea level (m): 10.4
Water depth (drill pipe measurement from sea level, m): 1429.6
Total depth (drill pipe measurement from rig floor, mbrf): 1597.5
Total penetration (meters below seafloor, mbsf): 157.5
Total length of cored section (m): 157.5
Total core recovered (m): 155.29
Core recovery (%): 98.6
Total number of cores: 18

Core	Date (Jun 2005)	Local time (h)	Depth (mbsf) Top	Depth (mbsf) Bottom	Length (m) Cored	Length (m) Recovered	Recovery (%)
308-U1319A-							
1H	7	0140	0.0	4.5	4.5	4.60	102.2
2H	7	0315	4.5	14.0	9.5	9.96	104.8
3H	7	0345	14.0	23.5	9.5	10.01	105.4
4H	7	0430	23.5	33.0	9.5	9.91	104.3
5H	7	0520	33.0	42.5	9.5	10.14	106.7
6H	7	0600	42.5	52.0	9.5	10.08	106.1
7H	7	0640	52.0	61.5	9.5	10.12	106.5
8H	7	0715	61.5	71.0	9.5	10.29	108.3
9H	7	0755	71.0	80.5	9.5	9.77	102.8
10H	7	1115	80.5	89.7	9.2	9.15	99.5
11H	7	1205	89.7	99.2	9.5	10.14	106.7
12H	7	1245	99.2	106.7	7.5	7.46	99.5
13H	7	1340	106.7	114.6	7.9	7.86	99.5
14X	7	1600	114.6	119.1	4.5	5.28	117.3
15X	7	1645	119.1	128.7	9.6	7.33	76.4
16X	7	1740	128.7	138.3	9.6	6.67	69.5
17X	7	1845	138.3	147.9	9.6	8.62	89.8
18X	7	2000	147.9	157.5	9.6	7.90	82.3
				Cored totals:	157.5	155.29	98.6

Table T3. Coring summary, Hole U1319B.

Hole U1319B
Latitude: 27°15.9857′N
Longitude: 94°24.1908′W
Time on site (h): 14.17
Seafloor (drill pipe measurement from rig floor, mbrf): 1441
Distance between rig floor and sea level (m): 10.4
Water depth (drill pipe measurement from sea level, m): 1430.6
Total depth (drill pipe measurement from rig floor, mbrf): 1621
Total penetration (meters below seafloor, mbsf): 180
Total length of cored section (m): 0
Total core recovered (m): 0
Core recovery (%): 0
Total number of cores: 0

Core	Date (Jun 2005)	Local time (h)	Depth (mbsf) Top	Depth (mbsf) Bottom	Length (m) Cored	Length (m) Recovered	Recovery (%)
308-U1319B-							
1-0	12	2100	0	180	0	0	0
				Cored totals:	0	0	0

Table T4. Lithostratigraphic units, Hole U1319C.

Unit	Top Core, section, interval (cm)	Top Depth (mbsf)	Bottom Core, section, interval (cm)	Bottom Depth (mbsf)	Thickness (m)	Lithology/Remarks
	308-U1319C-		308-U1319C-			
I	1H-1, 0	0.00	1H-3, 33	3.33	3.33	Clay, foraminifer bearing; base picked on first silty sand lamina
II	1H-3, 33	3.33	3H-3, 25	17.25	13.92	Clay with fine sand laminae
IIA	1H-3, 33	3.33	2H-2, 20	6.20	2.87	Clay with very fine sand and silt laminae
IIB	2H-2, 20	6.20	2H-5, 150	12.00	5.80	Clay, black organic
IIC	2H-6, 0	12.00	2H-8, 27	14.00*	2.00	Clay with very fine sand and silt laminae
IID	3H-1, 0	14.00	3H-3, 25	17.25	3.25	Clay
III	3H-3, 25	17.25	3H-8, 22	23.50*	6.25	Clay, foraminifer bearing; top: onset of foraminifer-bearing clay; bottom: sharp drop in lightness data
IV	4H-1, 0	23.50	4H-4, 150	29.50	6.00	Clay, with very fine sand laminae
V	4H-5, 0	29.50	4H-6, 150	31.00	1.50	Clay, foraminifer bearing
VI	4H-7, 0	31.00	18X-7, 29	155.80	124.80	Clay

Notes: Depth of unit boundary base was approximated to top of core immediately below. Measured length and calculated depth of core bottom exceeds top of next core due to greater than 100% recovery, as a result of gas expansion of core after recovery.

Table T5. Relative abundances of planktonic foraminifers, Hole U1319A.

Core, section, interval (cm)	Depth (mbsf)	Sample code	Zone	Age	Preservation	Group abundance	*Globigerina bulloides*	*Globigerina falconensis*	*Globigerinella calida*	*Globigerinella siphonifera*	*Globigerinoides conglobatus*	*Globigerinoides ruber* (pink)	*Globigerinoides ruber* (white)	*Globigerinoides sacculifer*	*Globorotalia crassaformis*	*Globorotalia flexuosa*	*Globorotalia inflata*	*Globorotalia menardii*	*Globorotalia scitula*	*Globorotalia truncatulinoides*	*Globorotalia tumida*	*Globoturborotalita hexagonus*	*Hastigerina pelagica*	*Neogloboquadrina dutertrei*	*Orbulina universa*	*Pulleniatina obliquiloculata*	Comments
308-U1319A-																											
1H-CC, 15–20	4.55	PAL	Z	Holocene	VG	C		R	R	F		F	R	R	F			F		R	R		R	F	F	R	
2H-CC, 22–27	14.41	PAL	Y		VG	R	R			F		F	F	R	F		F						R	R	R		
3H-CC, 17–22	23.96	PAL			VG	A		R	R	C	F	R	A	C	F	A		A	R	C	F	R	F	A	C	C	
4H-5, 9–13	29.59	QILI	X		M	A	R	R	R	C	C	R	A	A	A	F		A	R	C	C	R	R	C	F	A	
4H-5, 84–88	30.33	QILI			VG	A		R	R	C	C	A	A	A	F	R		A		F	A	R	F	C	C	C	
4H-CC, 23–28	33.36	PAL			G	R	R					F	F				R			R				R	R		Abundant pyrite
5H-CC, 36–41	43.09	PAL			VG	R	R			R		F	F			R	F			F					R		
6H-CC, 25–30	52.53	PAL			VG	R	R			R	R	F	F	R	F		F			R			R	R	R		
7H-CC, 22–27	62.07	PAL			VG	R	R			R		F	F		R		F				R				R		
8H-CC, 35–40	71.74	PAL			VG	R	R			R	R	F	F				F			R					F		
9H-CC, 32–37	80.72	PAL		Pleistocene	VG	R	R	R				F	F	R			R			R					R		
10H-CC, 33–38	89.6	PAL			VG	R	R			R		F	F				F			R					R		
11H-CC, 19–24	99.79	PAL	W		VG	R				R		F	F				F			R					R		
12H-CC, 38–43	106.61	PAL			VG	R				R		R	F	R			R			R					R		
13H-CC, 6–12	114.5	PAL			VG	R				R		F	F	R			F			F					R		
14X-CC, 22–27	119.83	PAL			VG	R	R			R		R	R	R			F			R					R		Coal grains?
15X-CC, 24–34	126.33	PAL			VG	R	F					R	F	R			F			R					R		
16X-CC, 13–19	135.31	PAL			VG	R	F			R		R	C				F			R					R		Coal grains?
17X-CC, 72–77	146.87	PAL			VG	R	R	R		R		R	F	R			R								R		Neritic
18X-CC, 24–29	155.75	PAL			VG	R	R			R		R	R				R								R		Neritic

Notes: Abundance: A = abundant, C = common, F = frequent, R = rare, VR = very rare, T = trace, B = barren. Preservation: VG = very good, G = good, M = moderate. PAL = paleontological sample, QILI = sample selected at core description table.

Table T6. Relative abundances of benthic foraminifers, Hole U1319A.

Core, section, interval (cm)	Depth (mbsf)	Preparation	Preservation	Group abundance	Bathymetry	*Ammodiscus tenuis*	*Bolivina spissa*	*Bolivina* spp.	*Bulimina aculeata*	*Bulimina* spp.	*Buliminella elegantissima*	*Buliminella tenuata*	*Cassidulina* spp.	*Chilostomella ovoidea*	*Cibicides* spp.	*Cibicidoides mckannai*	*Cibicidoides* spp.	*Cibicidoides wuellerstorfi*	*Dentalina* spp.	*Eggerella bradyi*	*Elphidium* spp.	*Epistominella* spp.	*Eponides* spp.	*Fursenkoina bradyi*	*Glandulina laevigata*	*Globobulimina affinis*	*Globocassidulina subglobosa*	*Gyroidina* spp.	*Hoeglundina elegans*	*Laticarinina pauperata*	*Lenticulina* spp.	*Melonis pompilioides*	*Melonis* spp.	*Nodosaria* spp.	*Oridorsalis tenera*	*Oridorsalis umbonatus*	*Pleurostomella* spp.	*Pyrgo* spp.	*Quinqueloculina* spp.	*Rhabdammina* sp.	*Sigmoilopsis* spp.	*Siphonina reticulata*	*Sphaeroidina bulloides*	*Trochammina* spp.	*Uvigerina hispida*	*Uvigerina* spp.	*Uvigerina subperegrina*	Comments
308-U1319A-																																															
1H-CC, 15–20	4.55	>150	VG	F	LB				F	F		R		R			R									R										R					F			F	R	
2H-CC, 22–27	14.41	>150	VG	F	LB				R	R									R																		R									
3H-CC, 17–22	23.96	>150	VG	R	LB												R								R				R										F		R		R			
4H-5, 9–13	29.59	>150	VG	R	LB				R	R							R								R				R				R								R		R		R	Some reworked
4H-5, 84–88	30.33	>150	VG	R	LB				R	R							R								R				R												R		R		R	
4H-CC, 23–28	33.36	>63	VG	R	UB			R	R	R							R																			R	R			R		F			Abundant pyrite
5H-CC, 36–41	43.09	>63	VG	F	LB		F		F	R				R			R	R									R				R							R				F	F			
6H-CC, 25–30	52.53	>63	VG	F	LB				R	R			R	F			R	R						R				R									R	R								
7H-CC, 22–27	62.07	>63	VG	F	LB		R	R	F					F										R				R				R					R		R			R			
8H-CC, 35–40	71.74	>63	VG	F	MB		R	R	F									R						R		R		R										R		R			R			
9H-CC, 32–37	80.72	>63	VG	F	MB			F	F				R				R							R							R					R	R					F		R	
10H-CC, 33–38	89.60	>63	VG	F	MB		R	F	R	R														C				R			R			R				F							
11H-CC, 19–24	99.79	>63	VG	R	MB			R	F	R																							R				F						R			
12H-CC, 38–43	106.61	>63	VG	R	MB			R	F	R			R	R			R																R			R	R							R		
13H-CC, 6–12	114.50	>63	VG	R	MB		R	R	R	R			R															F					R			R	R						R		R	
14X-CC, 22–27	119.83	>63	VG	R	MB		R	R	R				R											R									R				R									Coal grains?
15X-CC, 24–34	126.33	>63	VG	R	MB		R	C	R															R									R				R									
16X-CC, 13–19	135.31	>63	VG	F	MB			C	F	R			R				R							F				R								R	R					F			Coal grains
17X-CC, 72–77	146.87	>63	VG	R	UB		R	F	R	R			R	R			R							F				R							R		R					R		R	Shallow
18X-CC, 24–29	155.75	>63	VG	R	UB			R	R	R							R							R					R								R									Shallow

Notes: Abundance: A = abundant, C = common, F = frequent, R = rare, VR = very rare, T = trace, B = barren. Preservation: VG = very good, G = good, M = moderate. LB = lower bathyal, MB = mid-bathyal, UB = upper bathyal.

Table T7. Datums used to plot Figure F22, Hole U1319A.

Code	Event	Top		Bottom		Age (ka)	Average depth (mbsf)	Average sedimentation rate (m/k.y.)
		Core, section, interval (cm)	Depth (mbsf)	Core, section, interval (cm)	Depth (mbsf)			
		308-1319A-		308-1319A-				
MS	Tie point 1					20	5	
PF	LO *G. inflata*	1H-CC,15–20	4.5	2H-CC, 22–27	14.41	10	9.75	0.975
MS	Tie point 2					52	10	
MS	Tie point 3					65	14	
MS	Tie point 4					79	16	
PF	LO *G. flexuosa*	2H-CC, 22–27	14.41	3H-CC, 17–22	23.96	68	18.5	0.15
CN	FO *E. huxleyi* acme	2H-CC, 22–27	14.41	3H-CC, 17–22	23.96	90	18.5	
MS	Tie point 5					86	19	
MS	Tie point 6					97	22	
Lith	Ash layer					85	22.73	
MS	Tie point 7					106	25	
MS	Tie point 8					122	30	
	No occurrence of *H. inversa*	3H-CC, 17–22	14.41	18X-CC, 24–29	155.75	<150	157.5	>2.31

Notes: MS = magnetostratigraphy, PF = planktonic foraminifer, CN = calcareous nannofossil, lith = lithostratigraphy. FO = first occurrence; LO = last occurrence. High sedimentation rates from the lower part of the hole need confirmation by postcruise studies.

Table T8. Summary of pass-through cryogenic magnetometer measurements, Hole U1319A.

Measurement	Core, section
	308-U1319A-
Natural remanent magnetization (0, 15, 20, 30 mT)	1H-1 through 18H-CC
Skipped sections	12H-CC and 13H-CC
Tensor tool	3H through 13H

Table T9. Magnetostratigraphic tie points, Site U1319.

Magnetostratigraphic tie point	MIS	Age (ka)
MTP1	3.1	30
MTP2	3.3	52
MTP3	4.2	65
MTP4	5.1	79
MTP5	5.2	86
MTP6	5.3	97
MTP7	5.4	106
MTP8	5.5	122

Note: MIS = marine isotope stage. Corresponding MIS and ages assigned according to Bassinot et al., 1994.

Table T10. Pore water chemistry, Hole U1319A.

Core, section, interval (cm)	Depth (mbsf)	Alkalinity (mM)	pH	Salinity (pph)	Chlorinity (mM)	SO_4^{2-} (mM)	NH_4^+ (μM)	PO_4^{3-} (μM)	H_4SiO_4 (nM)	Na^+ (mM)	K^+ (mM)	Mg^{2+} (mM)	Ca^{2+} (mM)	B^{3+} (nM)	Li^+ (μM)	Sr^{2+} (μM)	Ba^{2+} (μM)	Fe^{2+} (μM)	Mn^{2+} (μM)
308-U1319A-																			
1H-1, 127–132	1.27			3.6	558	26.1		24.9	271	443	12.9	51.0	9.1	468	28.4	79.2	0.0	6.0	146.5
1H-2, 145–150	2.95			3.6	537	22.6		23.6	343	438	12.1	51.0	9.4	498	27.0	83.0	0.0	15.2	126.2
1H-3, 127–132	4.27	7.84	7.27	3.7	553	21.2	602	1.7	401	447	11.7	51.2	8.6	490	25.9	79.4	0.0	13.2	98.4
2H-1, 145–150	5.95	10.69	7.18	3.6	562	13.8	968	17.0	399	387	10.3	43.1	6.6	521	24.6	75.2	0.0	104.6	47.0
2H-2, 137–142	7.37			3.4	554	13.6		13.9	321	472	12.0	52.3	7.5	512	24.1	77.2	1.6	11.4	25.2
2H-3, 145–150	8.95	13.50	7.45	3.5	562	8.5	826	11.3	356	385	9.2	42.8	5.8	528	21.4	73.7	1.3	17.4	14.4
2H-5, 145–150	11.87	17.19	7.22	3.5	561	2.9	1161	43.9	407	366	8.7	38.7	4.5	558	20.2	75.6	8.2	64.7	5.2
2H-6, 145–150	13.45	19.45	7.35	3.4	557	0.5	1226	75.2	433	350	7.8	38.1	4.0	581	20.4	77.3	29.0	13.6	7.8
2H-7, 64–69	14.14	17.89	7.39	3.4	561	0.4	1699	54.1	388	384	8.5	41.0	4.1	554	20.8	78.9	32.6	26.3	7.1
3H-1, 145–150	15.45	16.60	7.43	3.5	564	0.8	1966	29.8	366	415	9.4	44.8	4.2	550	22.1	78.4	50.7	18.4	11.3
3H-2, 145–150	16.95	15.72	7.46	3.4	559	1.1	2005	28.2	415	426	9.6	45.9	4.3	552	23.4	80.4	54.5	27.0	12.1
3H-3, 145–150	18.45	15.58	7.46	3.4	546	0.4	1870	26.6	419	419	9.8	45.0	4.2	585	24.1	86.0	59.2	15.3	15.1
3H-4, 145–150	19.95	14.60	7.48	3.4	563	0.6	1812	18.6	394	435	9.6	46.6	4.3	554	23.6	83.1	56.9	19.5	19.5
3H-5, 145–150	21.45	14.23	7.66	3.4	563	0.4	1373	27.3	394	416	9.7	44.2	4.1	585	23.1	83.4	60.7	17.0	21.3
3H-6, 145–150	22.95	13.53	7.45	3.4	564	0.4	1778	23.1	379	423	9.1	46.3	4.5	544	21.3	83.3	65.1	10.8	19.3
3H-7, 74–79	23.74	12.02	7.7	3.4	565	0.6	1974	7.5	300	427	9.9	44.2	3.9	499	20.0	79.2	62.5	7.2	14.3
4H-1, 145–150	24.95	12.94	7.69	3.4	562	0.6	1846	16.7	236	427	9.4	46.4	4.9	550	19.6	85.4	61.1	0.1	18.3
4H-3, 145–150	27.95	11.66	7.73	3.3	555	0.6	1349	34.3	369	423	9.0	45.1	5.4	606	19.2	87.3	52.1	1.1	23.9
4H-4, 145–150	29.37	9.33	7.84	3.4	553	0.6	2367	21.8	234	411	10.2	41.6	4.6	457	18.5	79.3	50.5	0.0	11.7
4H-5, 145–150	30.95	9.71	7.61	3.5	556	0.3	715	16.4	378	425	8.8	44.1	5.5	517	18.6	85.4	50.4	19.8	12.1
4H-6, 145–150	32.45	8.56	7.63	3.4	561	0.3	1988	13.2	476	425	8.3	45.8	6.2	491	17.4	87.8	44.2	16.1	9.3
4H-7, 58–63	33.08	7.21	7.74	3.4	568	0.4	291	10.7	318	425	9.8	42.8	5.8	465	19.9	87.8	46.0	2.0	6.2
5H-1, 145–150	34.45			3.4	563	1.8	1515	3.0	356	413	8.5	43.1	6.4	485	18.1	88.9	39.1	3.0	3.8
5H-2, 145–150	35.95	4.90	7.83	3.4	572	1.4	1349	9.4	258	433	9.7	42.7	6.5	384	18.3	86.2	36.2	1.3	2.6
5H-3, 145–150	37.37	5.00	7.5	3.4	565	1.6	1631	2.3	357	431	8.0	43.0	7.1	459	16.5	88.4	32.7	25.0	2.3
5H-4, 145–150	38.95	4.40	7.54	3.4	568	0.7	1349	4.6	264	418	9.1	41.0	6.7	384	17.7	88.0	33.9	10.2	1.5
5H-5, 145–150	40.45	4.01	7.51	3.3	570	0.7	1421	4.9	257	382	7.7	39.1	6.6	395	17.4	89.3	30.8	14.5	1.6
5H-6, 145–150	41.95	4.17	7.47	3.4	565	0.6	2451	2.7	281	408	7.8	42.0	7.7	406	16.3	88.7	27.9	34.3	1.8
5H-7, 145–150	42.68	3.85	7.61	3.3	555	0.5	1487	4.6	169	406	7.8	41.7	7.3	372	16.4	88.5	28.8	4.8	1.2
6H-1, 145–150	43.95	3.56	7.47	3.3	564	1.0	1947	2.3	169	397	7.2	40.2	7.5	428	14.7	89.4	26.2	32.5	2.0
6H-2, 145–150	45.45			3.2	567	0.7	2709	1.1	215	411	6.7	43.3	8.3	427	15.9	93.5	26.3	22.5	1.7
6H-3, 145–150	46.95	3.44	7.4	3.4	565	1.1	2550	2.0	212	394	7.4	39.7	8.4	423	18.6	90.8	27.0	21.2	3.0
6H-4, 145–150	48.45	3.42	7.46	3.4	561	0.6	2940	5.9	186	410	8.1	40.8	8.5	371	19.3	90.3	24.9	3.9	1.8
6H-5, 145–150	49.95	3.66	7.33	3.4	562	0.6	1867	1.4	308	406	7.0	42.2	9.0	429	17.5	95.7	22.4	47.7	2.6
6H-7, 53–58	52.03	3.69	7.4	3.4	563	0.6	2839	2.7	246	403	7.1	41.6	9.0	404	17.1	94.6	21.6	2.7	2.6
7H-1, 145–150	53.45	3.30	7.39	3.4	565	0.9	3112	13.5	214	363	6.3	38.0	8.3	371	18.2	95.1	19.7	3.1	2.3
7H-2, 145–150	54.95	3.11	7.45	3.3	568	1.0	3201	2.3	147	404	7.3	41.1	9.3	337	17.6	93.4	19.1	2.0	2.6
7H-3, 137–142	56.37	2.95	7.35	3.4	566	0.8	2837	5.9	144	410	7.7	41.0	8.9	285	18.8	88.5	20.2	0.0	2.0
8H-3, 137–142	65.87	3.23	7.41	3.4	564	0.8	3413	2.7	140	423	6.5	43.3	10.1	354	13.0	94.0	15.6	0.3	3.2
9H-4, 137–142	76.87	3.40	7.43	3.4	564	0.7	3717	5.9	218	411	5.8	42.0	10.4	334	19.3	98.5	16.9	4.3	2.6
10H-5, 137–142	87.87			3.3	564	1.3	2764	2.1	365	413	4.8	43.2	11.2	396	17.6	103.3	19.6	60.7	3.8
11H-3, 145–150	93.07	3.09	7.53	3.4	567	1.4	2789	3.9	184	408	5.5	40.9	10.7	270	16.1	100.5	20.7	3.7	4.2
12H-2, 137–142	102.07	3.83	7.49	3.3	567	1.1	2979	2.3	221	379	3.9	39.1	10.2	385	11.3	104.4	19.8	0.0	2.4
13H-3, 77–82	109.72	3.36	7.64	3.2	516	1.4	3097	2.0	194	367	3.9	36.9	9.4	380	12.4	112.2	25.8	9.3	3.0
14X-2, 136–141	117.46	3.09	7.51	3.4	570	1.7	4180	5.2	143	402	4.6	39.9	10.3	287	12.6	105.7	24.0	0.0	2.1
15X-1, 145–150	123.60	3.73	7.33	3.5	548	2.9	3784	1.7	290	378	3.6	39.7	10.2	415	13.8	110.0	23.2	17.1	4.4
16X-3, 137–142	133.07	3.68	7.51	3.5	564	2.1	4235	5.9	197	345	3.9	33.2	7.8	366	15.1	102.6	23.8	0.0	2.7
17X-3, 145–150	142.75	3.96	7.55	3.4	552	2.5	4411	4.6	159	433	4.3	43.3	10.6	294	13.7	100.4	23.2	0.0	1.9

Table T11. Sediment elemental analysis, Hole U1319A.

Core, section, interval (cm)	Depth (mbsf)	Carbon (wt%)				TN (wt%)	TH (wt%)	C/N (mol:mol)
		Total	Inorganic	$CaCO_3$	Organic			
308-U1319A-								
1H-1, 127–132	1.27	3.10	2.47	20.55	0.63	0.28	0.96	2.64
1H-2, 145–150	2.95	1.80	1.57	13.10	0.23	0.24	0.81	1.09
1H-3, 127–132	4.27	1.50	0.82	6.87	0.68	0.21	0.73	3.70
2H-1, 145–150	5.95	1.54	0.73	6.07	0.81	0.23	0.79	4.06
2H-2, 137–142	7.37	1.95	1.07	8.92	0.88	0.27	0.95	3.83
2H-3, 145–150	8.95	1.92	1.05	8.74	0.87	0.27	1.01	3.83
2H-4, 145–150	10.45	1.84	1.05	8.73	0.79	0.23	0.90	3.98
2H-5, 137–142	11.87	1.59	0.98	8.14	0.61	0.17	0.49	4.08
2H-6, 145–150	13.45	1.70	0.64	5.37	1.06	0.21	0.82	5.92
3H-1, 145–150	15.45	2.35	1.83	15.27	0.52	0.24	0.96	2.52
3H-2, 145–150	16.95	2.40	1.86	15.48	0.54	0.26	0.85	2.39
3H-3, 145–150	18.45	2.87	2.17	18.04	0.70	0.27	0.88	2.97
3H-4, 145–150	19.95	1.83	1.37	11.41	0.46	0.24	0.89	2.24
3H-5, 145–150	21.45	2.79	2.18	18.17	0.61	0.28	0.92	2.54
3H-6, 145–150	22.95	2.30	1.96	16.30	0.34	0.22	0.89	1.79
3H-7, 74–79	23.74	4.08	3.56	29.64	0.52	0.28	0.82	2.21
4H-1, 145–150	24.95	0.87	0.16	1.35	0.71	0.27	1.06	3.10
4H-2, 145–150	26.45	0.92	0.16	1.32	0.76	0.24	0.97	3.67
4H-3, 145–150	27.95	1.34	0.57	4.77	0.77	0.27	1.04	3.32
4H-4, 137–142	29.37	2.67	2.18	18.19	0.49	0.26	0.97	2.20
4H-5, 145–150	30.95	2.04	1.47	12.23	0.57	0.28	0.96	2.37
4H-6, 145–150	32.45	2.50	2.34	19.51	0.16	0.21	0.79	0.88
4H-7, 58–63	33.08	3.13	2.31	19.21	0.82	0.28	0.94	3.38
5H-1, 145–150	34.45	2.99	1.09	9.09	1.90	0.26	0.95	8.53
5H-2, 145–150	35.95	1.65	1.87	15.61	ND	0.21	0.73	
5H-3, 137–142	37.37	2.82	1.55	12.93	1.27	0.26	0.83	5.74
5H-4, 145–150	38.95	2.85	1.82	15.19	1.03	0.25	0.73	4.88
5H-5, 145–150	40.45	3.43	2.55	21.27	0.88	0.22	0.68	4.72
5H-6, 145–150	41.95	3.55	2.67	22.24	0.88	0.25	0.59	4.06
5H-7, 68–73	42.68	2.36	1.43	11.91	0.93	0.25	0.80	4.42
6H-1, 145–150	43.95	2.08	1.24	10.35	0.84	0.22	0.81	4.48
6H-2, 145–150	45.45	2.74	1.86	15.48	0.88	0.23	0.77	4.50
6H-3, 145–150	46.95	3.15	2.19	18.25	0.96	0.23	0.69	4.92
6H-4, 145–150	48.45	3.44	2.40	19.97	1.04	0.24	0.68	4.99
6H-5, 145–150	49.95	3.44	2.50	20.82	0.94	0.20	0.68	5.48
6H-7, 53–58	52.03	3.66	2.73	22.76	0.93	0.22	0.65	4.86
7H-1, 145–150	53.45	3.88	2.80	23.35	1.08	0.26	0.70	4.78
7H-2, 145–150	54.95	3.51	2.64	21.97	0.87	0.25	0.63	4.08
7H-3, 137–142	56.37	3.31	2.50	20.86	0.81	0.23	0.67	4.21
8H-3, 137–142	65.87	3.78	3.09	25.74	0.69	0.19	0.56	4.21
9H-4, 137–142	76.87	4.06	3.26	27.14	0.80	0.19	0.58	4.99
10H-5, 137–142	87.87	2.80	2.03	16.93	0.77	0.21	0.75	4.24
11H-3, 145–150	93.07	3.06	2.51	20.90	0.55	0.20	0.59	3.19
12H-2, 137–142	102.07	3.56	3.01	25.10	0.55	0.20	0.53	3.27
13H-3, 77–82	109.72	3.77	3.24	26.97	0.53	0.17	0.55	3.55
14X-2, 136–141	117.46	3.10	2.46	20.52	0.64	0.20	0.61	3.69
15X-3, 145–150	123.55	2.98	2.43	20.21	0.55	0.19	0.58	3.30
16X-3, 137–142	133.07	3.30	2.74	22.86	0.56	0.21	0.59	3.07
17X-3, 145–150	142.75	3.14	2.54	21.17	0.60	0.18	0.57	3.85
18X-3, 137–142	152.27	3.22	2.55	21.20	0.67	0.20	0.56	3.99

Note: ND = not determined.

Table T12. Headspace gas analysis, Hole U1319A.

Core, section, interval (cm)	Depth (mbsf)	Headspace gas (ppmv)		C_1/C_2 ratio
		Methane	Ethane	
308-U1319A-				
1H-3, 0–5	3.0	2.4	0.0	
2H-5, 0–5	10.5	2.4	0.0	
3H-5, 0–5	20.0	6,333	0.0	
4H-5, 0–5	29.5	11,310	0.0	
5H-5, 0–5	39.0	7,195	0.0	
6H-5, 0–5	48.5	4,560	0.0	
7H-5, 0–5	58.0	4,325	0.0	
8H-5, 0–5	67.5	1,893	0.0	
9H-5, 0–5	77.0	2,116	0.0	
10H-5, 0–5	86.5	894.1	0.0	
12H-5, 0–5	105.2	7,950	0.7	11,357
13H-5, 0–5	111.4	7,879	0.0	
14X-3, 0–5	117.6	5,785	0.0	
15X-5, 0–5	125.1	5,072	0.0	
16X-5, 0–5	134.2	6,907	0.7	9,867
17X-5, 0–5	144.3	7,710	0.6	12,850
18X-5, 0–5	153.9	1,870	0.0	

Table T13. Microbiology, Hole U1319A.

Core, section, interval (cm)	Cell density (cells/mL)
308-U1319A-	
1H-3, 4.3–4.4	1.2×10^6
2H-2, 7.4–7.5	1.1×10^6
2H-5, 11.9–12.0	5.9×10^5
3H-2, 16.9–17.0	4.0×10^4
3H-5, 21.4–21.5	2.0×10^4
4H-3, 29.4–29.5	1.0×10^4
5H-3, 37.4–37.5	1.2×10^5
6H-3, 46.9–47.0	3.5×10^4
7H-3, 56.4–56.5	1.0×10^4
8H-3, 65.9–66.0	2.0×10^4
9H-3, 76.9–77.0	ND
10H-3, 84.9–85.0	2.0×10^4
12H-3, 102.1–102.2	1.0×10^4
13H-3, 109.8–109.9	ND
14X-3, 117.5–117.6	ND
16X-3, 133.1–133.2	1.0×10^4
18X-3, 152.3–152.4	ND

Note: ND = not detected or below significant levels (1.0×10^4 cells/mL).

Table T14. Downhole tool deployment, Site U1319.

Hole	Tool	Deployment	Depth (mbsf)	Depth (mbsl)	Date (2005)	Time in formation (min)
308-						
U1319A	T2P	1	–41.6	1388.0	6 June	5
U1319A	APCT	1	42.5	1471.7	7 June	10
U1319A	T2P	2	80.5	1509.7	7 June	35

Note: T2P = temperature/dual pressure probe, APCT = advanced piston corer temperature tool.

Table T15. T2P Deployment 1, Hole U1319A.

Event	Time (CDT)	Description
1	18:31:00	Data logger started at 1 Hz
2	20:46:00	T2P on rig floor
3	21:10:00	T2P raised vertically
4	21:10:20	Pressure response chamber removed from T2P tip
5	21:10:20	Shroud in place over T2P tip
6	21:11:19	T2P placed in drill pipe
7	21:13:00	T2P connected to spacer
8	21:16:16	CDS connected to spacer
9	21:16:43	CDS in extended position
10	21:20:05	Start lowering T2P downhole
11	21:32:35	Stop at 511 mbsl
12	21:35:00	Start lowering probe
13	21:41:27	Stop at 1011 mbsl
14	21:44:00	Start lowering probe
15	21:55:33	Stop at 1388 mbsl
16	22:01:30	Start pulling T2P uphole
17	22:16:59	Stop at 1010 mbsl
18	22:19:02	Continue pulling T2P uphole
19	22:23:05	Stop at 511 mbsl
20	22:25:09	Continue pulling T2P uphole
21	22:41:40	T2P on rig floor
22	22:41:52	T2P tip in pressure response chamber
23	22:46:46	Pressure response test
24	22:58:00	Data downloaded from data logger
25	23:40:00	Battery removed from T2P

Notes: Date = 6 June 2005. Depth = 1388 mbsl. T2P = temperature/dual pressure probe. CDS = colleted delivery system. CDT = central daylight time.

Table T16. T2P Deployment 2, Hole U1319A.

Event	Time (CDT)	Description
1	01:07:50	Data logger started at 1 Hz
2	08:13:28	T2P on rig floor
3	08:15:48	T2P raised vertically
4	08:16:10	Pressure response chamber removed from T2P tip
5	08:16:10	Shroud in place over T2P tip
6	08:19:38	T2P placed in drill pipe
7	08:20:11	T2P connected to spacer
8	08:23:54	CDS connected to spacer
9	08:25:15	CDS in extended position
10	08:26:52	Start lowering T2P downhole, pumps on
11	08:35:03	Stop at 511 mbsl, pumps off
12	08:37:20	Start lowering probe, pumps on
13	08:44:25	Stop at 1012 mbsl, pumps off
14	08:46:30	Start lowering probe, pumps on
15	08:52:39	Stop at 1431 mbsl, pumps off
16	08:55:05	Start lowering probe
17	08:58:20	T2P passes through lockable float valve
18	09:05:45	CDS lands in BHA
19	09:08:52	Start penetration of T2P into sediment
20	09:15:29	End of T2P penetration
21	09:27:03	Pumps on at 10 spm
22	09:47:30	Start pulling T2P uphole
23	09:48:50	Stop pulling at 1509 mbsl
24	09:49:30	Pulling/releasing winch to free CDS from BHA
25	09:52:20	Start pulling T2P uphole
26	10:09:04	Stop at 511 mbsl, pumps off
27	10:11:30	Start pulling T2P uphole
28	10:20:59	CDS detached from wireline
29	10:27:50	CDS detached from spacer
30	10:30:16	Spacer detached from T2P
31	10:30:50	T2P on rig floor
32	10:31:16	T2P tip in pressure response chamber
33	10:39:00	T2P in workroom
34	10:49:00	Battery removed from T2P
35	11:04:38	T2P connected to direct-current power
36	11:05:00	Data downloaded from data logger

Notes: Date = 7 June 2005. Depth = 81.37 mbsf. T2P = temperature/dual pressure probe. CDS = colleted delivery system. BHA = bottom-hole assembly. spm = strokes per minute. CDT = central daylight time.